An Evaluation of Tree Ring Records as Proxies for Historical Atmospheric River Storm Variability in Southwest BC

by

Laura Mackey

B.Sc. (Environmental Science), McGill University, 2020

Thesis Submitted in Partial Fulfillment of the
Requirements for the Degree of
Master of Resource Management

in the
School of Resource and Environmental Management
Faculty of Environment

SIMON FRASER UNIVERSITY
Summer 2024

Declaration of Committee

Name:	**Laura Mackey**
Degree:	**Master of Resource Management**
Title:	**An Evaluation of Tree Ring Records as Proxies for Historical Atmospheric River Storm Variability in Southwest BC**
Committee:	**Chair:** **John Axsen** Professor, Resource and Environmental Management
	Karen Kohfeld Supervisor Professor, Environmental Science
	Diana Allen Committee Member Professor, Earth Sciences
	William Jesse Hahm Examiner Assistant Professor, Geography

Abstract

Atmospheric rivers (ARs) influence floods, droughts, and snowpack levels in southwest British Columbia (BC), making their variability consequential to the region's water resources. While instrumental AR data are limited to recent decades, tree ring records can extend knowledge of AR trends by centuries, allowing for better contextualization of current and future AR trends. This research evaluates two dendrochronological methods – tree ring width and tree ring $\delta^{18}O$ – for their novel use as proxy records of historical AR variability in southwest BC. Generalized Additive Models reveal that AR data explain tree ring width and $\delta^{18}O$ variability not explained by other climate data, suggesting an AR signal. The strength of this signal is stronger for tree ring $\delta^{18}O$, with the percentage of fall precipitation from Pineapple Express (PE)-type ARs explaining up to 44% of $\delta^{18}O$ variance. These results indicate the potential for centuries-long PE records and carry important implications for water resource management.

Keywords: Atmospheric river; Pineapple Express; dendrochronology; tree ring; $\delta^{18}O$; climate change

For my dad – thank you for showing me the forest.

Acknowledgements

This research would not have been possible without the mentorship of my supervisor, Dr. Karen Kohfeld, and my committee member, Dr. Diana Allen. Your insights, guidance, and thoughtful feedback helped challenge and shape my scientific thinking. Thank you both for supporting my curiosities.

A big thank you to my tree coring team: Talia Cole, Lea Antesz, Ariel Greenblat, and especially Abby McCarthy and Cass Pereira, whom I brought to the forest an uncountable number of times. I am very grateful for your company and arm strength!

A number of people were indispensable to this thesis. Thank you to my valiant lab assistants Ciaran Dudley, Dayna Lee, Tiffany Lam, and Autumn Dao, who sliced and ground very many tree rings, and Jeremy Klein, who helped measure those tree rings. Thanks also to the many people who offered their knowledge and expertise throughout the research process: Christie Spry, whose work inspired and informed mine; Celeste Barlow, who shared many dendrochronological insights; Ionut Aron, who knew where to find Pacific silver firs; James Shoults, who turned 2x4s into dozens of tree core mounts; Dr. Sandra Timsic, who supported my early α-cellulose $\delta^{18}O$ inquiry; Dr. Christine Shields, who answered my many NetCDF and atmospheric river cataloguing questions; and Ian Bercovitz, who supported my statistical analyses.

Additional thanks to the students I instructed as a teaching assistant for Introduction to Environmental Science while completing my thesis. It was a joy to share the world of environmental science with you!

With lots of gratitude for my friends, family, and partner for cheering me on.

Finally, thank you to the Douglas-firs and Pacific silver firs who shared their secrets with me.

This work was supported by funds from the J. Stone Memorial Graduate Bursary of Environment, the SFU School of Environmental Science, a Canadian Natural Sciences and Engineering Research Council Discovery Grant awarded to Karen Kohfeld, and a Pacific Institute for Climate Solutions grant awarded to Diana Allen and Jesse Hahm.

Table of Contents

List of Tables

List of Figures

List of Acronyms

AIC	Akaike Information Criterion
AMJ	April, May, June (spring)
AO	Arctic Oscillation
AR	Atmospheric river
BC	British Columbia
CWHdm	Coastal Western Hemlock dry maritime
CWHvm1	Coastal Western Hemlock very wet maritime
ENSO	El Niño Southern Oscillation
EPS	Expressed Population Signal
GAM	Generalized Additive Model
GS-RH	Growing season relative humidity
ITRDB	International Tree Ring Database
IVT	Integrated horizontal vapour transport
IWV	Integrated water vapour
JAS	July, August, September (summer)
JFM	January, February, March (winter)
LAC	Library and Archives Canada
M	Mean
MCC	Mean cloud cover
MERRA-2	Modern-Era Retrospective Analysis for Research and Applications Version 2
MJO	Madden-Julian Oscillation
MKRF	Malcolm Knapp Research Forest
MKRF-1	Malcolm Knapp Research Forest site 1
MKRF-2	Malcolm Knapp Research Forest site 2
NCEP/NCAR	National Centers for Environmental Prediction/National Center for Atmospheric Research
NPGO	North Pacific Gyre Oscillation
OND	October, November, December (fall)
ONDJFM	October, November, December, January, February, March
PAR	Photosynthetically active radiation
PDO	Pacific Decadal Oscillation
PE	Pineapple Express

PE AR	Pineapple Express-type Atmospheric River
PNA	Pacific/North American pattern
PNW	Pacific Northwest
RH	Relative humidity
RWI	Radial width index
SD	Standard deviation
SFU	Simon Fraser University
SPEI	Standardised Precipitation-Evapotranspiration Index
SST	Sea surface temperature
SWE	Snow water equivalent
US	United States
VSMOW	Vienna Standard Mean Ocean Water
WY	Water year
$\delta^{18}O$	The deviation of sample ^{18}O:^{16}O from a standard ^{18}O:^{16}O

ARs and PE ARs shape southwest BC's hydroclimate:

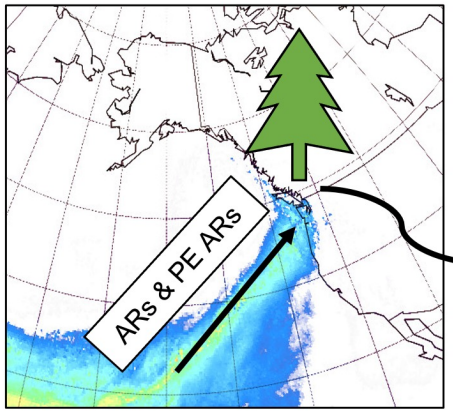

ARs deliver intense precipitation

PE ARs deliver intense, $\delta^{18}O$-enriched precipitation

Can dendrochronological records reconstruct AR and PE AR history in southwest BC?

Methods

1. Core trees in southwest BC
2. Measure trees' radial growth and α-cellulose $\delta^{18}O$
3. Compare radial growth and $\delta^{18}O$ with AR and PE AR variability using GAMs

Results

Radial growth-AR relationships:

Increasing radial growth is associated with…

↑ Total AR count
↓ Intense (90th percentile) AR count

Primary control mechanisms: snowpack, infiltration capacity, infiltration rate

α-cellulose $\delta^{18}O$-PE AR relationships:

Increasing $\delta^{18}O$ is associated with…

↷ Summer % PE AR precipitation
↓ Spring % PE AR precipitation
↑ Annual PE AR count
↝ Annual % PE AR precipitation

Primary control mechanisms: humidity & snowpack

Conclusions: Radial growth = weaker proxy
α-cellulose $\delta^{18}O$ = stronger proxy

Map retrieved from CIMSS (2024).

Chapter 1.

General Introduction

1.1. Summary

Anthropogenic climate change is distorting the global water cycle, particularly through shifts in the patterns and intensities of hydrological extremes (Douville et al., 2021). This intensification of extreme rainfall and droughts poses severe risks to human livelihoods, agricultural systems, economies, and water resources worldwide (Intergovernmental Panel on Climate Change, 2022). Along the southwest coast of British Columbia (BC) and northwest coast of the conterminous United States (US), hereinafter referred to as the Pacific Northwest (PNW), extreme precipitation in the form of atmospheric river (AR) storms has important impacts on the region's water budgets (Dettinger, 2013; Eldardiry et al., 2019; Goldenson et al., 2018; Metro Vancouver, 2019a). However, the lack of multi-century long historical records of AR trends limits the ability of PNW water resource managers to account for these storms in future planning. Such data are especially crucial as the region grapples with climate change-induced shifts to snowpack, streamflow, and summer water availability (Metro Vancouver, 2019b; Seattle Public Utilities, 2019; Vano et al., 2015). To this end, this research evaluates two dendrochronological approaches, tree ring width and $\delta^{18}O$ in tree ring cellulose, for their novel use as proxy records of historical AR trends in southwest BC, Canada.

1.2. Background

Atmospheric rivers are filamentary hydrological features, thousands of kilometres long and hundreds of kilometres wide, that transport large volumes of water vapour and deliver intense precipitation to mid-latitude coastlines (Ralph et al., 2018; Ralph & Dettinger, 2011). These synoptic-scale plumes are responsible for over 90% of the globe's water vapour flux from the tropics toward the poles (measured as vertically integrated horizontal water vapour flux) (Zhu & Newell, 1998), with some ARs transporting water at a rate of fifteen Mississippi Rivers combined (Ralph et al., 2018; Ralph & Dettinger, 2011). When AR paths intersect coastal or inland mountain ranges, the storms release intense orographic precipitation (Ralph & Dettinger, 2011), giving way

to the flooding, landslides, and infrastructure damage often associated with ARs (Payne et al., 2020). As a result, ARs are responsible for 84% of flood damages in the western US (1978-2017) (Corringham et al., 2019).

ARs also bring important impacts to North American water resources, including in the PNW. The PNW experiences Mediterranean and oceanic climates, with mild, wet winters followed by dry summers (Peel et al., 2007). This drives many PNW watersheds' hybrid runoff regimes, wherein mountain snowpacks accumulate in cold seasons and melt in warmer months (Pike et al., 2011). These snowpacks function as natural reservoirs; they hold the region's winter precipitation until the spring and early summer, when warm temperatures melt the snow and release water to downstream environments (Vano et al., 2015). Through this system, snowpacks provide in-season water resupply to human-made reservoirs, and this resupply is necessary to meet the PNW's municipal, agricultural, and industrial water demands (Vano et al., 2015 and refs. therein). ARs, as predominantly cold-season phenomena (Mundhenk et al., 2016), interact with this snowmelt-reliant system. Although AR precipitation is generally associated with beneficial snowpack contributions in western North America (Eldardiry et al., 2019), PNW ARs tend to degrade snowpacks through rain-on-snow events (Chen et al., 2019; Eldardiry et al., 2019), challenging the PNW's water resources. At the same time, warm-season ARs can relieve droughts, and ARs have broken 60-74% of all persistent droughts between 1950 and 2010 in the US PNW (Dettinger, 2013). Understanding AR frequency and seasonality, then, is crucial in determining the PNW's ability to meet its water demands.

Climate change is likely to compound AR effects on PNW water resources. Warmer temperatures are projected to reduce winter snowpacks, straining the PNW's snowmelt-fed regime (Siirila-Woodburn et al., 2021). In one PNW watershed serving the municipal water supply of Metro Vancouver, BC, a >90% decrease in peak wintertime snow water equivalent (SWE) is projected for the 2080s under a high-emissions scenario (RCP 8.5) (Dierauer et al., 2021). Such decreased SWE can exacerbate summer streamflow droughts (Dierauer et al., 2021) and strain the region's water resources (Metro Vancouver, 2019b; Siirila-Woodburn et al., 2021), especially during the PNW's projected longer summer dry spells (Curry & Sobie, 2023; Mote & Salathé, 2010). Considering ARs' ability to break and create droughts, ARs are likely to increasingly interact with PNW hydroclimate extremes as the climate warms.

Climate change is also affecting ARs themselves, bringing additional hazards. As greenhouse gas emissions increase global ocean and atmospheric temperatures, the intensity of ARs is rising (Baek & Lora, 2021). Warmer oceans and air are projected to increase atmospheric moisture (Held & Soden, 2006), enhancing the frequency, duration, size (Rhoades et al., 2020), and precipitation intensity of AR storms (Payne et al., 2020). Climate change-derived AR intensification has already begun; for example, climate change made a 2021 AR in the PNW 45% more likely (Gillett et al., 2022). This AR's heavy precipitation caused flooding, landslides, and major evacuations; cut off Vancouver, BC from the rest of Canada by rail and road; and led to five fatalities (Gillett et al., 2022). Considering climate change's intensification of ARs and their hazards, there is a growing interest in understanding the interannual frequency and intensity of AR storms to better accommodate their hydroclimate impacts (Ralph et al., 2017).

A climate change-altered precipitation regime in the PNW is also likely to affect the region's vegetation. PNW vegetation is finely adapted to mild summers and cool, wet winters, and shifts to this system will lead to cascading, ecosystem-level impacts (Shanley et al., 2015). These impacts may particularly manifest in PNW forests, where longer summer dry periods, decreased snowpack, and increased drought stress will likely affect tree growth and productivity (Albright & Peterson, 2013; Case et al., 2021). With more of the region's precipitation arriving from ARs (Gershunov et al., 2019), AR interannual variability may increasingly play a role in tree growth; recent studies have begun examining this relationship (Borkotoky et al., 2023; Howard et al., 2023; Steinschneider et al., 2018).

Knowledge of historical AR storm patterns is essential for contextualizing current and future AR trends. However, quantification of AR variability has traditionally been limited to the mid-20th century satellite era (Shields et al., 2018), impeding the ability to evaluate present and future ARs. Dendrochronological records, alternatively, can serve as effective proxy records for past weather extremes and climate many centuries older than instrumental or satellite reanalysis records (Speer, 2010). Such historical reconstructions are possible because trees generally grow a distinct ring each year and because tree growth can be climate-limited; for example, drought-intolerant trees might grow narrower rings in drier years than wetter years (Speer, 2010). If yearly tree ring width, a common dendrochronological measurement, correlates strongly with instrumental records of a climate variable, then ring width can serve as an annually-

resolved proxy record of that climate variable that extends beyond the instrumental record. In the PNW, tree ring width records have added to knowledge of past streamflow (Littell et al., 2016), groundwater levels (Hunter et al., 2020), SWE (Mood et al., 2020), summer temperature (Pitman & Smith, 2012), precipitation (Dannenberg & Wise, 2016), and snow drought (Harley et al., 2020), with some reconstructions as old as eight centuries (Littell et al., 2016). Recent research has indicated the potential for tree ring widths to record centuries-long AR history on the US west coast (Borkotoky et al., 2023; Gupta et al., 2023; Howard et al., 2023; Steinschneider et al., 2018). However, radial growth records have not yet been tested for their use as an AR proxy in southwest BC.

Tree ring stable isotopes are another dendrochronological record that documents past climates. Isotopes with heavier atomic weights cycle through the environment differently than their lighter counterparts, and climatic controls on that cycling can correlate strongly with stable isotope compositions measured in tree rings (McCarroll & Loader, 2004a). Stable isotope dendrochronology applications are diverse, with relationships identified between tree ring stable isotopes and climate variables such as humidity (G. Xu et al., 2022), soil moisture (Tei et al., 2013), moisture source (Labotka et al., 2016), precipitation amounts (Roden & Ehleringer, 2007; C. Xu et al., 2013), cyclone activity (Miller et al., 2006), and the phases of climate oscillations such as the El Niño Southern Oscillation (Brienen et al., 2012), the Pacific Decadal Oscillation (PDO) (C. Xu et al., 2019), and the Arctic Oscillation (AO) (Churakova Sidorova et al., 2021; Dinis et al., 2019).

In the PNW, where plant growth is less water-limited than other parts of the world (Nemani et al., 2003), stable isotope dendrochronology is a valuable option for recording annual hydroclimate histories (Ratcliff et al., 2018). Currently, a stable isotope tree ring proxy record has not been created for North American west coast AR storm variability; this gap likely exists because AR precipitation's $\delta^{18}O$ and $\delta^{2}H$ isotopic ratios are not substantially different from those of non-AR precipitation (Greenblat et al., 2024; McCabe-Glynn et al., 2016). However, Pineapple Express (PE) storms, a category of ARs that transport water vapor from the subtropical Pacific Ocean to the North American west coast (Shields & Kiehl, 2016b), exhibit potential for appearing in tree ring stable isotope records due to their precipitation's enriched $\delta^{18}O$ relative to non-PE precipitation (Oster et al., 2012; Spry et al., 2014). The potential capture of enriched $\delta^{18}O$ from PE AR storms in tree ring cellulose, and the associated relationships between tree ring $\delta^{18}O$

and interannual PE variability, were first studied in Spry (2013), though a multi-tree $\delta^{18}O$ record has not yet been evaluated for its use as a PE proxy.

1.3. Purpose and Objectives

The potential extension of AR history using dendrochronological methods carries substantial implications for water resource management in the PNW. Dendrochronological records of water extremes have already demonstrated their management utility across North America; applications include the measurement of drought return periods (Kwon & Lall, 2016), the estimation of reservoir sizes (Patskoski & Sankarasubramanian, 2015), and the contextualization of modern river and stream gauge data (Meko & Woodhouse, 2011). For ARs, the extension of their historical patterns beyond instrumental records using dendrochronological methods would allow for a more comprehensive evaluation of their long-term interannual frequency. This, in turn, would allow for improved contextualization and management of current and future ARs in a changing climate.

This research explores two dendrochronological methods — tree ring width records and records of $\delta^{18}O$ in tree cellulose — for their ability to record drought and AR variability in the PNW. To do so, this thesis presents tree ring records for Pacific silver fir and Douglas-fir in two coastal watersheds on the southwest coast of BC. This thesis also presents records of AR and PE AR frequency, and their annual contribution to precipitation for the study region, using satellite reanalyses and weather station data. The tree ring records are then compared with the AR and PE AR records using Generalized Additive Models (GAMs) to evaluate whether and how these dendrochronological methods function as proxy records for AR and PE AR variability.

In Chapter 2, I present Pacific silver fir radial growth records from southwest BC and analyze their potential to record AR variability. I establish annual and earlywood radial growth chronologies for Pacific silver fir, a species potentially responsive to AR trends due to their sensitivity to low moisture availability (Klinka et al., 1999), then assess their relationships with AR variability using Generalized Additive Models (GAMs). Likely determinants of tree radial growth, including temperature, snowpack, and climate oscillations such as El Niño Southern Oscillation are also included in the GAM to identify whether AR data explain tree growth variability not explained by other climate variables.

To clarify the interpretation of AR effects on tree growth, I also evaluate concurrent impacts of ARs and summer drought on tree growth using *t*-tests. These results are discussed in the context of other tree ring width reconstructions of AR variability from western North America.

In Chapter 3, I present Douglas-fir $\delta^{18}O$ records from southwest BC and analyze their potential as a proxy for PE AR storm variability using GAMs. Known environmental determinants of tree ring $\delta^{18}O$, such as snowpack, relative humidity, and climate oscillations, are included in the GAM analyses to identify whether PE AR data explain tree ring $\delta^{18}O$ variability not explained by other climate variables. These results are discussed in a PNW water management context with consideration of PEs' ability to compound the effects of climate change on future PNW snow and streamflow droughts.

In these chapters, two dendrochronological records, ring width and $\delta^{18}O$, are assessed as potential proxy records of southwest BC's historical AR and drought variability. Together, they present a deeper understanding of the region's paleohydroclimate variability and situate these hydrological extremes – and their water management implications – within the PNW's climate change projections.

Chapter 2. Evaluating AR and Drought Effects on Tree Radial Growth in Southwest BC

2.1. Introduction

Atmospheric rivers (ARs) are filamentary hydrological features of the lower troposphere, thousands of kilometres long and hundreds of kilometres wide, that transport large volumes of water vapour and deliver intense precipitation to mid-latitude coastlines (Ralph et al., 2018; Ralph & Dettinger, 2011). ARs dramatically affect hydroclimates, with their characteristic extreme precipitation producing flood conditions (Barth et al., 2017; Lavers et al., 2011; Neiman et al., 2011; Payne et al., 2020), relieving drought conditions (Dettinger, 2013; Dettinger et al., 2011), and modulating winter snowpacks (Eldardiry et al., 2019). As climate change increases ocean and air temperatures, ARs are projected to increase in frequency, duration, size (Rhoades et al., 2020), and precipitation intensity (Baek & Lora, 2021; Payne et al., 2020). These changes to ARs are likely to amplify both AR flood hazards (Corringham et al., 2019) and ARs' impacts on water resources (Chen et al., 2018; Dettinger et al., 2011). In this context, there is a growing interest in understanding the interannual frequency and intensity of AR storms to better accommodate their hydroclimate impacts (Ralph et al., 2017).

Knowledge of historical AR patterns is essential to plan for future AR variability, but data on past AR variability has traditionally been limited to the mid-20th century satellite era (Shields et al., 2018). These few available decades of satellite AR records may poorly capture ARs' long-term variability, as low-frequency, multi-decadal climate oscillations appear to affect AR patterns (X. Liu et al., 2016; Mantua & Hare, 2002). Tree ring records, meanwhile, are an annually precise and reliable measure of past climates and weather extremes many centuries older than instrumental or satellite records (Speer, 2010). Tree radial growth records have been used to reconstruct past hydroclimates globally (e.g., Ljungqvist et al., 2020; Steiger et al., 2018), including recent advances in reconstructing North American west coast AR trends (Borkotoky et al., 2023; Gupta et al., 2023; Howard et al., 2023; Steinschneider et al., 2018). However, no tree ring-based interannual AR reconstruction exists for the study area of southwest British Columbia (BC).

Southwest BC's hydroclimate complicates the creation of such an AR reconstruction. This region experiences higher annual precipitation than the North American Pacific coast to the south (Schneider et al., 2017), making its trees less moisture-limited (Coulthard & Smith, 2016; Nemani et al., 2003), and therefore less likely to record precipitation variability, than trees growing in AR-affected regions to the south. This trend was documented in Borkotoky et al. (2023), who found that western United States (US) tree ring records more precisely reconstructed southwest US AR variability than northwest US AR variability. However, despite their relative lack of moisture limitation, trees in southwest BC have been found to record precipitation inputs (Mood & Smith, 2021; St. George, 2014). In southwest BC and the northwest conterminous United States (hereinafter, Pacific Northwest [PNW]), winter precipitation tends to limit radial growth (St. George, 2014) due to large snowpacks delaying the start of growing seasons (Kirdyanov et al., 2003; Sanmiguel-Vallelado et al., 2019; Watson & Luckman, 2016). A smaller number of PNW radial growth records do positively correlate with winter precipitation (St. George, 2014), likely a result of snowmelt's contribution to soil moisture during growing seasons (St. George, 2014; Watson & Luckman, 2016). ARs occur more frequently in cold seasons (Mundhenk et al., 2016), and cold-season AR precipitation may affect radial growth by either delaying the growing season or increasing soil moisture during growing seasons.

However, the influence of cold-season ARs on southwest BC's snowpack, and therefore on radial growth, is not definitive. While North American Pacific coast cold-season ARs are thought to result in positive snow accumulation (Eldardiry et al., 2019), this trend primarily holds for the high-elevation Sierra Nevada mountains (Eldardiry et al., 2019). Meanwhile, cold-season ARs affecting the US PNW tend to result in negative snow water equivalent (SWE) changes, likely due to the region's warm storm temperatures and resulting enhanced snow ablation (Chen et al., 2019). This suggests that frequent PNW winter ARs may challenge, rather than benefit, PNW snowpacks. The direction of AR-derived SWE change is also confounded by southwest BC's AR temperatures, with the nearby Cascade Range in Washington, USA, experiencing AR temperatures more evenly split above and below freezing levels than California's Sierra Nevada mountains, whose AR days are more frequently below 0°C (Hu & Nolin, 2019). Additional complications to the interpretation of AR effects on southwest BC's snowpack include the timing of cold-season ARs, as the extent of positive and negative SWE

accumulation from ARs varies by the month of a storm's occurrence (Eldardiry et al., 2019). Despite these intricacies, the success of Borkotoky et al. (2023) in reconstructing AR variability using radial growth records in the US PNW, which experiences a similar climate to that of southwest BC (Peel et al., 2007), indicates that such a record is possible for southwest BC. The exact mechanisms for an AR effect on radial growth, though, are complex.

Differences in moisture availability between seasons may additionally obscure AR-radial growth relationships in southwest BC and elsewhere. ARs, as primarily cold-season phenomena (Mundhenk et al., 2016), may enhance or constrain radial growth through SWE effects as described, but be followed low-precipitation summers, which can independently affect radial growth (e.g., Crawford et al., 2015). Inter-seasonal moisture availability and its effects on radial growth may be especially impactful in a southwest BC context; growing-season precipitation inputs in the region are typically less than half that of cold-season precipitation inputs (ECCC, 2023c), making growing-season moisture availability potentially more limiting to radial growth than cold-season precipitation inputs. As such, an evaluation of southwest BC's AR-radial growth relationship requires examination of the concurrent effects of cold-season AR precipitation and summer moisture availability on radial growth.

The creation of a long-term, tree ring-based record of past southwest BC AR variability would be highly informative for the region's water resource management. Coastal and near-coastal southwest BC watersheds experience hybrid runoff regimes, with snowmelt and rainfall both determining moisture availability and the extent of summer low streamflow (Pike et al., 2011). The region's mountain snowpacks serve as natural reservoirs under this regime, with snowmelt offsetting low summer precipitation and providing water for municipal, agricultural, fisheries, and industrial needs in warmer and drier months (Metro Vancouver, 2019b; Pike et al., 2011; Vano et al., 2015 and refs. therein). As the climate warms, snowmelt contributions to summer streamflow are projected to weaken or disappear entirely (Pike et al., 2011), and municipal water managers in the region have identified a need to expand future water storage capacity to more extensively retain winter precipitation (Metro Vancouver, 2019b). ARs strongly impact this winter precipitation (Sharma & Déry, 2020), with currently-variable snowpack effects (Chen et al., 2019; Eldardiry et al., 2019) and a shift toward more AR precipitation falling as rain than snow as the climate warms (Gonzales et al., 2019).

Considering this context, a more comprehensive understanding of the frequency and extent of past ARs would be highly useful in planning for future water resource needs.

This study evaluates the capacity of radial growth records from trees in southwest BC that experience winter snowpacks to record AR variability. Considering the climatic complexities shaping these records, this study uses a Generalized Additive Model (GAM) approach. GAMs model a response variable (e.g., radial growth) as a sum of non-linear functions of multiple predictor variables (e.g., ARs and other climate variables) (Wood, 2017) and allow for an assessment of what combination of predictor variables best explain the response variable. Using GAMs, this study evaluates AR data for their ability to explain tree radial growth relative to known predictors of radial growth in southwest BC. These alternative predictors of radial growth include precipitation amount (Crawford et al., 2015; Dannenberg & Wise, 2016; St. George, 2014), temperature (Larocque & Smith, 2005; Pitman & Smith, 2012; Starheim et al., 2013), snowpack (Mood & Smith, 2021; Starheim et al., 2013), and the phases of climate oscillations affecting the region (St. George, 2014). For this study, AR data are assembled by multiple seasonal and annual metrics – total AR count, intense AR count, and ARs' percent contribution to total precipitation – to further clarify AR impacts on radial growth. This study also evaluates sub-annual ring widths for their potential to record AR variability, as sub-annual rings may record seasonal signals unresolvable in annual ring widths (Dannenberg & Wise, 2016). Additionally, this study examines the interactive effects of cold-season ARs and warm-season drought on tree radial growth to inform interpretations of the AR-radial growth relationship.

2.2. Methods

2.2.1. Study area

Core samples were collected from Pacific silver fir (*Abies amabilis*) trees in the Malcolm Knapp Research Forest (MKRF) to study the relationships between radial growth, interannual AR variability, and drought. The PNW is a moisture-rich region (PRISM, 2024) with trees that are less moisture-limited than other parts of North America (Coulthard & Smith, 2016; Nemani et al., 2003). To maximize the likelihood of identifying an AR signal in a PNW radial growth record, this study evaluated Pacific silver firs, as this species has the highest water demand of any evergreen tree in BC

(Klinka et al., 1999) and a low tolerance for water deficits (Province of British Columbia, 2024). Considering ARs' ability to contiribute to (via snowpack loss) and end drought conditions (Dettinger, 2013), it was reasoned that the high water demand of Pacific silver firs and their poor tolerance for water deficits may increase the species' ability to record AR precipitation variability in their radial growth compared to other species in the region.

The Pacific silver fir study site, referred to as MKRF-1, is located on q̓iċəy̓ (Katzie) and Stó:lō land (Katzie First Nation, 2024; Stó:lō Research and Resource Management Centre, 2016) within the North Alouette Watershed, 50 km east of Vancouver, BC. This site was selected for its accessible location within a research forest, for its nearby climate station, and for the Pacific silver fir trees located at the site. MKRF-1 has a mean elevation of 441.42 m above sea level, a southwest aspect, a 5-15° slope, and is located within the Coastal Western Hemlock very wet maritime (CWHvm1) biogeoclimatic zone (B.C. Ministry of Forests, 2021). Characteristic of the CWHvm1 zone, this area experiences mild winters and cool summers with frequent hot and dry stretches (Meidinger & Pojar, 1991). The study area receives a mean annual precipitation of 2180 mm and has a mean annual temperature of 9.9°C (1981-2010 climate normals; (ECCC, 2023c)). As a whole, this climate supports the site's tree cover of western hemlock (*Tsuga heterophylla*), western redcedar (*Thuja plicata*), Pacific silver fir (*Abies amabilis*), and grand fir (*Abies grandis*) and the understory of primarily salal (*Gaultheria shallon*), deer fern (*Blechnum spicant*), red huckleberry (*Vaccinium parvifolium*), and Alaskan blueberry (*Vaccinium alaskaense*). The study site was last logged between 1920 and 1931. In 1931, a large fire burned the site, and the forest has since regenerated naturally except for tree thinning in 2002 and 2003 (I. Aron, personal communication, October 31, 2022). The exact location of MKRF-1 was selected as it was known to have avoided more recent fires that have prevented Pacific silver fir growth elsewhere in the MKRF (I. Aron, personal communication, October 31, 2022). Presently, the site is surrounded by active logging and newly planted tree stands. MKRF-1 is located 6.2 km southwest of the MKRF-2 site described in Chapter 3 (Figure 2.1).

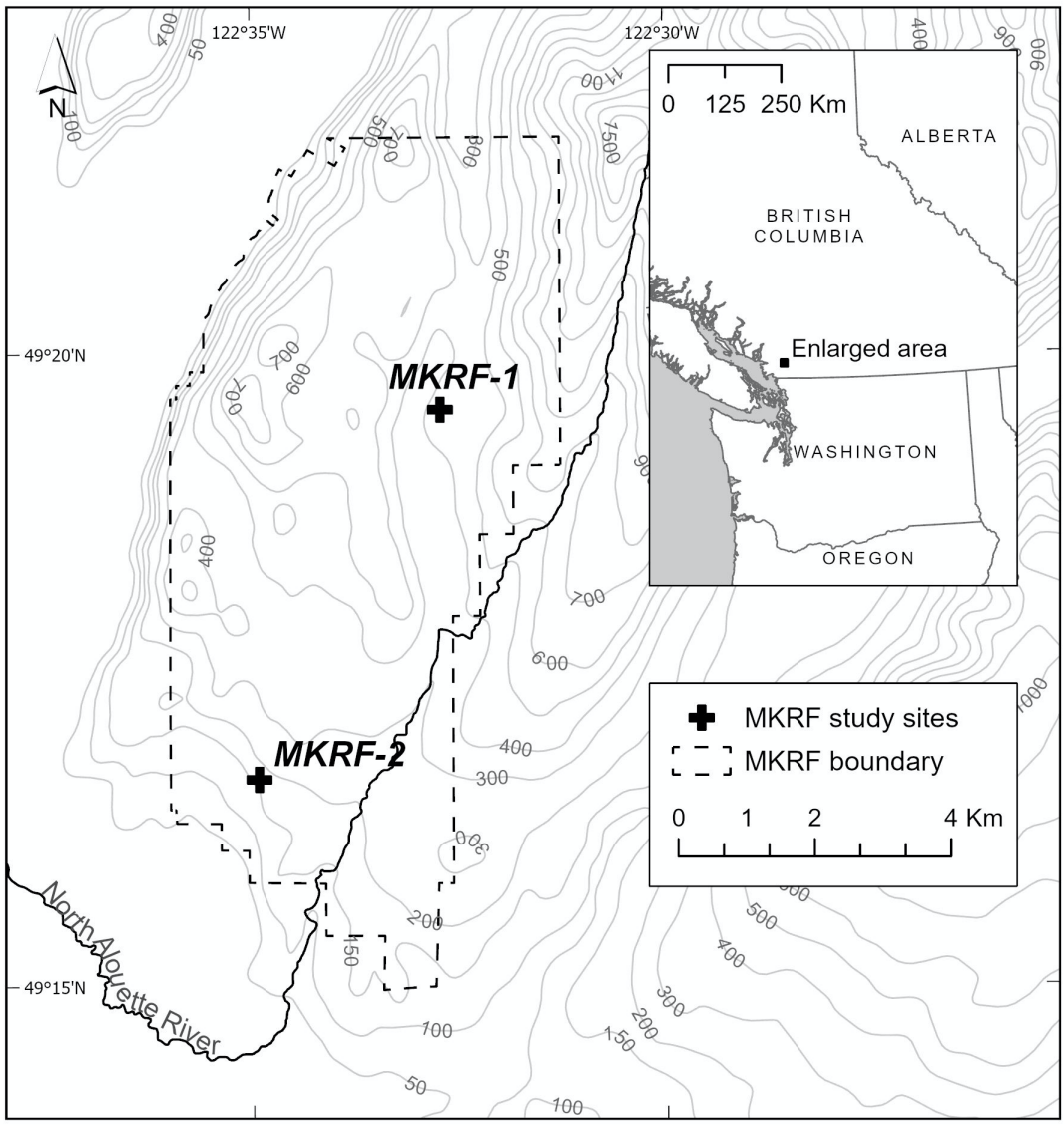

Figure 2.1 Location and extent of the MKRF and the locations of the two sites sampled within the MKRF described in Chapters 2 and 3.

The MKRF-1 study area has a rainfall-dominated hydroclimate regime with ephemeral winter snow cover (Leach & Moore, 2014) (Figure 2.2). Precipitation varies seasonally, with higher precipitation in the fall and winter (ONDJFM) than in the spring and summer (AMJJAS) (Figure 2.2). MKRF-1 is located within a watershed experiencing

high-elevation seasonal winter snowpack, exemplified with data from the nearest high-elevation climate station in Figure 2.2B.

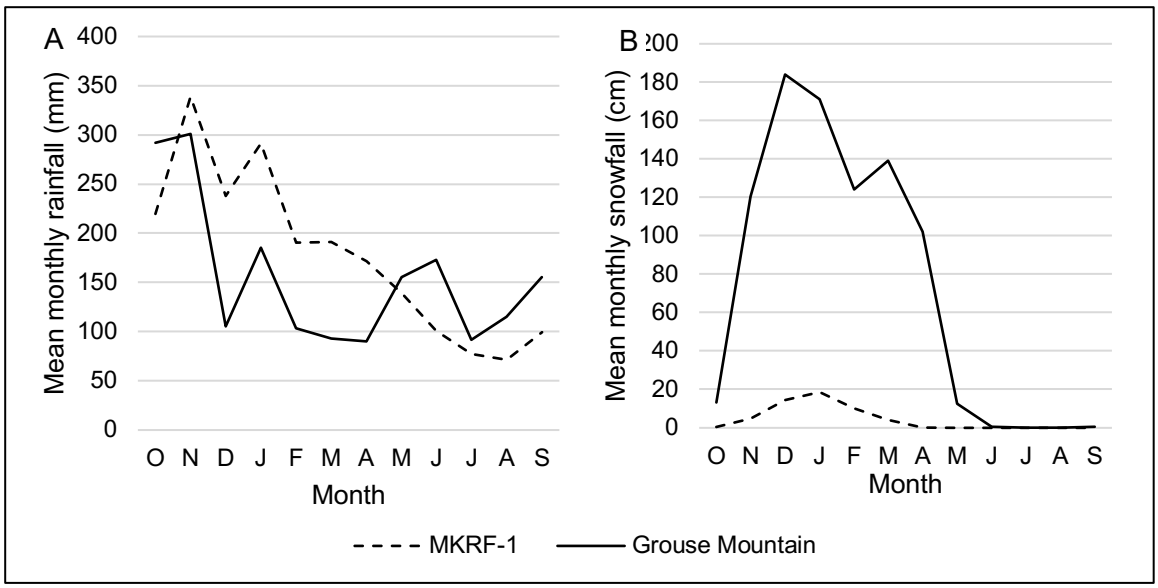

Figure 2.2 **(A) Mean monthly rainfall and (B) snowfall at MKRF-1 and the Grouse Mountain climate station, 1981-2010. MKRF-1 data are sourced from the nearest available climate station (Haney UBC RF Admin, Station ID: 1103332). The Grouse Mountain station is approximately 45 km from MKRF-1 and is 1103.00 m above sea level. Data sources: MKRF-1, (ECCC, 2023c); Grouse Mountain (ECCC 2024).**

2.2.2. Sampling and ring width measurement

In fall 2022, winter 2022-2023, and spring 2023, Pacific silver firs were cored at MKRF-1 (Figure 2.1). Due to the limited number of Pacific silver firs within the MKRF and at MKRF-1, trees were selected for coring according to a targeted sampling design in which all living Pacific silver firs within a 0.25 km radius of a known Pacific silver fir stand (49.328538, -122.542705) were cored. Tree cores were collected with a 5-mm increment borer at the standard 1.35 m from the tree base. Table A1 lists the locations and details of the cored trees. Fifteen trees were cored with two complete cores collected per tree for cross-dating purposes. This sample size satisfied an expressed population signal (EPS) > 0.85 over the years of the available precipitation record (described in section 2.2.3), indicating that the ring width record was adequately common among the sampled population and not dominated by an individual tree or trees

(Speer, 2010). EPS was calculated using the dplR R package (Bunn, 2008) with the following equation:

$$EPS = \frac{t \times \overline{r}}{t \times \overline{r} + (1 - \overline{r})} \quad (2.1)$$

wherein t was the average number of tree series using one core per tree and $\overline{r}$ was the mean between-tree correlation (Speer, 2010).

To develop a ring width chronology for the site, the tree cores were first sanded, dated, and cross-dated following the standard methodology described in Speer (2010). Sanding of the tree cores was completed with a belt sander followed by hand-sanding with successively finer grit to resolve the details of the rings. To assign calendar years to the tree rings and cross-date the cores, both the list method and the cross-dating program COFECHA were applied. The list method involves counting annual rings backwards from the most recent year of growth, identifying narrow ring years for each core, and comparing those years between cores to confirm the accuracy of the counted years and to detect potential missing or duplicate rings (Yamaguchi, 1991). To further validate the tree ring dating, secondary cross-dating was completed with the COFECHA program (Grissino-Mayer, 2001; Holmes, 1983).

To establish radial growth records, the cores were scanned at 2400 dots per inch (DPI) with an Epson V39 Flatbed Scanner. Then, ring widths were measured with the CooRecorder program (Cybis Dendrochronology, 2022). The CooRecorder “auto-place” function was utilized to systematically identify boundaries between earlywood and latewood. These earlywood and latewood boundaries were then visually evaluated, and any auto-place boundary errors were resolved. Then, site-wide earlywood, latewood, and annual radial growth datasets were compiled using the program CDendro (Cybis Dendrochronology, 2022). For trees sampled in April through October (i.e. while the trees may have been growing), the youngest growth rings were omitted from trees’ ring width records in CDendro as they may have not represented a full season of earlywood and/or latewood development. Following ring width measurement and cross-dating, the ring width records were standardized to a negative exponential curve to remove age-related growth trends using the R package dplR (Bunn, 2008). This detrending method was selected as it retains interdecadal variability (Cook & Kairiukstis, 1990), which AR activity is known to exhibit (Gershunov et al., 2017). The resulting detrended ring width

records were compiled into earlywood, latewood, and annual ring site chronologies spanning 1931 through 2021.

2.2.3. Sourcing AR and climate data

AR data

To analyze relationships between radial growth and interannual AR variability, AR data for southwest BC were obtained from the SIO-R1 catalogue developed by Gershunov et al. (2017). SIO-R1 is currently the longest-spanning AR reanalysis record available, and its long temporal overlap with the MKRF-1 chronologies makes it well suited for this study. The SIO-R1 catalogue identifies AR events and their vertically integrated horizontal vapour transport (IVT), integrated water vapour (IWV), wind direction, and landfalling latitude and longitude using National Centers for Environmental Prediction/National Center for Atmospheric Research (NCEP/NCAR) atmospheric reanalysis (Gershunov et al., 2017). SIO-R1 classifies ARs as features with contiguous grid cells spanning 1500 km or more in which IVT is greater than 250 kg/m/s, IWV is greater than 15 mm, and which cross the North American Pacific coastline between 32.5 and 52.5°N. This catalogue extends from January 1948 through the present and has a 2.5°, 6-hourly resolution (Gershunov et al., 2017). To determine annual AR counts within the study region, ARs with a central landfalling location within the grid cell covering the study area (the grid cell bounded by 47.5°N, 50°N, 125°W, 122.5°W, Figure 2.3) were extracted from the larger dataset. To align the 6-hourly AR data with daily precipitation records, the AR data were upscaled to daily records by considering days with at least one AR time step as AR days. Then, AR days were summed by water year[1] (WY) and season (JFM, AMJ, JAS, and OND) to determine WY and seasonal AR counts.

[1] North American water years are October 1 to September 30 and are named by the calendar year in which they end.

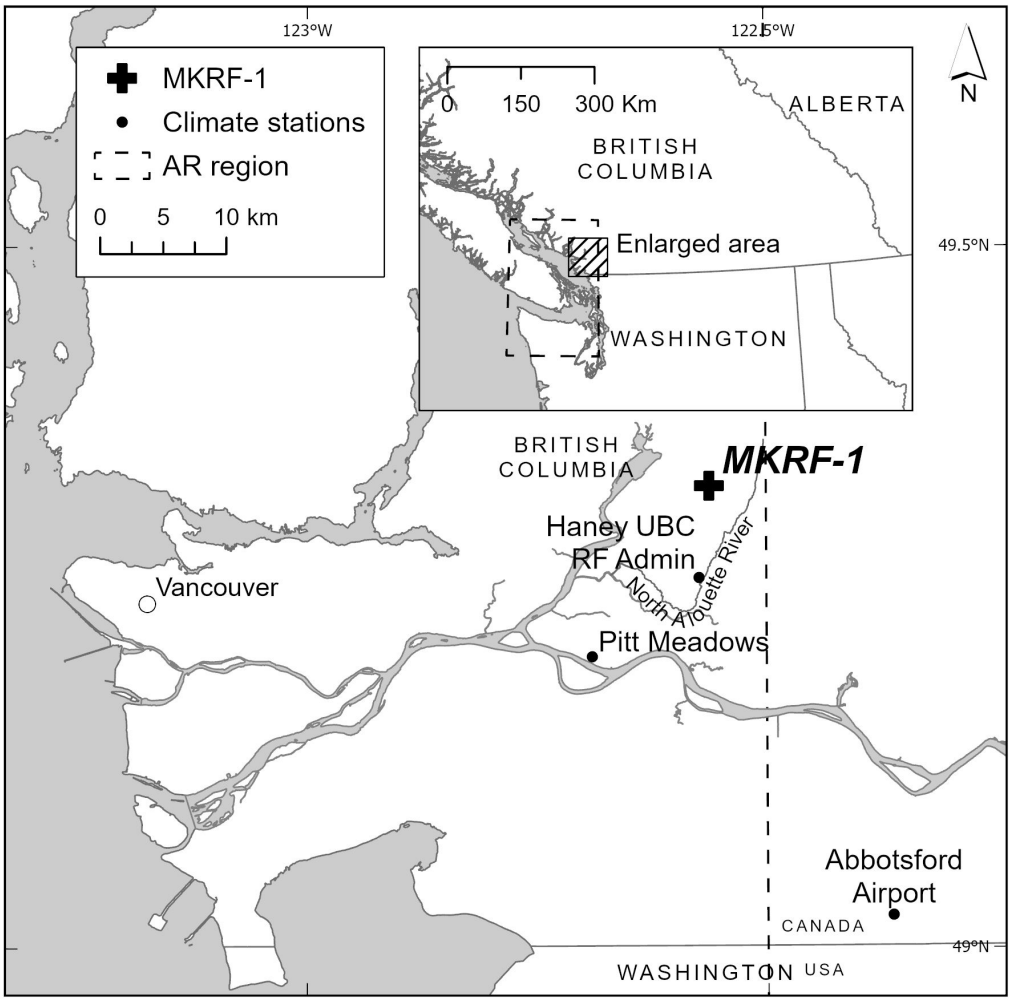

Figure 2.3 Location of the MKRF-1 study site, SIO-R1 AR data region, and climate stations.

Two additional AR variables with the potential to capture AR effects on tree growth were included in the analysis: percent AR precipitation and intense AR count. To calculate percent AR precipitation (i.e., the percentage of the total annual or seasonal precipitation occurring on AR days), the precipitation occurring on AR days was divided by the total precipitation for the corresponding WY or season. Precipitation data sources are described below. For intense AR count, intense AR days are defined as AR days at or above the 90th percentile of daily precipitation (i.e., days with precipitation totals higher than 90% of the compiled daily records). The 90th percentile and above is commonly used to define intense AR precipitation (e.g., Chen et al., 2018; Hagos et al., 2016; Najibi & Steinschneider, 2023; Ramos et al., 2018), informing its use here.

To further understand the AR storms affecting the west coast of North America, the fraction of ARs approaching the study area from the southwest was calculated. This was used to approximate the fraction of ARs that were Pineapple Express (PE) storms, as PEs originate in the subtropical Pacific Ocean and approach the west coast of North America from the southwest (Dettinger, 2004). PEs carry unique hydroclimate impacts relative to non-PE ARs (Gonzales et al., 2022), discussed in Chapter 3. To calculate the fraction of all SIO-R1 ARs which were PEs, the number AR time steps with positive u and v wind vectors (i.e. approaching from the southwest) was divided by the total number of AR time steps over the catalogue's 1949-2021 range.

Climate data

To determine whether AR variability showed a unique signature in MKRF-1 radial growth records, AR data were analyzed alongside other climate variables likely to affect the trees' radial growth. One variable, precipitation amount, has been shown to correlate with PNW tree ring width records (Crawford et al., 2015; Dannenberg & Wise, 2016; St. George, 2014). The mostly negative trend between PNW radial growth and winter precipitation in particular is likely due to heavier snowpacks delaying the start of cambial activity in the spring (St. George, 2014). These relationships vary by season and precipitation variable; for example, Crawford et al. (2015) reported significant positive relationships with April-June precipitation and Dannenberg & Wise (2016) reported significant positive relationships with cool-season extreme low precipitation.

For this study, precipitation data were taken from the nearest climate station to MKRF-1, Haney UBC RF Admin (Station ID: 1103332). This station is 1.85 km southeast of MKRF-1 and its record spans WYs 1962-2021 (Figure 2.3). Some data were missing from this record, so to assemble a complete daily precipitation record, a "shift factor" approach was applied. Precipitation data were obtained from the next-nearest weather station to MKRF-1 with temporally overlapping records, Abbotsford Airport (Station IDs: 1100030, 1100031). Then, both the Abbotsford Airport and Haney UBC RF Admin daily precipitation records were averaged for every month of their record. These monthly values were then averaged by decade, e.g. 1970s July mean daily precipitation at Abbotsford Airport, 1980s July mean daily precipitation at Abbotsford Airport, etc. The difference between corresponding months' decadal averages at the two stations were calculated for each decade; these differences are referred to as "shift factors." For days

missing data from the Haney UBC RF Admin record, the Abbotsford Airport monthly mean daily precipitation for the corresponding month was summed with the corresponding shift factor; the resulting value was added to the Haney UBC RF Admin record. This method allows for an estimation of a day's precipitation at Haney UBC RF Admin while adjusting for mean monthly and decadal-scale differences in precipitation at the two stations. For days with data missing at both Haney UBC RF Admin and Abbotsford Airport, the same shift factor approach was applied using precipitation data from Pitt Meadows CS (Station ID: 1106178). The combination of these three stations' data created a continuous daily precipitation record representative of average monthly and decadal conditions at the Haney UBC RF Admin station.

Interannual temperature data were also included in the analysis, as tree radial growth has been identified as responding to temperature variability in the PNW. Larocque & Smith (2005) identified positive relationships between radial growth and July mean air temperature in BC's southern Coast Mountains, while Pitman & Smith (2012) identified positive significant relationships between radial growth and June-July mean air temperature in BC's central Coast Mountains. Starheim et al. (2013) also found significant positive correlations between radial growth and preceding winter (October-April) mean temperature in the central Coast Mountains. For this study, temperature records were assembled with the same daily climate station data (Haney UBC RF Admin, Abbotsford Airport, and Pitt Meadows CS) and shift factor methods as described for the precipitation record. Mean temperature records were assembled by WY and season for 1962-2021.

Snowpack data were also included in the analysis, as tree radial growth is known to vary with snowpack in southwest BC. For example, Starheim et al. (2013) found significant negative relationships between annual radial growth and end-of-winter SWE in the central Coast Mountains, while Mood & Smith (2021) found significant negative correlations between annual radial growth and April 1 SWE in the southern Coast Mountains. These relationships are both consistent with the regional trends reviewed in St. George (2014), who found predominantly negative relationships between cold season precipitation and radial growth across the PNW. Persistent seasonal snowpacks occur at higher elevations in the study site's watershed (Figure 2.2), and the timing of this snowpack's melt may affect soil temperatures, and therefore the start of springtime transpiration (Mellander et al., 2004), at lower elevations. For this study, NCEP-NCAR

gridded atmospheric reanalysis of daily kg/m^2 of water equivalent of accumulated snow depth were averaged across WYs and included in the analysis. This source was selected as was the highest-resolution continuous SWE record overlapping with the radial growth record available at the time of this study (a 59-year overlap). Complex topography, such as southwest BC's Coast Mountains, has been found to limit the ability of gridded SWE reanalysis records to reconstruct true SWE (Snauffer et al., 2016). However, a continuous SWE record was necessary to calculate mean WY SWE, and this was not available from nearby climate stations, resulting in the use of a gridded SWE reconstruction.

A climate index which combines temperature and precipitation variability, the Standardised Precipitation-Evapotranspiration Index (SPEI), was incorporated into this study for its potential to represent drought conditions better than temperature or precipitation alone. The SPEI considers the effect of potential evapotranspiration on drought severity (Beguería et al., 2010), making it well-suited to assess the impacts of drought conditions on plants compared to other drought indices. For this study, mean seasonal and WY SPEI records for the study area were assembled from Beguería et al. (2023).

Solar radiation data were also included in the analysis for their potential to impact radial growth. Relationships between solar radiation and tree radial growth have been studied elsewhere in North America; for example, Nicklen et al. (2019) found a negative relationship between annual mean potential solar radiation and radial growth in Alaska, while Stahle et al. (1991) found a negative relationship between March-June percentage possible sunshine and radial growth in the central United States. Although relationships between solar radiation and tree radial growth have not been assessed in the PNW, solar radiation is known to generally limit plant growth in southwest BC more than temperature or precipitation (Nemani et al., 2003). For this reason, a proxy for solar radiation – mean cloud cover (MCC) – was included in this study's analysis. While other measures of radiation like Photosynthetically Active Radiation (PAR) are more commonly used to express the portion of radiation affecting plant growth (Ryu et al., 2018), historical PAR records are limited to recent decades (Tang et al., 2022). To maximize the temporal overlap between solar radiation data and the MKRF-1 chronology, MCC data in the form of NCEP-NCAR gridded percentages of cloud cover

were used in this study. These data were averaged across WYs and by season to approximate incoming radiation over the study area.

Multiple climate oscillations also influence tree ring radial growth in the PNW. These include the El Niño Southern Oscillation (ENSO), the Pacific Decadal Oscillation (PDO), the Arctic Oscillation (AO), the Madden-Julian Oscillation (MJO), the North Pacific Gyre Oscillation (NPGO), and the Pacific-North American Oscillation (PNA). ENSO creates warm and dry PNW winters in its El Niño phase and cool and wet winters in its La Niña phase (NOAA PSL, 2023), and PNW tree ring width records have recorded significant positive associations between ENSO indices and radial growth (St. George, 2014; Starheim et al., 2013). In the positive NPGO phase, ocean-to-land moisture transport is enhanced (X. Liu et al., 2016), with Dong et al. (2022) documenting a positive association between tree radial growth and the NPGO index globally. The PDO index, meanwhile, is negatively associated with ocean-to-land moisture transport over the PNW (X. Liu et al., 2016), and radial growth chronologies have shown both significant positive and negative associations with the PDO index (Lyu et al., 2019; St. George, 2014; Starheim et al., 2013) The AO, whose negative phase is associated with more cold air outflow to the mid-latitudes (Thompson et al., 2003), has also shown significant positive correlations with radial growth (D'Arrigo et al., 2003; Y. Liu et al., 2015). The MJO exhibits an alternating negative phase of enhanced convection and rainfall and positive phase of suppressed convection and rainfall (National Weather Service Climate Prediction Center, 2023b), and its variability has also appeared in tree radial growth records (Maxwell et al., 2018). Finally, the PNA, determined by air pressure anomalies over the Pacific Ocean, strengthens the mid-latitude jet stream and is associated with decreased precipitation in the PNW in its positive phase (Z. Liu et al., 2017). PNA variability has also shown significant positive correlations with western North American tree radial growth records (St. George, 2014; Starheim et al., 2013; Trouet & Taylor, 2010).

Many of these oscillations also affect AR variability. Mundhenk et al. (2016) found that more ARs occur in the North Pacific during La Niña than El Niño, and AR activity has been shown to vary significantly with the location of the MJO convective phase (Guan et al., 2012). More ARs also occur in the PNW during the PNA positive phase (Toride & Hakim, 2021). These oscillations and teleconnections have an

interactive relationship with ARs, with the PNA phase modulating the MJO-AR relationship (Toride & Hakim, 2021).

Climate oscillation indices synthesize multiple environmental variables, such as temperature, precipitation, and storm frequency, into a single index. This may allow climate oscillation indices to explain radial growth variability better than a single climate variable alone. Considering ENSO, PDO, MJO, AO, NPGO, and PNA's impacts on the PNW climate, their interactions with AR variability, and their presence in tree ring records, these oscillations were also included in the analysis.

All AR variables, climate variables and climate oscillation indices were assembled by WY and season (JFM, AMJ, JAS, OND), except for mean SWE, which was only assembled by WY. All data sources, including their units, station location or grid cell extent, and record length are described in Table 2.1.

Table 2.1 AR and climate data sources. All records were generated for each variable by water year (WY) and by season unless otherwise noted.

Variable	Description	Data region	Record length (WY)	Time period	Data source
AR variables					
Total AR count	Number of AR days, where an AR day is any day with at least one 6-hour time step classified by Gershunov et al. (2017) as an AR time step.	47.5, 50, -125, -122.5	1949-2021	WY and seasonal	Gershunov et al. (2017)
Intense AR count	Number of AR days exceeding the 90th percentile for daily precipitation at the Haney UBC RF Admin climate station.	47.5, 50, -125, -122.5	1949-2021	WY and seasonal	PE days: Gershunov et al. (2017) Precipitation: (ECCC, 2023d, 2023h, 2023i, 2023j)
% AR precipitation	Percent of total WY and seasonal precipitation occurring on AR days. Precipitation data were sourced from the Haney UBC RF Admin weather station (Climate station ID: 1103332), Abbotsford Airport weather station (Station IDs: 1100030, 1100031) and Pitt Meadows CS weather station (Station ID: 1106178). The combination of these data sources is described below under "total precipitation."	47.5, 50, -125, -122.5	1962-2021	WY and seasonal	PE days: Gershunov et al. (2017) Precipitation: (ECCC, 2023d, 2023h, 2023i, 2023j)

Variable	Description	Data region	Record length (WY)	Time period	Data source
Climate variables					
Total precipitation	Daily precipitation records were sourced from the Haney UBC RF Admin weather station (Station ID: 1103332). For days when this weather station was missing data, the precipitation record was supplemented with data from nearby weather stations: Abbotsford Airport (Station IDs: 1100030, 1100031) and Pitt Meadows CS (Station ID: 1106178). Data from these stations were scaled to Haney UBC RF Admin monthly and decadal averages and combined with the Haney UBC RF Admin record to create a continuous daily record. Data were reported in mm.	Station data: *Haney UBC RF Admin* 49.2645, -122.5732 *Abbotsford Airport* 49.0253, -122.3600 *Pitt Meadows CS* 49.2083, -122.6900	1962-2021	WY and seasonal	Haney UBC RF Admin: (ECCC, 2023j) Abbotsford Airport: (ECCC, 2023d) (ECCC, 2023h) Pitt Meadows CS: (ECCC, 2023i)
Mean temperature	Mean WY temperature was calculated using daily temperature records recorded at the Haney UBC RF Admin weather station (Climate station ID: 1103332). For days with data missing from the Haney UBC RF Admin record, temperature data from Abbotsford Airport (Station IDs: 1100030, 1100031) and Pitt Meadows CS (Station ID: 1106178) were scaled and adjusted to Haney UBC RF Admin monthly and decadal averages and combined with the Haney UBC RF Admin record to create a continuous daily record.	Station data: *Haney UBC RF Admin* 49.2645, -122.5732 *Abbotsford Airport* 49.0253, -122.3600 *Pitt Meadows CS* 49.2083, -122.6900	1962-2021	WY and seasonal	Haney UBC RF Admin: (ECCC, 2023j) Abbotsford Airport: (ECCC, 2023d) (ECCC, 2023h) Pitt Meadows CS: (ECCC, 2023i)

Variable	Description	Data region	Record length (WY)	Time period	Data source
MCC	Mean WY and seasonal cloud cover above the study site were calculated using NCEP-NCAR atmospheric reanalysis data. This dataset considers the entire atmosphere as one layer and reports vertical cloud cover from 0-100% at 1.875°x1.875° resolution.	48.57, 50.47, -121.875, -123.75	1962-2021	WY and seasonal	(NOAA, 2024a)
SWE	Mean WY SWE values were calculated from NCEP-NCAR atmospheric reanalysis data. This source reports daily kg/m^2 of water equivalent of accumulated snow depth at 1.875°x1.875° resolution.	48.57, 50.47, -121.875, -123.75	1962-2021	WY	(NOAA, 2024b)
Climate indices					
SPEI	SPEI is a drought index calculated using precipitation and potential evapotranspiration (Beguería et al., 2010). Mean seasonal and WY SPEI were calculated using gridded data with a 0.5°x0.5° resolution for the grid cell covering the study area.	49, 49.5, -122.25, -122.75	1962-2021	WY and seasonal	(Beguería et al., 2023)
ENSO	ENSO is a three-to-seven-year oscillation with low atmospheric pressures and high sea surface temperatures occurring in the tropical eastern Pacific during the El Niño phase. The Niño 3.4 index was selected for this study as it is commonly used for ENSO analysis in North America and is defined by sea surface temperatures between 5°N-5°S, 170°W-120°W (ESRL/NOAA, 2023).	Global	1962-2021	WY and seasonal	(ESRL/NOAA, 2023)

Variable	Description	Data region	Record length (WY)	Time period	Data source
PDO	The PDO is a 20-to-30-year oscillation defined by Pacific Ocean temperature and sea level pressure. When interior North Pacific sea surface temperatures and sea level pressures are anomalously low, the PDO is in its positive phase (NOAA, 2023).	Global	1962-2021	WY and seasonal	(NOAA, 2023)
AO	The AO is a weeks- to months-long oscillation characterized by atmospheric pressure over the arctic and northern Pacific and Atlantic oceans. When Arctic atmospheric pressure is anomalously low and north Pacific and Atlantic atmospheric pressure is anomalously high, the AO is in its positive phase (Thompson et al., 2003).	Global	1962-2021	WY and seasonal	(National Weather Service Climate Prediction Center, 2023a)
MJO	The MJO is a 30-to-60-day oscillation which creates regions of enhanced and suppressed tropical rainfall. MJO records were determined by 200 hPa velocity potential anomalies within 0-30°N, normalized by standard deviation during ENSO-neutral and weak ENSO winters (National Weather Service Climate Prediction Center, 2023b). Weekly MJO records for the 120°W region (the eastern tropical Pacific) were used.	120°W region	1979-2021	WY and seasonal	(National Weather Service Climate Prediction Center, 2023b)
NPGO	The NPGO is a decadal-scale ocean oscillation defined by sea surface height anomaly in the northeast Pacific (Di Lorenzo et al., 2008).	Global	1962-2021	WY and seasonal	(Di Lorenzo, 2023)

Variable	Description	Data region	Record length (WY)	Time period	Data source
PNA	The PNA teleconnection is a sub-seasonal variation defined by 550 mb height anomalies and affects the Northern Hemisphere extra-tropics. The positive phase of the PNA features above-average heights (above-average temperatures) in the tropical Pacific and western North America (National Weather Service Climate Prediction Center, 2023c).	Global	1962-2021	WY and seasonal	(National Weather Service Climate Prediction Center, 2023c)

2.2.4. Analyzing relationships between radial growth, ARs, and climate variables with GAMs

Generalized Additive Models (GAMs) were created to analyze relationships between radial growth, ARs, and climate variables. GAMs model relationships between the sums of smoothed functions of predictor variables (covariates) and a response variable (Wood, 2017). Unlike Generalized Linear Models, the linear equivalent to GAMs, GAMs model non-linear relationships between predictor and response variables. This makes GAMs a suitable choice for modelling the potentially non-linear relationships between AR variables, climate variables, and climate oscillation indices (the predictor variables) and annual, earlywood, and latewood radial growth (the response variables). This study applied GAMs to 1) assess relationships between individual predictor variables and the radial growth response variables, and 2) determine whether AR data, alongside known predictors of radial growth, improved model fits.

To determine whether inclusion of AR variables improved model fits, single-predictor GAMs were first created between all WY and seasonal AR variables, climate variables, and climate oscillation indices (as predictors) and annual, earlywood, and latewood radial growth (as response variables). GAMs cannot model more response data than the number of predictor variable inputs (Wood, 2017), so to refine the number of predictor variables in the multi-predictor GAMs, only the non-AR variables with the strongest relationships to radial growth were included. Predictor variables were assessed according to their single-predictor GAM's 1) p value, where the p value approximates the likelihood that a model's smooth covariate equals zero, and 2) adjusted R^2, the proportion of variance explained where original variance and residual variance are both approximated using unbiased estimators (Wood, 2017). Non-AR predictors with $p<0.05$ and $R^2 \geq 0.1$ were selected for inclusion in the multi-predictor GAMs. A multi-predictor GAM was created with these variables, then all AR variables were added to this GAM and model fit before and after AR variable inclusion was evaluated, as described below. This allowed for a determination of if and how AR data explained radial growth variability while accounting for the effects of other likely influences on radial growth.

Due to the large number of covariates, a stepwise GAM approach was necessary to prevent the model from having more coefficients than response variable observations.

First, a multi-predictor GAM was created with the maximum number of selected (p<0.05 and R^2 ≥0.1) non-AR predictors. The GAM was implemented with automatic term selection using the double-penalty "shrinkage" applied, wherein covariates with the strongest effect on the response were retained and covariates with weak effects were penalized out of the model. This method was chosen as it performs better than alternative selection methods when Restricted Maximum Likelihood (REML) is used for smoothing parameter estimation (Marra & Wood, 2011), described below. GAM covariates with an estimated degrees of freedom <0.0001 were considered penalized out of the model. Penalized covariates were removed from the model, then the remaining selected non-AR predictor variables were added to the GAM and the process was repeated. After all the selected non-AR predictor variables were evaluated (i.e. retained in or removed from the GAM), the AR predictor variables were added to the GAM. The iterative penalization approach was repeated until all AR predictors had been evaluated in the GAM.

Predictor variables were also assessed for their concurvity at each GAM iteration. Concurvity, a measure of predictor variable redundancy in which one smooth term can be approximated by another smooth term in the GAM, can create unstable smooth parameter estimates (Kovács, 2022). The 'concurvity()' function in the 'mgcv' R package was used to test concurvity of covariates (R Core Team, 2022; Wood, 2004). Concurvity values range from 0 to 1, with 0 indicating zero concurvity and 1 indicating no identifiability between predictor variables (Wood, 2004). When two predictor variables' estimate concurvity exceeded 0.5 and neither was penalized out of the model, the predictor variable with the lower p value in the GAM output was retained in the subsequent iteration and the predictor with the higher p value was removed. "Estimate" concurvity exceeding 0.5 was selected as the cut-off because "estimate" is considered a more reliable concurvity measure than the "worst" or "observed" concurvity measures available in 'mgcv' and because concurvity above 0.5 may introduce substantial risk of a false statistically significant effect (He, 2004; Wood, 2004).

GAMs were implemented with the 'gam' function using the 'mgcv' package in the R environment (R Core Team, 2022; Wood, 2004). For all GAMs, REML was applied as a smoothing parameter as it is less prone to undersmoothing the models than other smoothing parameters (Wood, 2011). K, the basis dimension which sets the upper limits of degrees of freedom for the smooth functions, was set to 4 to avoid overfitting the

model, resulting in a maximum of three degrees of freedom for all smooth functions (Wood, 2023). Models were also evaluated using the 'k.check' function in 'mgcv' to ensure that the k-index was near one, as k-indices below one indicate a missed pattern left in the model's residuals (Wood, 2017).

The quality of the final non-AR GAM and including-AR GAM was assessed according to the models' *p* values, adjusted R^2 values, and Akaike Information Criteria (AIC). AIC evaluates models by taking both their accuracy and parsimony (number of predictor variables) into account, with lower values indicating a more accurate model with fewer parameters (Wagenmakers & Farrell, 2004). This final model comparison allows for a determination of whether and how AR variable inclusion alongside likely determinants of radial growth improved model fit. This process of creating single-predictor GAMs followed by iterative multi-predictor GAMs to assess AR effects on GAM fits was repeated for each of the detrended radial growth response variables (annual growth, earlywood, and latewood).

The GAMs were used to assess a large number of annual and seasonal AR, climate, and climate oscillation variables as potential predictors of radial growth. These analyses were exploratory by design and intended to evaluate many potential sources of radial growth variability. To constrain the risk of type I errors resulting from the large number of predictor variables tested, this study also compared the GAM results with other North American and PNW studies on climate relationships with radial growth. This pairing of the GAM results with available literature clarified how the GAM results were similar or dissimilar to trends identified elsewhere and allowed for a more comprehensive evaluation of potential mechanisms for environmental control on radial growth beyond the GAM.

2.2.5. Analyzing the interactive effects of ARs and summer droughts on tree growth

To evaluate the concurrent effects of AR variability and summer drought on radial growth, radial growth for years with dry summers and high or low ARs the preceding fall and winter (ONDJFM) were compared with *t*-tests. "Dry" summer years were identified as any WY with a negative JAS SPEI, as this indicates low precipitation and/or high evaporative demand conditions (Beguería et al., 2010). ONDJFM was selected for

analysis of AR occurrence following the reasoning that this range could capture AR occurrence affecting snowpack in advance of the onset of dry JAS conditions. Using the SIO-R1 record, high ONDJFM AR years were determined as any years above the 75th percentile for ONDJFM total AR count (>32 ARs/year, 1962-2021) and low AR years were determined as any years below the 25th percentile for total ONDJFM AR count (<20.75 ARs/year, 1962-2021). Annual radial growth for years falling into either category – years with dry summers and high fall/winter total AR count, and years with dry summers and low fall/winter total AR count – were sub-selected from the detrended MKRF-1 annual ring width chronology. Then, a Welch's *t*-test was performed to compare radial growth between the groups.

This process was repeated for intense ONDJFM AR counts. High intense ONDJFM AR counts were determined as any years above the 75th percentile for the variable (>13 intense ARs/year, 1962-2021) and low intense ONDJFM AR count as any years below the 25th percentile for the variable (<7 intense ARs/year, 1962-2021). A Welch's *t*-test was performed to compare radial growth between these groups.

To determine whether a potential mediating effect of ONDJFM ARs on radial growth was due to AR incidence or due to precipitation generally, a third Welch's *t*-test was performed to compare radial growth means between dry summer years with low ONDJFM precipitation (<25th percentile, <1359.9mm, 1962-2021) and dry summer years with high ONDFJM precipitation (>75th percentile, >1786.3mm, 1962-2021).

Welch's *t*-tests were chosen for all three analyses due to the lack of equal variance between groups. For all groups, data distributions were assessed with Shapiro-Wilk normality tests and analyses were performed with the R base package (R Core Team, 2022). These *t*-test results identified whether radial growth significantly differed between dry summer years with high vs. low total AR counts, high vs. low intense AR counts, and high vs. low precipitation in the preceding fall and winter. Low summer precipitation is generally associated with low radial growth in the western US and Canada (St. George, 2014), and these *t*-tests allow for an evaluation of whether ARs mediate or compound the effects of dry summers on radial growth.

2.3. Results

2.3.1. Tree ring data

Sampling at the MKRF-1 site ultimately yielded 30 complete cores from 15 trees. List method and COFECHA cross-dating revealed that two of the sampled trees produced a duplicate ring in the 1997 calendar year; this was measured as a single year's growth, and earlywood and latewood measurements were excluded for these trees' 1997 rings. Raw annual ring width series from MKRF-1 are shown in Figure 2.4. For the years overlapping with the available AR record (1962-2021), annual and earlywood EPS met the 0.85 guideline (annual EPS=0.859, earlywood EPS=0.850), while latewood did not (latewood EPS = 0.567). COFECHA results indicated that, of 50-year series segments, series intercorrelation was highest for 1950-1999 (segment correlation = 0.29) and lowest for 1975-2021 (segment correlation = 0.18). DplR calculations of series intercorrelation showed a mean intercorrelation of 0.28 for the entire record, 1931-2021.

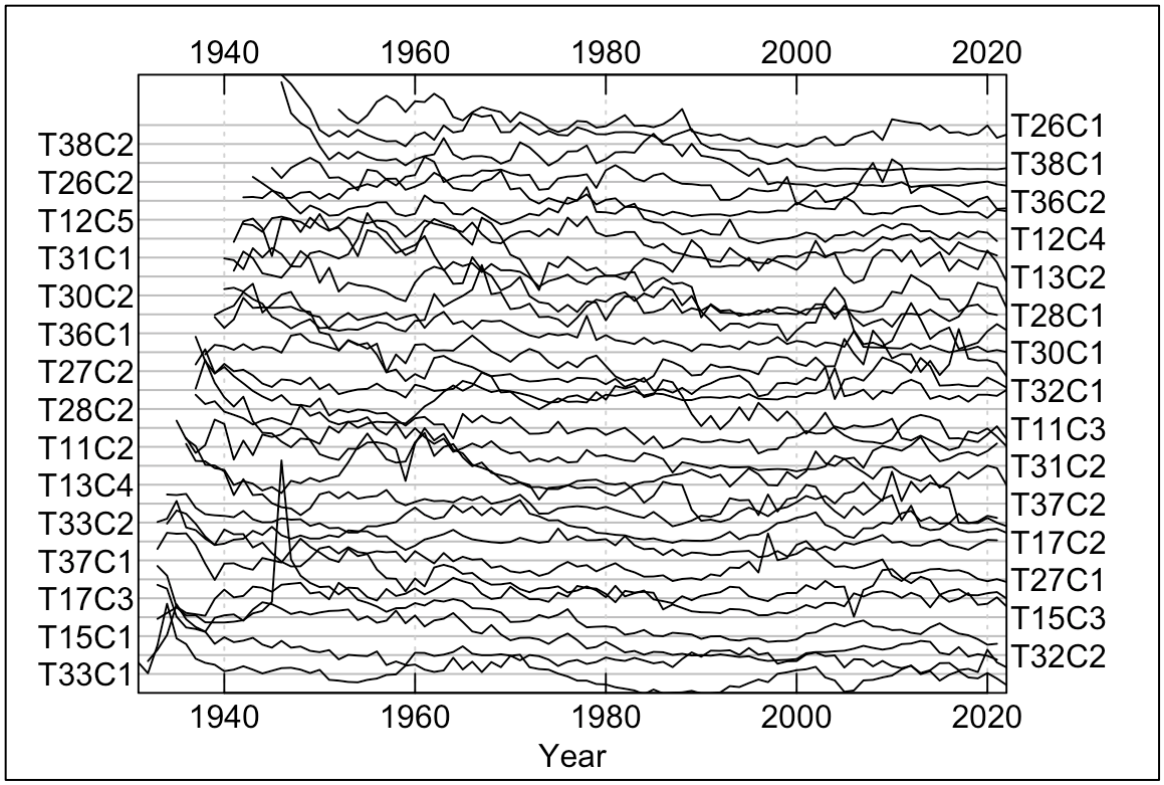

Figure 2.4 Raw annual ring width measurements from the Pacific silver fir cores used to assemble the MKRF-1 radial growth chronologies.

The raw radial growth measurements were detrended on a negative exponential curve to remove age-related growth trends, revealing interannual variation in radial growth across the site. The compiled annual ring width index (RWI) chronology is shown in Figure 2.5 alongside the chronology's sample size.

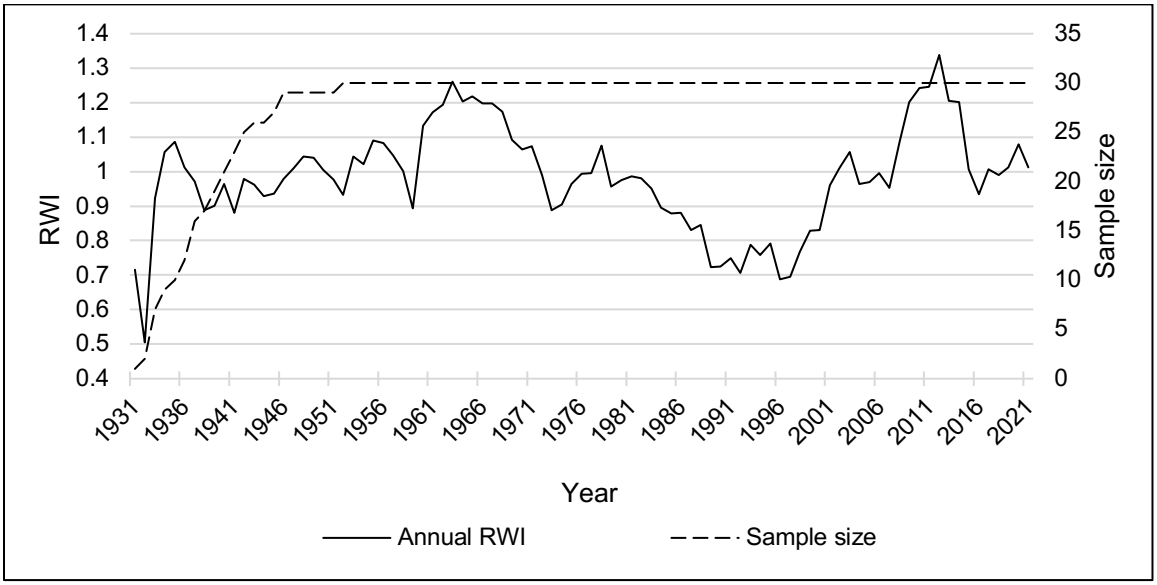

Figure 2.5 The MKRF-1 detrended annual radial growth chronology RWI overlaid with the chronology's sample size.

2.3.2. AR and climate data

Total AR count in the study region ranged from 27 to 65 ARs per WY, while the number of intense ARs per WY ranged from 5 to 25 (Figure 2.6A). The OND season experienced the greatest number of ARs (by both total ARs and intense ARs) as well as the largest mean percentage contribution of AR precipitation to total seasonal precipitation (Figure 2.6B). The JAS season experienced the second-highest total AR count and mean percentage contribution of AR precipitation to total seasonal precipitation, while the AMJ season was the least affected by ARs according to the AR variables measured (Figure 2.6B).

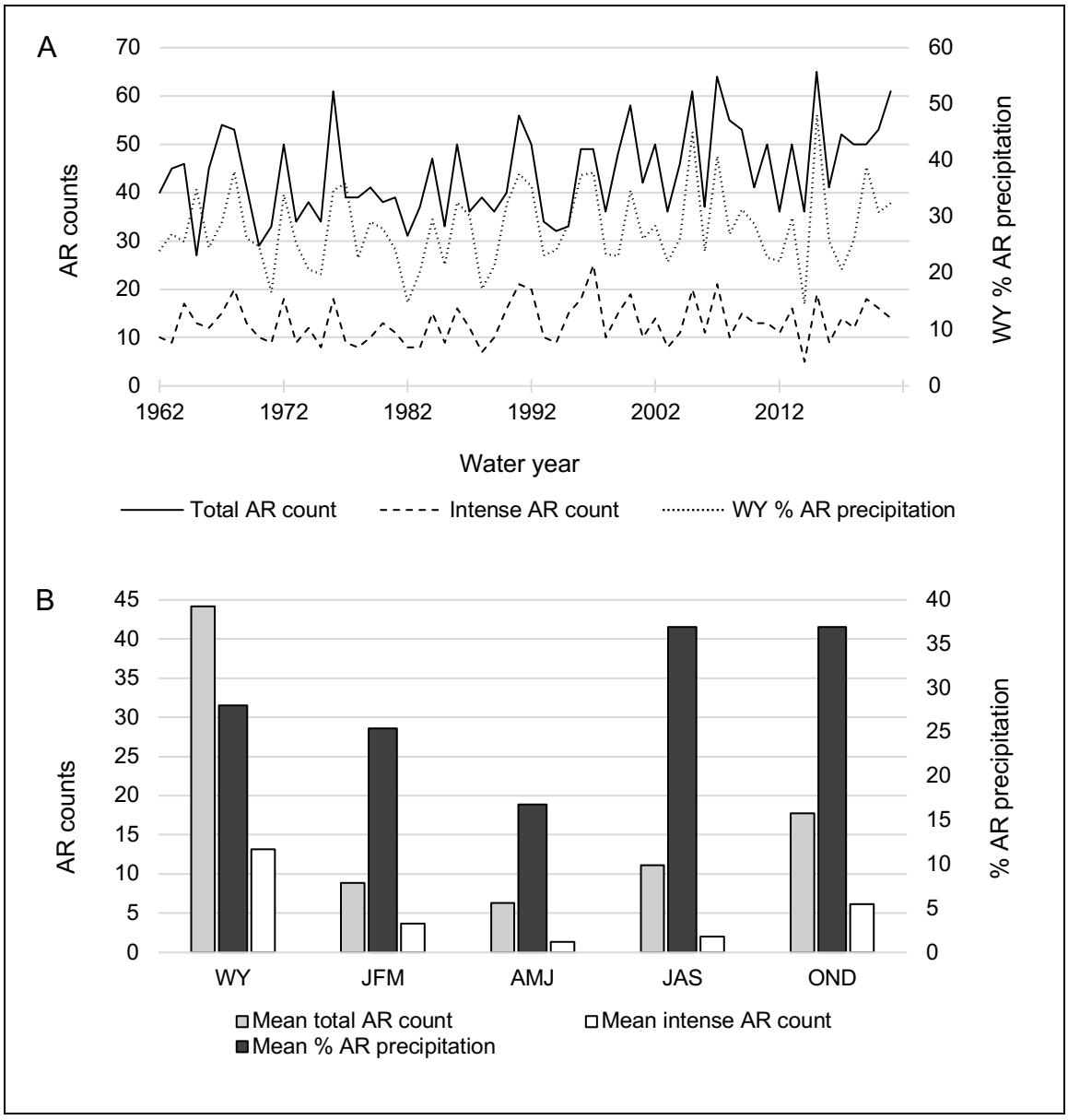

Figure 2.6 (A) Interannual WY AR variability and (B) the mean of AR variables by WY and season, both for 1962-2021.

Calculation of the fraction of ARs in the SIO-R1 catalogue which were PEs (i.e., ARs which approached the study area from the southwest) revealed that 84.2% of ARs were PE ARs.

Post-hoc Pearson correlations were carried out to additionally investigate relationships between variables of interest, with results reported in Table A7.

2.3.3. Radial growth relationships with ARs and climate variables

Annual radial growth relationships with ARs and climate variables

Results from single-predictor GAMs between AR and climate predictor variables and the annual RWI indicated significant (p<0.05 and R^2≥0.10) relationships between the annual radial growth index and mean SWE, AMJ PDO, JAS PDO, WY PDO, JFM MJO, WY MJO, and AMJ Niño 3.4 (Table A2, Figure 2.7).

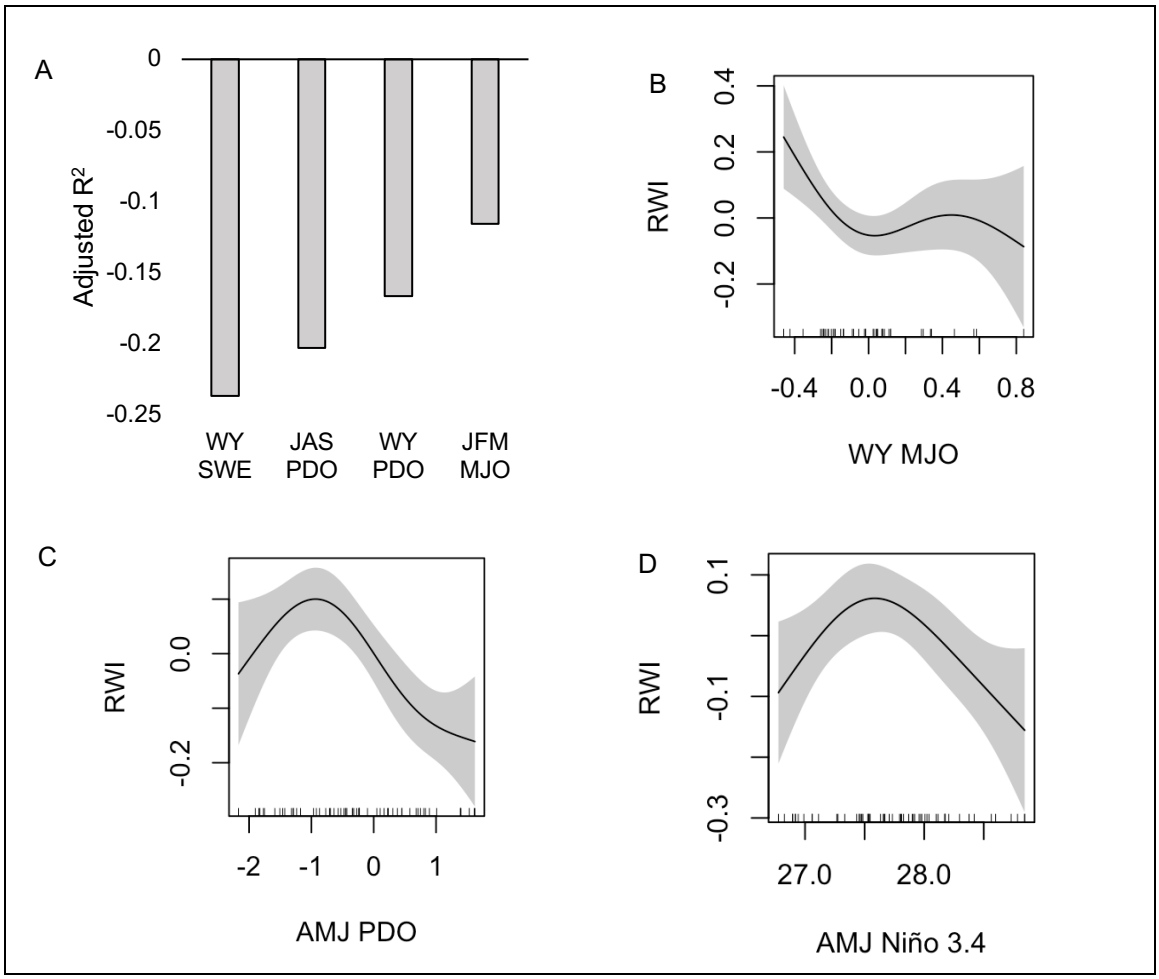

Figure 2.7 **Variables with significant (p<0.05 and R^2≥0.10) relationships with the MKRF-1 annual radial width index (RWI) in single-predictor GAMs. Figure A shows the adjusted R^2 values and direction of the relationship (assessed visually, as adjusted R^2 values do not have a sign) for variables with linear relationships with annual RWI. Figures B, C, and D show the shape of the non-linear significant relationships, with y-axes denoting the smooth function of the predictor variable's effect on RWI (centered to zero) and small vertical lines denoting the distribution of the climate oscillation data.**

GAMs including AR variables showed higher model R^2 than the GAM without, with R^2 increasing by 0.181 between the first and final GAM iteration (Table 2.2). AIC is also lower when AR variables are included in the GAM (AIC=-49.7 at GAM iteration 1, AIC=-65.6 at the final GAM iteration) (Table 2.2).

Table 2.2 Multi-predictor GAM iterations for annual RWI. For non-penalized variable pairs with concurvity greater than 0.5, only the underlined variables were retained in the subsequent iteration.

GAM iteration	Input variables	Adjusted R^2	Deviance explained (%)	AIC	Penalized variables	Non-penalized variable pairs with concurvity above 0.5
1 Significant non-AR variables	Mean SWE AMJ PDO JAS PDO WY PDO JFM MJO WY MJO AMJ Niño 3.4	0.467	53.8	-49.7	JAS PDO	<u>JFM MJO</u> & WY MJO
2 Remove penalized and high-concurvity variables, add AR variables	Mean SWE AMJ PDO WY PDO WY MJO AMJ Niño 3.4 WY total AR count JFM total AR count AMJ total AR count JAS total AR count OND total AR count WY %AR precipitation JFM %AR precipitation JAS %AR precipitation OND %AR precipitation	0.610	69.4	-60.0	WY total AR count JFM total AR count AMJ total AR count OND total AR count AMJ %AR precipitation JAS %AR precipitation OND %AR precipitation	<u>WY %AR precipitation</u> & JFM %AR precipitation

GAM iteration	Input variables	Adjusted R^2	Deviance explained (%)	AIC	Penalized variables	Non-penalized variable pairs with concurvity above 0.5
3 Remove penalized and high-concurvity variables, add AR variables	Mean SWE AMJ PDO WY PDO WY MJO AMJ Niño 3.4 JAS total AR count WY %AR precipitation WY intense AR count AMJ intense AR count JFM intense AR count JAS intense AR count OND intense AR count	0.657	72.7	-65.6	WY % AR precipitation AMJ intense AR count JFM intense AR count JAS intense AR count	OND intense AR count & WY intense AR count
4 Remove penalized and high-concurvity variables to create final GAM	Mean SWE AMJ PDO WY PDO WY MJO AMJ Niño 3.4 JAS total AR count OND intense AR count	0.648	71.4	-65.6	None	None

Variables retained in the final GAM iteration were mean SWE, AMJ PDO, WY PDO, WY MJO, AMJ Niño 3.4, JAS total AR count, and OND intense AR count (Table 2.3). All variables but JAS total AR count and AMJ Niño 3.4 showed $p<0.05$ (Table 2.3).

Table 2.3 Final multi-predictor GAM results for the annual RWI GAM. *P* values <0.05 are shown in bold. EDF indicates the corresponding variable's estimated degrees of freedom in the GAM.

Predictor variable	EDF	*F* statistic	*p* value
JAS total AR count	0.74	0.96	0.06
OND intense AR count	1.60	6.19	**<0.01**
Mean SWE	0.85	1.93	**0.01**
AMJ PDO	0.84	1.82	**0.01**
WY PDO	0.84	1.79	**0.01**

Predictor variable	EDF	*F* statistic	*p* value
WY MJO	2.10	4.56	**<0.01**
AMJ Niño 3.4	0.92	0.51	0.19

Of the variables retained in the final annual RWI GAM, only JAS AR count showed a positive linear relationship with RWI (Figure 2.8). Mean SWE, AMJ PDO, and WY PDO showed negative linear relationships, while OND intense AR count and WY MJO showed non-linear but negatively trending relationships (Figure 2.8). AMJ Niño 3.4 showed a non-linear trend with low RWI at low and high AMJ Niño 3.4 and no partial effect on RWI at neutral AMJ Niño 3.4 (Figure 2.8).

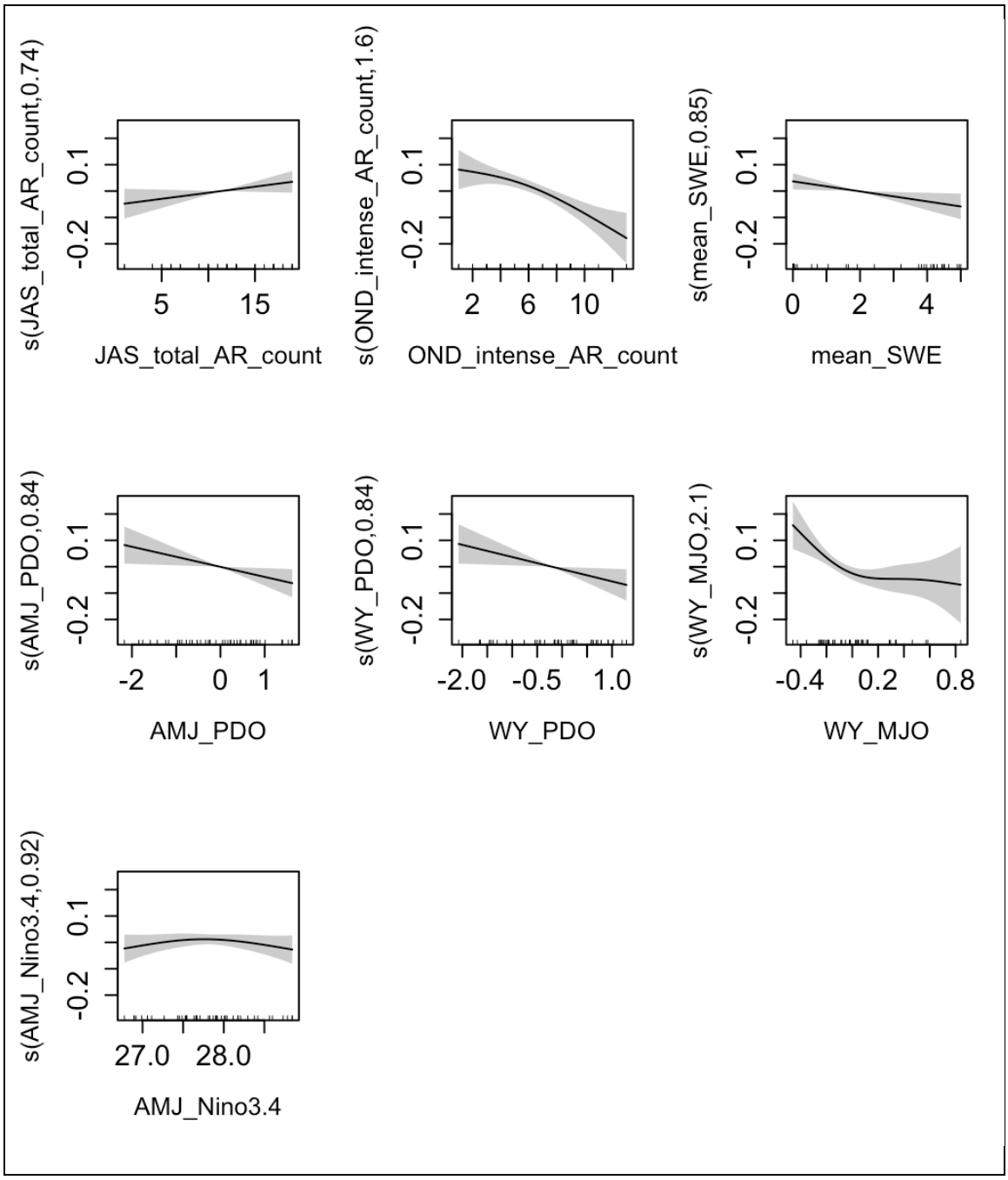

Figure 2.8 **Individual partial effects of the smooth functions of predictor variables on the annual RWI response variable. The predictor variables included are those retained (i.e., not pentalized) in the final multi-predictor GAM. Y-axis values are zero-centered, and the numbers following the y-axis labels are the predictor variables' effective degrees of freedom in the GAM. The shaded area indicates the 95% confidence interval and small vertical lines on the x-axes denote the distribution of AR and climate data.**

Earlywood radial growth relationships with AR and climate variables

Results from single-predictor GAMs between all predictor variables and the earlywood RWI indicate significant (p<0.05 and R^2≥0.10) earlywood RWI relationships with mean SWE, WY PDO, AMJ PDO, JAS PDO, OND PDO, WY MJO, JFM MJO, AMJ PNA, and AMJ Niño 3.4 (Table A3, Figure 2.9).

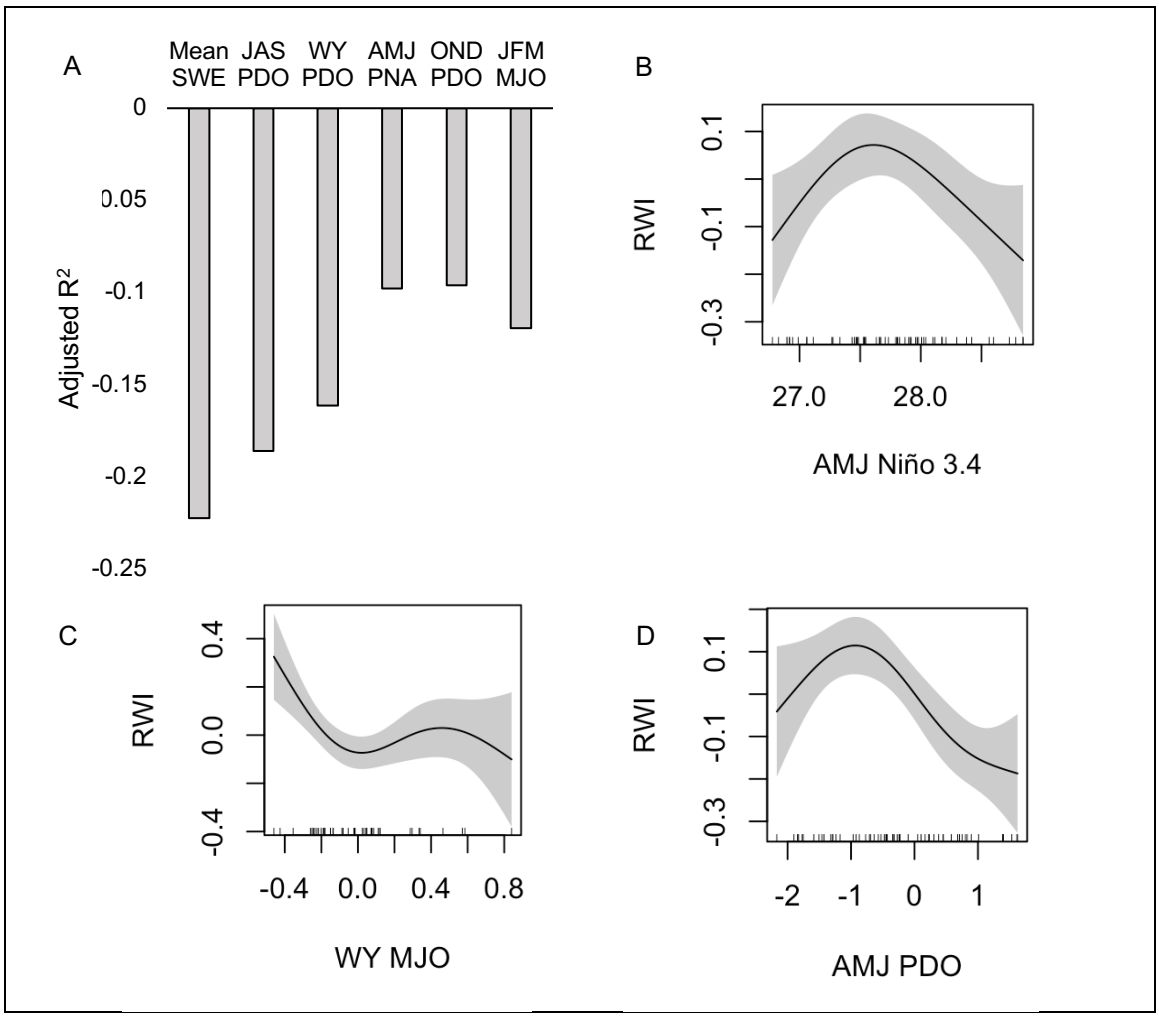

Figure 2.9 **Variables with significant (p<0.05 and R^2≥0.10) relationships with the MKRF-1 earlywood radial width index (RWI) in single-predictor GAMs. Figure A shows the adjusted R^2 values and direction of the relationship (assessed visually, as adjusted R^2 values do not have a sign) for variables with linear relationships with annual RWI. Figures B, C, and D show the shape of the significant variables with non-linear relationships to earlywood RWI, with y-axes denoting the smooth function of the predictor variable's effect on earlywood RWI (centered to zero) and small vertical lines denoting the distribution of the climate oscillation data.**

The final earlywood multi-predictor GAM with AR variables showed a higher model R^2 than the final GAM without AR variables, with R^2 increasing by 0.133 between the first and final GAM iterations (Table 2.4). AIC also decreased between the first and final GAM iterations (Table 2.4).

Table 2.4 Earlywood RWI multi-predictor GAM iterations. For non-penalized variable pairs with concurvity>0.05, only the underlined variables were retained in the subsequent GAM iteration.

GAM iteration	Input variables	Adjusted R^2	Deviance explained (%)	AIC	Penalized variables	Non-penalized variable pairs with concurvity above 0.5
1 Significant non-AR variables	Mean SWE WY PDO AMJ PDO JAS PDO OND PDO WY MJO JFM MJO AMJ PNA AMJ Niño 3.4	0.495	56.6	-39.15	JAS PDO OND PDO AMJ PNA	WY MJO & JFM MJO
2 Remove penalized and high-concurvity non-AR variables and add AR variables	Mean SWE WY PDO AMJ PDO JFM MJO AMJ Niño 3.4 WY total AR count JFM total AR count AMJ total AR count JAS total AR count OND total AR count WY %AR precipitation JFM %AR precipitation AMJ %AR precipitation OND %AR precipitation	0.618	69.6	-50.99	WY total AR count AMJ total AR count OND total AR count JFM %AR precipitation OND %AR precipitation AMJ %AR precipitation	None

GAM iteration	Input variables	Adjusted R^2	Deviance explained (%)	AIC	Penalized variables	Non-penalized variable pairs with concurvity above 0.5
3 Remove penalized variables and add remaining AR variables	Mean SWE WY PDO AMJ PDO JFM MJO AMJ Niño 3.4 JFM total AR count JAS total AR count WY %AR precipitation JAS %AR precipitation WY intense AR count JAS intense AR count AMJ intense AR count JFM intense AR count OND intense AR count	0.70	77.8	-58.424	JAS %AR precipitation JFM intense AR count JAS intense AR count	OND intense AR count & WY intense AR count WY % AR precipitation & WY intense AR count
4 Remove penalized and high-concurvity variables	Mean SWE WY PDO AMJ PDO JFM MJO AMJ Niño 3.4 JFM total AR count JAS total AR count WY %AR precipitation AMJ intense AR count OND intense AR count	0.628	69.2	-53.44	JAS total AR count WY % AR precipitation	None
5 Remove penalized variables to create final GAM	Mean SWE WY PDO AMJ PDO JFM MJO AMJ Niño 3.4 JFM total AR count AMJ intense AR count OND intense AR count	0.628	69.2	-53.44	None	None

Variables retained in the final GAM iteration were JFM total AR count, AMJ intense AR count, OND intense AR count, mean SWE, WY PDO, AMJ PDO, JFM MJO,

and AMJ Niño 3.4. All variables but JFM total AR count and AMJ Niño 3.4 showed $p<0.05$ (Table 2.5).

Table 2.5 Summary results of final multi-predictor GAM annual RW. *P* values less than 0.05 are shown in bold. EDF indicates the variable's estimated degrees of freedom in the GAM.

Response variable	EDF	*F* statistic	*p* value
JFM total AR count	0.549	0.30	0.20
AMJ intense AR count	0.784	1.21	**0.04**
OND intense AR count	1.429	5.30	**<0.01**
Mean SWE	0.819	1.51	**0.02**
WY PDO	0.838	1.73	**0.01**
AMJ PDO	0.846	1.84	**0.01**
JFM MJO	0.927	4.21	**<0.01**
AMJ Niño 3.4	1.184	0.85	0.12

AMJ intense AR count, mean SWE, WY PDO, AMJ PDO, and JFM MJO varied negatively and linearly with earlywood RWI, while OND intense AR count varied non-linearly but predominantly negatively (Figure 2.10). JFM total AR count varied non-linearly but predominantly positively with earlywood RWI, while earlywood RWI was low at low and high AMJ Niño 3.4 and neutral at neutral AMJ Niño 3.4 (Figure 2.10).

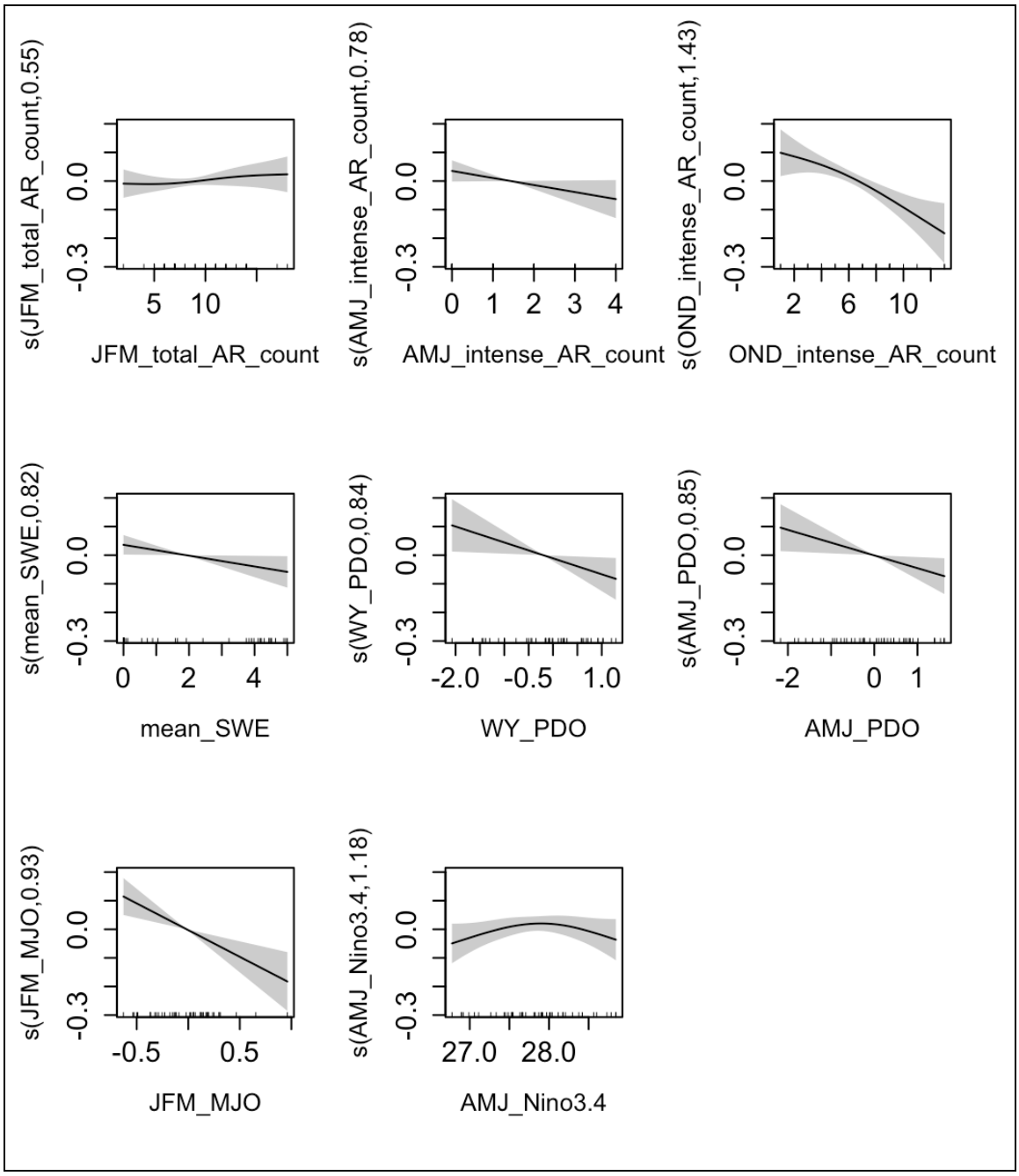

Figure 2.10 **Individual partial effects of the smooth functions of predictor variables on the earlywood RWI response variable. The predictor variables included are those retained (i.e., not penalized) in the final multi-predictor GAM. Y-axis values are zero-centered, and the numbers following the y-axis labels are the predictor variables' effective degrees of freedom in the GAM. The shaded area indicates the 95% confidence interval and small vertical lines on the x-axes denote the distribution of AR and climate data.**

2.3.4. AR and drought effects on radial growth

The *t*-tests revealed no significant differences in RWI between drought summer years with high and low ONDJFM precipitation, drought summer years with high and low ONDJFM total AR counts, or drought summer years with high and low ONDJFM intense AR counts. While annual rings grown during drought summers with low ONDJFM precipitation were smaller (M=0.966, SD=0.173) than annual rings grown during drought summers for years with high ONDJFM precipitation (M=0.927, SD=0.172), the two were not significantly different (*t*[10.9]=-0.161, *p*=0.68). Annual rings grown during drought summer years with low ONDJFM total AR count years were smaller (mean [M]=0.903, standard deviation [SD]=0.096) than annual rings grown during drought summers with high ONDJFM total AR counts (M=1.013, SD=0.188), but the two were also not significantly different (*t*[7.44] = -1.29, *p*=0.240). Oppositely, annual rings grown during drought summers with low intense ONDJFM AR counts were larger (M=1.038, SD=0.122) than annual rings for drought summers with high intense ONDJFM AR counts (M=0.944, SD=0.201). However, these two groups were also not significantly different (*t*[8.37]=0.945, *p*=0.37). RWI distributions for all groups are shown in Figure 2.11.

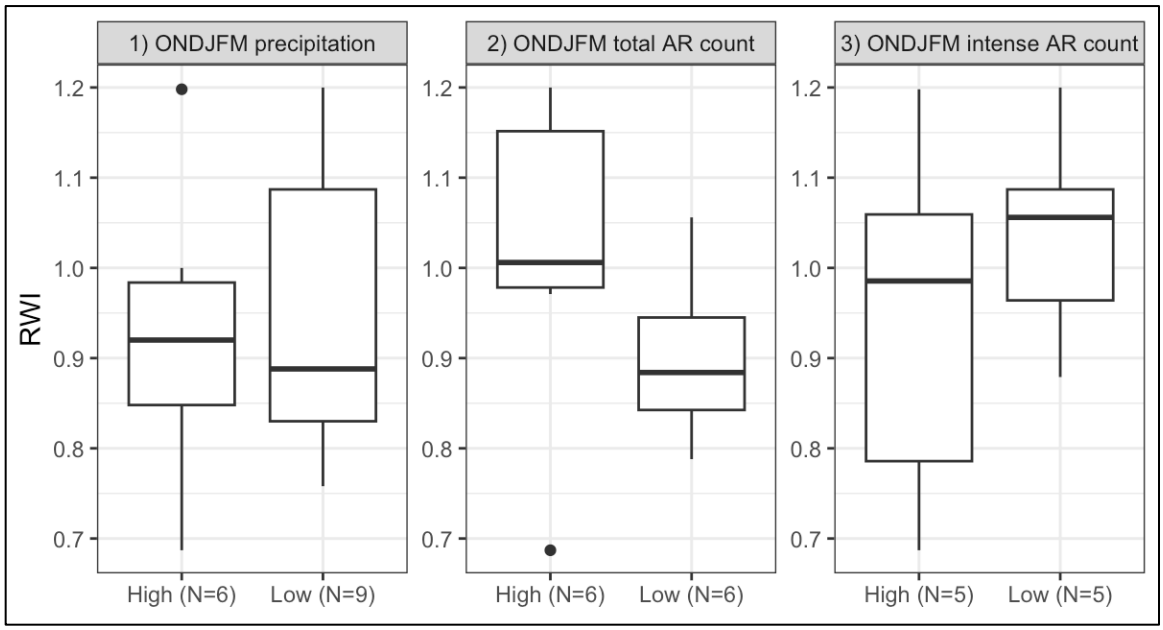

Figure 2.11 RWI distributions for dry summer (JAS SPEI<0) years low (<25th percentile) and high (>75th percentile) in intense ONDJFM AR count, total ONDJFM AR count, and ONDJFM precipitation.

2.4. Discussion

2.4.1. Radial growth as an AR proxy record

This study's results indicate that southwest BC trees can record AR variability in their radial growth. This is the first documented radial growth-AR relationship in southwest BC, to our knowledge. GAM results reveal this finding; AR data improved GAM outputs for the annual RWI and earlywood RWI GAMs, as both showed higher adjusted R^2 and lower AIC with AR variable inclusion. Additionally, some AR variables did not exhibit high concurvity with other non-AR predictor variables (Tables 2.2, 2.4). Together, these results indicate that AR data explain radial growth variability not explained by other climate predictors. Figure 2.12 summarizes the AR variables and other climate variables retained in the final GAM iterations. As the latewood chronology did not meet the EPS≥0.85 threshold, its GAM results are available in Appendix A but excluded here.

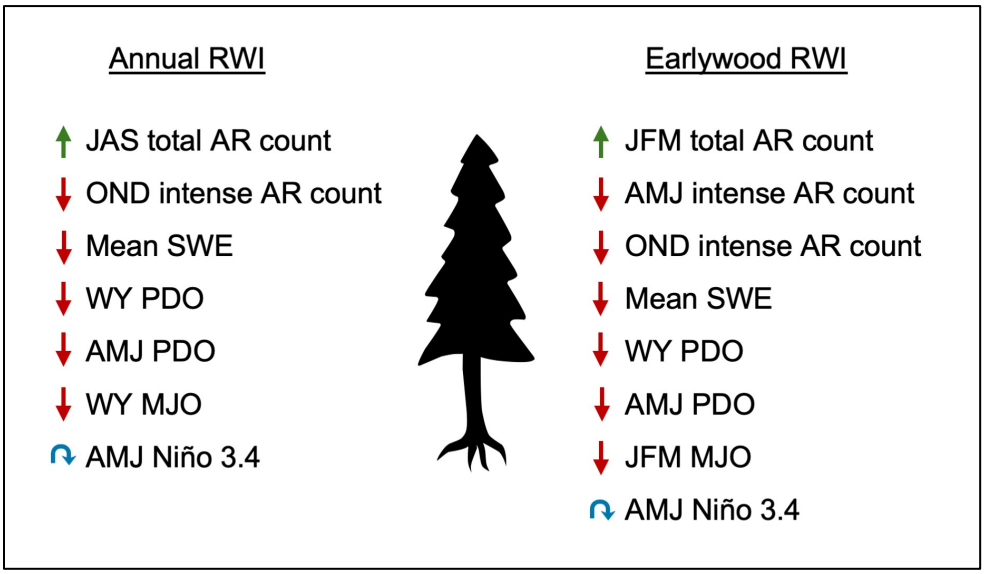

Figure 2.12 **PE and climate variables retained in the final annual and earlywood multi-predictor GAMs. Green upward arrows indicate a positive relationship between the variable and RWI, red downward arrows indicate a negative relationship between the variable and RWI, and blue curved arrows indicate a non-linear relationship between the variable and RWI wherein RWI increases when the variable is low and decreases when the variable is high. Tree image retrieved from Stone (2022).**

The AR variables retained in the final annual and earlywood GAM iterations suggest that ARs may affect radial growth in southwest BC through multiple mechanisms. The GAMs showed a positive relationship between radial growth and total AR counts, including positive associations between JFM total AR count and earlywood RWI (Figure 2.10). This may be a result of ARs contributing to a shrinking of SWE and supporting an earlier onset of the growing season. A post-hoc Pearson correlation test revealed a significant negative correlation between WY AR count and mean SWE (r[58]=-0.27, p=0.03), suggesting that the positive total AR count-earlywood radial growth relationship may result from AR depletion of snowpacks and the resulting early onset and extension of the growing season. Similar negative trends between snowpack and Pacific silver fir radial growth were also observed in Mood & Smith (2021). Although the MKRF-1 area experiences ephemeral snow cover (Leach & Moore, 2014), rather than a seasonal snow cover that persists throughout the winter, the seasonal snowpack conditions at higher elevations may affect the length of the growing season at MKRF-1. Seasonal SWE affects the timing of spring soil warming and the extent of summer soil moisture (Wilson et al., 2020), and these effects may propagate from higher elevations to nearby lower elevations and explain the observed AR-radial growth and SWE-radial growth associations.

The final GAM iteration also showed a positive association between JAS total AR count and annual RWI (Figure 2.8). While this may result from AR contributions to soil moisture during the late growing season, total JAS precipitation was not significant in the single-predictor GAM. This suggests that the positive association between JAS ARs and radial growth may be a result of non-precipitation AR effects, or a combination of AR effects including precipitation. Summer precipitation has been found to both positively and negatively correlate with PNW radial growth (St. George, 2014), aligning with this study's GAM result showing a lack of clear association between JAS precipitation totals and radial growth.

While total AR counts showed positive associations with radial growth in the final GAM iterations, intense AR counts showed negative associations. High radial growth corresponded with low OND intense AR count in both the annual and earlywood final GAMs (Figures 2.8, 2.10), and intense ARs' contributions to snowpacks may explain this effect. Eldardiry et al. (2019) observed greater increases in SWE for more intense ARs (95^{th} percentile of daily precipitation records) than less intense ARs (90^{th} percentile of

daily precipitation records), suggesting that AR intensity increases SWE accumulation. Both the annual and earlywood radial growth records showed negative associations with SWE in their final GAM iterations (Figures 2.8, 2.10), indicating that high SWE is associated with low radial growth at the site. Through this relationship, high OND intense AR counts are likely to result in high snowpacks, which delay the onset of cambial activity and cause the observed low radial growth.

Meanwhile, high AMJ intense AR counts also corresponded with low radial growth in the earlywood GAM (Figure 2.10). Due to their occurrence in warmer months, AMJ ARs are unlikely to interact with snow levels and instead may exert a constraining effect on radial growth through their tendency for rapid runoff. This mechanism was observed in Wise & Dannenberg (2022), who modeled radial growth responses to equal precipitation amounts delivered either steadily through time or delivered through extreme, concentrated precipitation events. This study found that, while steady precipitation delivery conferred a positive effect on radial growth, precipitation delivered over fewer, more intense events resulted in reduced radial growth. Wise and Dannenberg (2022) attributed this trend to extreme precipitation's likelihood to rapidly leave catchments through saturation and infiltration excess overland flow rather than persisting as soil moisture and effectively wetting the root zone. While the % AR precipitation variable more closely aligns with the extreme precipitation modeled in Wise and Dannenberg (2022), and the final earlywood GAM did not retain any % AR precipitation variables, % AR precipitation and intense AR counts were significantly positively correlated in the AMJ season (r[58]=0.86, p<0.01). This indicates that AMJ seasons with high intense AR counts received most of their precipitation through those intense AR events. Intense precipitation events are more likely to exceed the maximum infiltration rates of soils and generate more infiltration excess overland flow relative to less intense precipitation events (Bronstert et al., 2023); in the AR context, intense AMJ ARs, delivering a large fraction of the season's precipitation, contribute little to soil water relative to less-intense precipitation events. This mechanism aligns with this study's findings of a positive total AR count-radial growth relationship and a negative intense AR count-radial growth relationship as well as the results of Wise and Dannenberg (2022).

Comparison of intense and total AR effects on radial growth during dry summer years clarifies this point. Years with dry summers preceded by wet cold-seasons showed higher RWI than years with dry summers preceded by dry cold-seasons, and the same

trend was identified for years with dry summers preceded by high vs. low total AR count cold-seasons (Figure 2.11). Although the differences between these groups were not significant in *t*-tests, the trend suggests that fall and winter AR precipitation, delivered in part through low-intensity events, may have provided a mediating effect on dry summers' constraint on radial growths. However, the opposite trend was observed for intense AR counts. Years with dry summers preceded by high intense AR count cold-seasons had *lower* radial growth than dry summers preceded by low intense AR count cold-seasons (Figure 2.11). This difference also was not significant in a *t*-test, but the divergent trends between intense and total AR counts on dry summer radial growth suggest that intense cold-season ARs affect radial growth uniquely from cold-season ARs in general.

These GAM and *t*-test results indicate that AR associations with radial growth vary based on AR intensity. While southwest BC ARs tend to deplete winter snowpacks, likely exerting a positive effect on radial growth, intense ARs tend toward the opposite. Southwest BC intense AR precipitation is more likely to contribute to snowpacks in cold seasons and rapidly leave catchments as runoff in warm seasons, likely constraining radial growth. These opposite trends provide important insight into the interpretation of radial growth reconstructions of AR variability.

These findings are specific to southwest BC, and previous studies have identified that the strength and direction of AR effects on radial growth vary regionally. For example, while Howard et al. (2023) and Steinschneider et al. (2018) identified strong positive correlations between coastal Californian radial growth records, extreme precipitation occurrences, and AR counts, Steinschneider et al. (2018) found weaker positive correlations with Sierra Nevada records and negative correlations between radial growth and AR counts in western Mexico, southern Arizona, and New Mexico. These results suggest that local-scale hydroclimates and trees' environmental tolerances can cause highly varied effects of ARs on radial growth. In this context, radial growth reconstructions of AR variability should not assume uniform positive associations between AR counts and radial growth. Instead, future reconstructions should both disaggregate AR data by precipitation intensity and evaluate seasonalized AR effects on local-scale hydroclimates to comprehensively understand AR-radial growth relationships.

2.4.2. Additional sources of radial growth variability

In addition to AR variability, the variability of several climate measures, including SWE, appeared to affect radial growth at the study site. Both annual RWI and earlywood RWI showed significant negative relationships with mean SWE (Figures 2.8, 2.10; Table 2.3, 2.5). Of the tested variables which were not AR or climate oscillation variables (i.e., total precipitation, mean temperature, MCC, SWE, and SPEI), SWE was the only variable retained in either the annual or earlywood final GAMs, pointing to this variable's prevailing association with radial growth. The significant (p<0.05) negative relationships observed indicate that high winter snowpacks likely did not benefit tree growth through soil moisture contributions; instead, they appeared to constrain early-season radial growth through the suppression of soil temperatures and a resulting delayed onset of cambial activity. These negative SWE-radial growth trends align with the majority-negative trend for PNW winter precipitation relationships with radial growth identified in St. George (2014).

The PDO also showed significant relationships with radial growth, with WY and AMJ PDO varying negatively with both annual and earlywood RWI in their respective final GAM iterations (Figure 2.8, 2.10; Table 2.3, 2.5). The PDO's climate effects are multivariate; the positive PDO phase is associated with reduced ocean-to-land moisture transport in the PNW, and the PDO exerts its greatest temperature effects in the study area in cold seasons (X. Liu et al., 2016). Resultingly, the PDO has been found to modulate western Canadian snow accumulations and melts on interdecadal time scales (Whitfield et al., 2010). The significant radial growth relationships with PDO phases are likely a result of the PDO's long-term, concurrent controls on precipitation, temperature, and snow levels.

The MJO also showed significant relationships with radial growth records. WY MJO varied negatively with annual RWI in its final GAM iteration (Figure 2.8, Table 2.3), while JFM MJO varied negatively with earlywood RWI in its final GAM iteration (Figure 2.10, Table 2.5). The positive MJO phase is associated with suppressed precipitation (National Weather Service Climate Prediction Center, 2023b), and radial growth likely responded positively to the negative MJO phase's enhanced convection and precipitation. The MJO varies intra-seasonally (30-90 days) (Zhang, 2005), making possible the earlywood RWI's precise response to the JFM MJO phase.

Both the annual and earlywood RWI records showed non-significant, non-linear relationships with AMJ Niño 3.4 in their respective final GAM iterations (Figures 2.9, 2.10; Tables 2.3, 2.5). RWI was suppressed during AMJ La Niña years (i.e., low Niño 3.4) and AMJ El Niño years (i.e., high Niño 3.4), but RWI was enhanced during AMJ ENSO-neutral years (i.e., moderate Niño 3.4) (Figures 2.9, 2.10). The extremes of ENSO likely explain this trend. The El Niño phase of ENSO is associated with warm and dry PNW conditions, while the La Niña phase is associated with cool and wet PNW conditions (Lee et al., 2014). PNW radial growth records have been found to vary positively with growing-season temperature (Larocque & Smith, 2005; Pitman & Smith, 2012), such that cool AMJ temperatures under La Niña are likely to constrain radial growth. Meanwhile, regional radial growth records have also been identified as responding positively to growing-season precipitation (Crawford et al., 2015; St. George, 2014), such that low AMJ precipitation under El Niño is likely to constrain radial growth as well. In this context, both AMJ El Niño and La Niña PNW conditions challenge radial growth, while neutral ENSO's milder conditions avoids these extremes. This likely creates the observed non-linear relationship between Niño 3.4 and radial growth.

Several of the tested climate variables showed no relationships with radial growth. Notably, the radial growth records did not appear to respond to solar radiation variability (Tables A2, A3), despite solar radiation more broadly limiting PNW plant growth than temperature or precipitation (Nemani et al., 2003). The lack of observed response to solar radiation may point to the utilized MCC data inadequately approximating PAR, or it may indeed suggest that the sampled Pacific silver firs were not limited by solar radiation availability. Pacific silver firs are highly tolerant of low light (Klinka et al., 1999), suggesting that the latter is the case. If longer-lived PAR data become available, future analysis using this data could clarify this point.

2.4.3. Southwest BC climate reconstructions

Although this study's results indicate that ARs affect radial growth in a manner not explained by the other tested climate variables, radial growth reconstructions of AR variability in southwest BC remain challenging. Linear regressions are typically applied in tree ring climate reconstructions (Speer, 2010), and a linear Pearson correlation between the strongest AR variable in either chronology's single-predictor GAM (by adjusted R^2 value), AMJ intense AR count, reveals a significant negative correlation

between the variable and earlywood RWI (r[58] = -0.32, p=0.01). However, this correlation is weaker than the Spearman correlations exceeding r=0.5 identified between coastal Californian radial growth records and AR counts identified in Steinschneider et al. (2018), likely due to southwest BC's moisture-rich hydroclimate. In this context, alternative methods of paleoclimate reconstruction, such as tree ring density or $\delta^{18}O$, may be better suited to reconstruct AR variability in this region.

Despite the chronologies' relatively low response to AR variability, this study's findings of divergent total AR and intense AR effects on southwest BC radial growth have important implications for future tree ring AR reconstructions. Disaggregating total AR and intense AR data can clarify AR effects on radial growth, as this study demonstrated. Reconstructions of intense ARs may also be particularly informative in a management context, as AR intensity dictates ARs' disaster risks (Corringham et al., 2019) and impacts on water resources (Chen et al., 2018; Dettinger et al., 2011), including on snowpacks (Eldardiry et al., 2019). Future attempts at PNW historical AR reconstruction should consider this total AR vs. intense AR distinction. As climate change amplifies AR intensity (Payne et al., 2020), a long-term, annually resolved record of past intense AR variability will become increasingly useful to contextualize modern ARs and plan for future hydroclimate extremes.

2.5. Conclusions

This study's GAM results suggest that southwest BC trees can record AR variability in their radial growth, a novel finding for the region. ARs appear to oppositely affect radial growth based on their intensity; high total AR counts were associated with high radial growth, while high intense AR counts were associated with low radial growth. These trends held for both cold-season and warm-season ARs. For fall and winter ARs, interactions between AR intensity and snowpack appeared to drive the observed result, as low SWE was associated with high radial growth in the GAM, and southwest BC ARs generally deplete snowpacks, enhancing radial growth. Intense ARs, however, are more likely to contribute to snowpacks and suppress radial growth, as observed. Meanwhile, for warm-season ARs, interactions between AR intensity and overland flow may drive the observed positive association between intense AR counts and radial growth. The GAM results also suggested PDO, MJO, and ENSO associations with radial growth, and SWE, temperature, and precipitation mechanisms are hypothesized. Comparisons

between this study's results and other North American radial growth AR reconstructions reveals that this study's chronologies more poorly approximate AR variability than radial growth records in the southwest US; in this context, alternative methods of paleohydroclimate reconstruction may be better suited to this moisture-rich region.

Chapter 3. Examining Pineapple Express Storm Variability with Tree Ring Stable Isotopes

3.1. Introduction

Pineapple Express (PE) storms contribute large volumes of water to the North American west coast, with dramatic effects on water resources. PEs, a type of atmospheric river (AR), are synoptic-scale hydrological features that transport water from oceans to mid-latitude coastlines as long, narrow corridors of concentrated water vapor (Ralph et al., 2004; Zhu & Newell, 1998). While ARs are global phenomena (Guan & Waliser, 2015), PE ARs (hereinafter, PEs) are defined by their origin in the sub-tropical Pacific Ocean and filamentary transport of water vapor to the North American west coast (Dettinger, 2004; Roberge et al., 2009). ARs are known for their strong associations with extreme precipitation (Chen et al., 2018; Waliser & Guan, 2017), flooding (Barth et al., 2017; Lavers et al., 2011), and wind hazards (Waliser & Guan, 2017) as well as beneficial contributions to snowpack (Eldardiry et al., 2019; Guan et al., 2013) and drought cessation (Dettinger, 2013). PEs, however, bring hydrological impacts and water management implications distinct from non-PE ARs affecting the North American west coast. Winter PEs affecting western North America contain 2 kg/m^2 more precipitable water and are 1.5°C warmer at landfall compared to non-PE ARs (Gonzales et al., 2022). These warmer temperatures make PEs more likely to precipitate as rain than snow than non-PE ARs (Gonzales et al., 2022), with important hydroclimate impacts. The ratio of rain to snow precipitation (rain fraction) influences the hazard of AR storms, with rainier ARs tied to heightened flood risk due to a more rapid release of runoff (Henn et al., 2020; Ralph et al., 2019). Additionally, warmer ARs (such as PEs) are more likely to deplete snowpacks through rain-on-snow events than cooler ARs (Guan et al., 2016), additionally magnifying flood conditions (Li et al., 2019). The frequency and intensity of PEs, then, have substantial implications on the water resources of the mid-latitude North American west coast.

These implications are particularly consequential in the southwest coast of British Columbia (BC) and the northwest coast of the United States (US) (hereinafter, Pacific Northwest [PNW]). Coastal and near-coastal PNW watersheds experience hybrid runoff regimes, with snowmelt and rainfall both determining moisture availability and the

maintenance of streamflow in the PNW's warm and dry summer months (Pike et al., 2011; Tohver et al., 2014). Many of the region's municipalities rely on cold-season precipitation stored in mountain snowpacks to function as natural reservoirs, the melting of which mediates low summer precipitation and meets water demands (Pike et al., 2011; Vano et al., 2010, 2015). Climate warming-induced increasing rain fraction and decreasing snowpacks (Siirila-Woodburn et al., 2021) pose a challenge to this regime (Hamlet, 2011), making PEs' warm temperatures and resulting interactions with snow levels (Gonzales et al., 2022) increasingly significant.

Given the influence of PEs on water resources and hydroclimates, there is a strong need to understand interannual patterns of PE storms. Contextualizing modern PEs requires long-term historical knowledge of past PE variability; however, such knowledge is generally limited to the mid-20th century satellite era (Shields et al., 2018). Dendrochronological data, alternatively, offer potential proxy records of past weather extremes like PEs that are centuries older than many instrumental records (Speer, 2010). One such dendrochronological record, the oxygen stable isotope ($\delta^{18}O$) composition of tree ring cellulose, has been effectively used to reconstruct paleoclimates due to the climatic controls on the $\delta^{18}O$ of meteoric water. This $\delta^{18}O$ increases with increased air temperatures (Araguás-Araguás et al., 2000), decreases with increased precipitation amounts due to Rayleigh fractionation (Gat, 1996), and varies with factors affected by temperature and precipitation amounts such as condensation height (Buenning et al., 2012), precipitation source area (Gat, 1996), and the distance precipitation travels from its source (Gat, 1996). When water precipitates over land and becomes available to trees through soil water, this water's isotopic signature can be incorporated into a tree's α-cellulose as it grows (McCarroll & Loader, 2004a). Tree ring α-cellulose, then, has the potential to create an annual record of climatic controls on source water $\delta^{18}O$. This source water $\delta^{18}O$ signal may be dampened by additional controls on α-cellulose $\delta^{18}O$ such as growing season relative humidity (Roden et al., 2000), isotope exchange with xylem water (Nakatsuka et al., 2020), and the depth of soil water accessed by trees (Brinkmann et al., 2018). Despite these additional cellulose $\delta^{18}O$ controls, tree ring $\delta^{18}O$ has been used as an effective paleoclimate proxy for precipitation origin. For example, a southeastern US tree ring $\delta^{18}O$ record was found to record North Atlantic hurricane activity (Miller et al., 2006), while another southeastern US tree ring $\delta^{18}O$ record was found to predominantly reflect seasonal moisture source

(Labotka et al., 2016). PEs, however, have not yet been assessed as a potential source of variability in tree ring $\delta^{18}O$ records.

The $\delta^{18}O$ in α-cellulose exhibits potential as a proxy record of PE variability due to a substantial isotopic difference between PE and non-PE storms. Spry et al. (2014) found that PE precipitation affecting southwest BC was 5-6‰ more enriched in $\delta^{18}O$ than non-PE precipitation, and Oster et al. (2012) identified similarly enriched $\delta^{18}O$ in PE precipitation relative to non-PE precipitation affecting central California. Both studies attributed this enriched $\delta^{18}O$ to the warmer temperatures at the PEs' subtropical origins relative to non-PE storms, with warmer temperatures evaporatively enriching sub-tropical seawater relative to the poles (LeGrande & Schmidt, 2006). The enriched $\delta^{18}O$ contained in PE precipitation raises the possibility that trees may record a PE variability signal in the $\delta^{18}O$ of their α-cellulose. While preliminary research on a single PNW tree's α-cellulose $\delta^{18}O$ did not indicate that the tree captured PE variability (Spry, 2013), stable isotopic sampling of four trees is generally required to sufficiently capture variance at a site (Leavitt, 2010). Such a multi-tree analysis of tree ring $\delta^{18}O$ as a potential proxy record for PE variability has not yet been carried out.

A variety of environmental factors have been found to influence the $\delta^{18}O$ stored in trees' α-cellulose each year. These factors, including precipitation amount (Roden & Ehleringer, 2007; C. Xu et al., 2013), relative humidity (Shi et al., 2011), temperature (Labuhn et al., 2014; Rebetez et al., 2003; Saurer et al., 2008; Shi et al., 2011; G. Xu et al., 2014), and snowpack (Qin et al., 2022) are all highly interrelated and cumulatively influenced by climate oscillations (e.g., Wang & Asefa, 2018). Identifying whether trees capture a PE signal in their $\delta^{18}O$, then, requires an analytical accounting for other factors controlling $\delta^{18}O$ variability. To this end, Generalized Additive Models (GAMs) are well-suited to analyze these interrelated influences on $\delta^{18}O$ as GAMs model effect variables as a sum of non-linear functions of multiple predictor variables (Wood, 2017). GAMs allow for an assessment of what combination of predictor variables, such as PE variability, relative humidity, and precipitation, best explain a response variable, such as α-cellulose $\delta^{18}O$. The application of GAMs to dendrohydrological research is a relatively new field with a promising capacity to explore tree ring data variability using interrelated environmental predictors, including PE data.

Managing the PNW's water resources requires a comprehensive understanding of precipitation extremes like PEs. Although this understanding is currently limited to the short length of instrumental records, tree ring $\delta^{18}O$ offers the potential to extend this record and better contextualize the variability of current and future PE storms. This study aims to develop tree ring $\delta^{18}O$ records from four Douglas-fir (*Pseudotsuga menziesii*) trees in southwest BC and (1) test this record's utility as a proxy for PE variability using a GAM approach; (2) evaluate alternative sources of tree ring $\delta^{18}O$ variability including temperature, total precipitation, humidity, and climate oscillations; and (3) contextualize these records with other North American tree ring $\delta^{18}O$ records. Finally, the implications of using tree ring $\delta^{18}O$ in informing water resource management in the PNW are discussed.

3.2. Methods

3.2.1. Study areas

Two sites in southwest BC were identified for tree ring $\delta^{18}O$ study. One site, "Capilano," is located within a forested park in the Capilano Watershed 10 km north of Vancouver, BC. This site was selected for comparison with the $\delta^{18}O$ record created for that site by Spry (2013). A second location, "MKRF-2," is located within the Malcolm Knapp Research Forest (MKRF), 50 km east of the Capilano site. This site was selected for its somewhat drier climate and therefore potential to capture PE variability distinct from the Capilano site. This location is also advantageous because it overlaps with the study area described in Chapter 2 and, as a research forest, the hydrometeorology and human activities in the area have been well described since the mid-20th century (Malcolm Knapp Research Forest, n.d.). Site locations are shown in Figure 3.1.

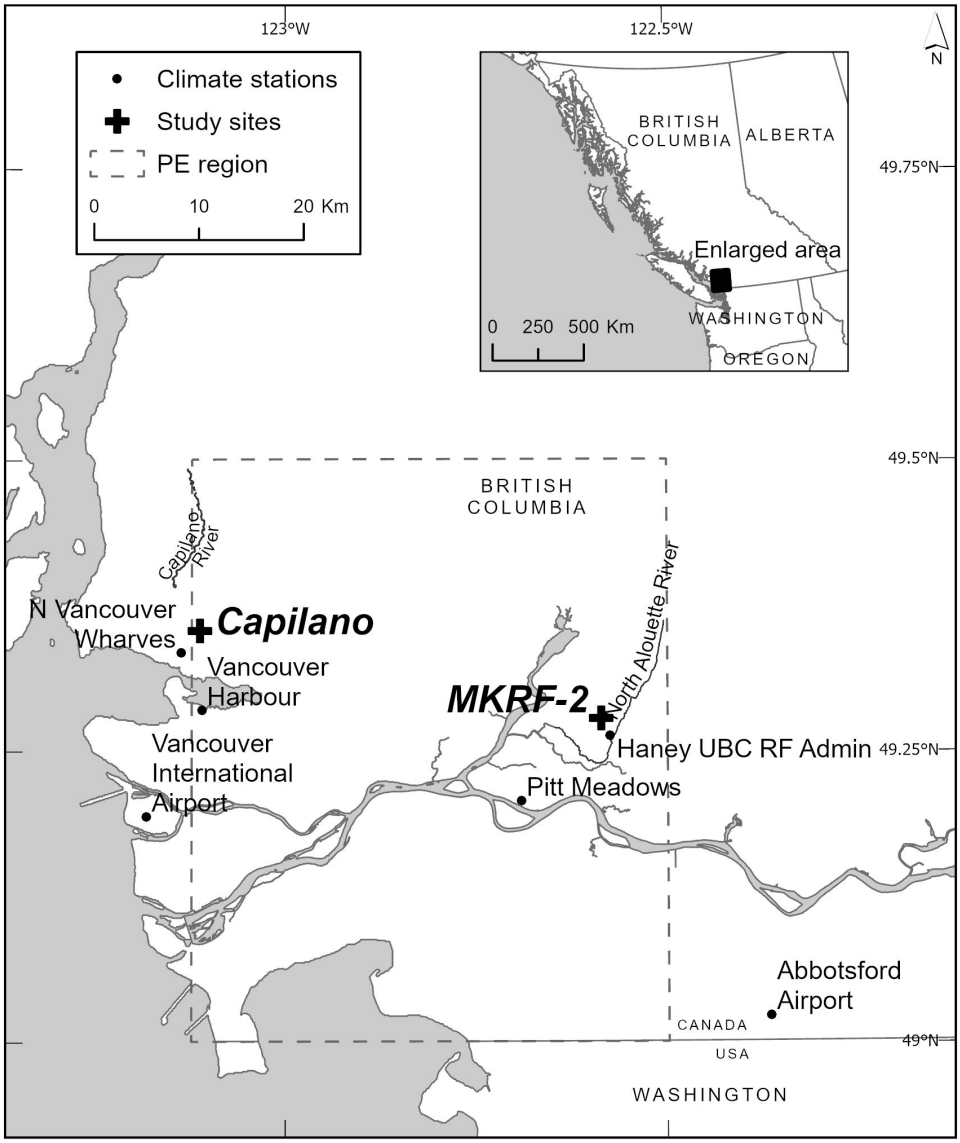

Figure 3.1 Locations of the Capilano and MKRF-2 study sites. The dotted line indicates the extent of the Shields & Kiehl (2016b) grid cell utilized for PE data. Climate stations used to create daily precipitation and temperature records at Capilano and MKRF-2 are shown.

The Capilano study site is located on səlilwətaɬ (Tsleil-Waututh), xʷməθkʷəy̓əm (Musqueam), Sḵwx̱wú7mesh (Squamish), and Stó:lō land (Musqueam Indian Band, 2024; Squamish Nation, 2024; Stó:lō Research and Resource Management Centre, 2016; Tsleil-Waututh Nation, 2021) within the Capilano River Regional Park. The site has an average elevation of 66 m above sea level, a southwest aspect, a 0-5° slope, and falls within the Coastal Western Hemlock dry maritime biogeoclimatic zone (CWHdm) (B.C. Ministry of Forests, 2021). Characteristic of the CHWdm zone, this region

experiences cool summers and mild, wet winters (Meidinger & Pojar, 1991), receiving a mean annual precipitation of 2399 mm and with a mean temperature of 9.1°C (1981-2010 climate normals; [ECCC, 2023a, 2023b]). This climate supports the study site's tree cover of primarily Douglas-fir (*Pseudotsuga menziesii*), western hemlock (*Tsuga heterophylla*), and western redcedar (*Thuja plicata*) and understory of predominantly salal (*Gaultheria shallon*), sword fern (*Polystichum munitum*), and flat moss (*Plagiothecium undulatum*) (Meidinger & Pojar, 1991).

The second study site, "MKRF-2," is located 6.2 km southwest of the "MKRF-1" site described in Chapter 2, both within the North Alouette Watershed on Katzie and Stó:lō land (Katzie First Nation, 2024; Stó:lō Research and Resource Management Centre, 2016). MKRF-2 has an average elevation of 175 m above sea level, a southwest aspect, and a 5-30° slope. It experiences a CWHdm climate with similar tree cover and understory to the Capilano site (B.C. Ministry of Forests, 2021). The area is warmer and drier than the Capilano site, with an average temperature of 9.9°C and annual precipitation of 2180 mm (1981-2010 climate normals; [ECCC, 2023c]). A large fire burned the area in 1868, but, at present, the site is a dense forest of mostly Douglas-fir and western hemlock and is surrounded by active logging and newly planted tree stands (I. Aron, personal communication, October 31, 2022). The exact location of this site was chosen for its accessibility within the MKRF and for its similar elevation to the Capilano site.

Both sites have rainfall-dominated hydroclimates with some winter snowfall (Figure 3.2). Precipitation varies seasonally, with higher precipitation in the fall and winter (ONDJFM) than in the spring and summer (AMJJAS) (Figure 3.2). Both sites are also located within watersheds experiencing high-elevation seasonal winter snowpack, exemplified with data from a nearby climate station in Figure 3.2B.

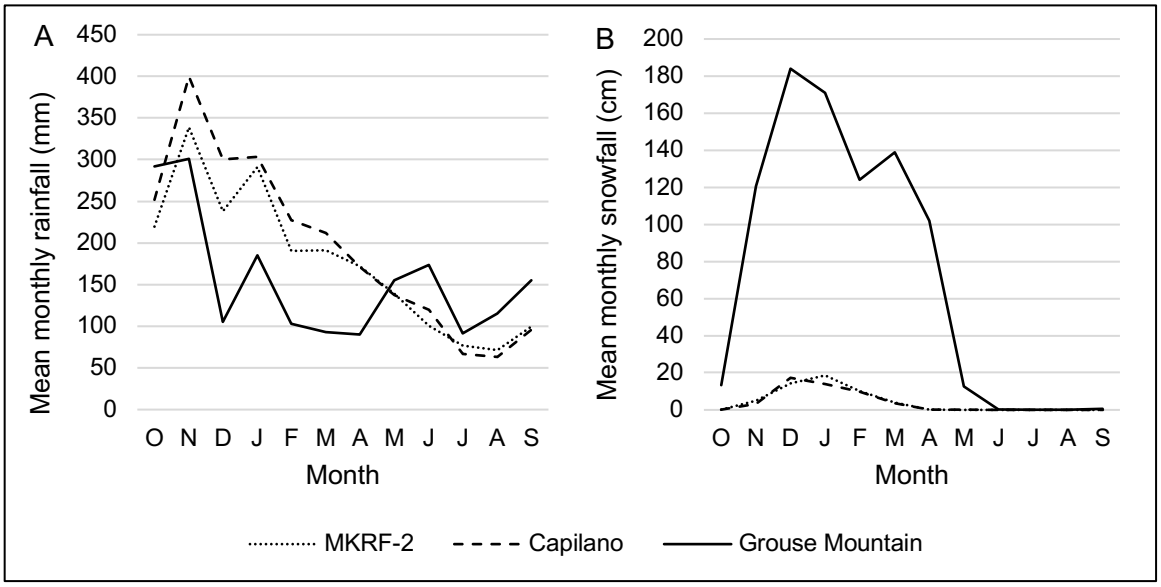

Figure 3.2 **(A) Mean monthly rainfall and (B) snowfall at Capilano, MKRF-2, and the Grouse Mountain climate station (Station ID: 1105658), 1981-2010. For Capilano and MKRF-2, data are sourced from the nearest available climate stations (N Vancouver Cleveland for Capilano, Station ID: 110EF56; Haney UBC RF Admin for MKRF-2, Station ID: 1103332). The Grouse Mountain station approximately 3 km from Capilano, is 45 km from MKRF-2, and is 1103.00 m above sea level. Data sources: Capilano, (ECCC, 2023b); MKRF-2, (ECCC, 2023c); Grouse Mountain, ECCC (2024).**

3.2.2. Sampling and sample preparation

In fall 2022, Douglas-fir trees were cored at Capilano and MKRF-2. Douglas-fir trees were selected for $\delta^{18}O$ study for their distinct definition between light-colored earlywood and dark-colored latewood (Martinez, 1996). Annual $\delta^{18}O$ analysis requires slicing the rings by year, so the high-contrast earlywood and latewood of Douglas-firs makes these trees suitable. Four Douglas-fir trees were cored per site, as this sample size has commonly been identified as sufficient to produce representative site chronologies of tree ring stable isotopes which capture the benchmark 85% of site variance (Leavitt, 2010). To select individual trees for coring, 20 m transects were laid perpendicular to the slopes at each site and all Douglas-firs within 2 m of the transects were numbered. Then, numbers were chosen using a random number generator and the corresponding trees were cored until two complete cores were retrieved per tree from four trees. These cores were later compared to a PE record extending to 1981, so it was

also visually confirmed at the time of sampling that each core was of sufficient age to overlap with the PE record. All cores were sampled using a 5 mm increment borer at 1.35 m above the tree base. Table C1 lists the locations and details of the trees cored at Capilano and MKRF-2.

To prepare the cores for annual $\delta^{18}O$ measurement, the cores were first lightly sanded to enhance earlywood-latewood contrast. Then, the cores were dated and cross-dated with the other trees sampled at the same site using the list method, CooRecorder, and COFECHA as described in Chapter 2 (Cybis Dendrochronology, 2022; Holmes, 1983; Yamaguchi, 1991). To limit time and costs associated with $\delta^{18}O$ analysis, one core from each tree was selected at random for $\delta^{18}O$ analysis, and a sample pooling technique was applied. Pooling, or combining annual rings of identical age from different trees, allows for a higher replication of the isotope chronology without increasing the number of $\delta^{18}O$ analyses and associated cost (Foroozan et al., 2019). The four selected cores were sliced into annual increments, then approximately equal wood masses (±0.02 mg) from each tree for the same year were pooled together as determined by the mass from the tree weighing the least in each year. When slicing the annual rings to produce equal ring masses across years, the rings were sliced parallel to the direction of growth so that proportional volumes of earlywood and latewood were contributed to the pooled sample. This method of pooling by mass was chosen as it avoids producing mass-weighted $\delta^{18}O$ values (Tardif et al., 2008). However, the rings for every 10^{th} year were not pooled and instead were analyzed individually to provide an estimate of the error associated with pooling (Leavitt, 2010). All the pooled and non-pooled samples were then further cut into thin slices and finely ground with an agate mortar and pestle to form homogenous wood samples for each year. This process was carried out for the rings of growth years 1981-2021, as this overlapped with the available PE record.

3.2.3. Extraction of α-cellulose and $\delta^{18}O$ measurement

Tree ring α-cellulose was isolated from the wood using a modified version of the extraction processes described in Leavitt & Danzer (1993) and Loader et al. (1997). The ground wood samples were placed into Soxhlet extraction thimbles; each thimble was placed into a beaker with sodium chlorite, acetic acid, and deionized water; then the beakers were heated in an ultrasonic bath to remove the wood's resins, tannins, and lignin and form holocellulose. The holocellulose samples were then placed in extraction

thimbles within beakers containing a sodium hydroxide solution; this process removes carbohydrates and results in α-cellulose (Loader et al., 1997). Further methodological details are described in Appendix B.

The α-cellulose samples were sent to the Washington State University Stable Isotope Laboratory for $\delta^{18}O$ analysis. $\delta^{18}O$ was measured with a Thermo Finnigan Delta XP isotope ratio mass spectrometer coupled with a Thermo Scientific Temperature Conversion/Elemental Analyzer which pyrolized samples at >1400 ˚C to convert oxygen present in the α-cellulose samples to carbon monoxide. Then, the carbon monoxide gas was passed through the mass spectrometer to determine its oxygen isotopic content (Thermo Fisher Scientific, 2008). Measurements are reported as $\delta^{18}O$ (‰) normalized to Vienna Standard Mean Ocean Water (VSMOW) using two-point normalization of USGS54 and USGS56 after corrections for time and size.

3.2.4. Sourcing PE and climate data

Pineapple Express data

PE data were sourced from the Shields & Kiehl catalogue described in Shields & Kiehl (2016b) and Rutz et al. (2019). This catalogue identifies PEs approaching the North American west coast using satellite-based atmospheric reanalysis from the Modern-Era Retrospective Analysis for Research and Applications Version 2 (MERRA-2) project. From MERRA-2, landfalling PEs are classified as features with contiguous grid cells spanning at least 200 km and a length-to-width ratio of 2:1 in which grid cells meet a latitude-dependent integrated water vapour (IWV) threshold and a regional wind threshold defined by 85th percentile 850 mb wind magnitudes. This catalogue captures PEs by additionally selecting for features approaching the North American west coast from a southwesterly direction, i.e. grid cells with 850 mb wind vectors between 180° and 270°. This dataset identifies PE presence and absence at 3-hourly (8 time steps per day) 0.5° latitude and 0.625° longitude resolution from January 1980 through June 2017 (Rutz et al., 2019; Shields & Kiehl, 2016b) and was selected for this study as it is the most up-to-date reanalysis record of PE storms available.

To determine annual PE counts within the study region, the global three-hourly (eight daily) Shields & Kiehl (2016b) data were first cropped to a spatial extent containing the study sites. Two spatial extents were considered: 1) a larger selection

area (49°, 49.5°, -123.75°, -122.5°) which would capture regional PE variability, and 2) the smallest selection area containing both study sites (49°, 49.5°, -123.125°, -122.5) which would capture more site-specific PE variability. The difference in PE counts per water year[2] (WY) captured by these different areas did not vary substantially (Table 3.1). The smaller selection area was ultimately chosen for this study as AR-derived precipitation in mountainous regions such as the Coast Mountains varies strongly spatially (Sharma & Déry, 2020), making the smaller area's finer resolution preferable.

Table 3.1 Mean PE day count per WY by selection criterion. The underline indicates the combined geographical extent and temporal upscaling method which were chosen for this study.

		Temporal upscaling method	
		≤ 1/8 PE time steps per day = PE day*	≤ 4/8 PE time steps per day = PE day*
Geographical extent	Small region 49°, 49.5°, -123.125°, -122.5	<u>25.4 PEs/year</u>	0.7 PEs/year
	Large region 49°, 49.5°, -123.75°, -122.5°	30.1 PEs/year	0.7 PEs/year

* These upscaling methods refer to the number of three-hourly (eight daily) time steps identified as PE time steps in the Shields & Kiehl (2016b) catalogue for a day to be considered a "PE day" in this study.

The Shields & Kiehl (2016b) 3-hourly data were also upscaled into daily records to allow for the creation of a daily AR count dataset. Two temporal upscaling methods were considered: 1) if at least one 3-hour time step of the eight daily time steps was a PE time step then the day would be considered a PE day (referred to as the 1/8 selection), and 2) if at least four out of the eight daily time steps were PE time steps then the day would be considered a PE day (referred to as the 4/8 selection). Mean WY PE counts were calculated for each of these permutations (Table 3.1). While the 4/8 selection produced an average of 0.7 PEs/year, the 1/8 selection produced an average of 25.4 and 30.1 PEs/year (Table 3.1), making the 1/8 selection closer to the 40 ARs/year rate identified in Waliser & Guan (2017) as common for mid-latitude coastal

[2] North American water years are October 1 to September 30 and are named by the calendar year in which they end.

areas. The 1/8 selection was also determined to be more representative for this study as any PE precipitation might contribute $\delta^{18}O$-enriched precipitation to the region, even if the PE precipitation lasted nine hours (three time steps) or fewer. For these reasons, this study used the 1/8 selection to calculate daily PE records. Once the spatial extent and temporal upscaling method were chosen, PE day counts were summed by WY and season to create WY and seasonal PE count records. Seasons are defined as winter (January, February, March - JFM), spring (April, May, June - AMJ), summer (July, August, September - JAS), and fall (October, November, December - OND). WY (rather than calendar year) analysis was conducted to standardize this study with similar studies.

A second PE variable, the percentage of total WY precipitation occurring on PE days, was included in the analysis as it was reasoned that this variable might better capture the influence of PEs on the soil water $\delta^{18}O$ available to trees. To calculate the percent PE contribution, daily precipitation data measured at the weather stations nearest the sites (N Vancouver Wharves [Climate station ID: 1108447] for Capilano and Haney UBC RF Admin [Climate station ID: 1103332] for MKRF-2) overlapping temporally with the isotope chronology were sourced. Where data were missing from these stations, data were sourced from the next-closest weather stations (Vancouver International Airport [Station ID: 1108447] and Vancouver Harbour [Station ID: 1108446] for Capilano, Abbotsford Airport [Station IDs: 1100030, 1100031] and Pitt Meadows CS [Station ID: 1106178] for MKRF-2) using the “shift factor” approach described in Chapter 2. Once continuous daily precipitation records were established, precipitation occurring on PE days (as defined by the temporally upscaled Shields & Kiehl [2016b] record) was identified and the percentages of total WY precipitation occurring on PE days were calculated for MKRF-2 and Capilano.

A third PE variable, intense PE count, was also assembled. Intense PE days were defined as PE days at or above the 90th percentile of daily precipitation (i.e., days with precipitation totals higher than 90% of the compiled daily Capilano or MKRF-2 precipitation records described above). The 90th percentile and above is commonly used to define intense AR precipitation (e.g., Chen et al., 2018; Hagos et al., 2016; Najibi & Steinschneider, 2023; Ramos et al., 2018), informing its use here.

All PE variables were assembled by WY and seasonally. Although the Shields & Kiehl (2016b) PE record spans January 1980 through June 2017, PE count, percent PE precipitation, and intense PE count data were truncated to WYs 1981-2016 due to the 1980 and 2017 data not including entire WYs.

Climate data

Additional climate data were included in this study's GAM analysis for their potential to explain $\delta^{18}O$ variability. Significant negative correlations have been identified between tree ring $\delta^{18}O$ and precipitation amounts (Saurer et al., 2008; Shi et al., 2011), likely a result of the so-called "amount effect" in which meteoric water $\delta^{18}O$ decreases with increased precipitation amounts due to Rayleigh fractionation (Gat, 1996). Total WY and seasonal precipitation amounts at the study areas were included in the analysis to capture this relationship.

This study also includes growing-season relative humidity (GS-RH) as it has been found to negatively correlate with tree ring $\delta^{18}O$ (Shi et al., 2011), likely a result of isotopic fractionation in tree leaves. Under low-humidity conditions, more light ($\delta^{18}O$-depleted) water molecules preferentially evaporate from leaves, leaving enriched $\delta^{18}O$ in leaf water which enriches $\delta^{18}O$ in α-cellulose (Roden et al., 2000). To account for this relationship, growing-season relative humidity (June through September relative humidity) data were also included in the analysis. Tree ring $\delta^{18}O$ is also known to vary positively with temperature (Labuhn et al., 2014; Rebetez et al., 2003; Saurer et al., 2008; Shi et al., 2011; G. Xu et al., 2014), a result of increasing evaporative enrichment effects on soil water with increasing temperature (Sano et al., 2013), and so was also included in the analysis. Standardised Precipitation-Evapotranspiration Index (SPEI) data were included as well, as SPEI, which combines temperature and precipitation data to represent drought intensity (Beguería et al., 2010), may capture $\delta^{18}O$ variability more strongly than precipitation or temperature alone (G. Xu et al., 2014). SPEI has exhibited negative relationships with α-cellulose $\delta^{18}O$ likely due to the negative relationship between relative humidity and $\delta^{18}O$ (Beguería et al., 2010; Nagavciuc et al., 2022; G. Xu et al., 2014).

Snow water equivalent (SWE) data were also included in the analysis for their potential to represent cold-season precipitation amounts experienced by trees. While cold-season rain is not immediately incorporated into tree growth (as tree growth occurs

in warmer months), cold-season precipitation which falls as snow is stored in the snowpack until warmer months when it melts and becomes available to trees, allowing for its incorporation into cellulose $\delta^{18}O$ (Leonelli et al., 2017). Therefore, a cold-season precipitation amount-$\delta^{18}O$ relationship might be better represented in α-cellulose by SWE than precipitation totals. SWE may also affect tree ring $\delta^{18}O$ through its impacts on growing season length, wherein higher seasonal SWE may delay the onset of the growing season, resulting in less leaf water evaporative enrichment over the growing season and lower α-cellulose $\delta^{18}O$ (Qin et al., 2022). Seasonal snowpacks occur at higher elevations in both the study sites' watersheds (Figure 3.2), and the timing of this snowpack's melt may affect soil temperatures, and thus the length of the growing season (Mellander et al., 2004), at lower elevations such as at Capilano and MKRF-2.

Several climate oscillation indices were also included in the analysis. Climate oscillations influence an array of α-cellulose $\delta^{18}O$ drivers, including storm track (Lin et al., 2020; Zheng et al., 2018), temperature (Becker & Tippett, 2024; Zheng et al., 2018), precipitation amounts (Nalley et al., 2019), SWE (Pathak et al., 2018; Thakur et al., 2020), and RH (Miralles et al., 2014). Therefore, climate oscillation indices, which synthesize these important environmental variables into one index, are well correlated with tree ring $\delta^{18}O$ records from across the globe (e.g., Brienen et al., 2012; Churakova (Sidorova) et al., 2023; Dinis et al., 2019; C. Xu et al., 2019). Several climate oscillations affecting PNW weather, as described below, were included in this analysis for their potential to explain $\delta^{18}O$ variability better than a single climate variable alone.

One oscillation affecting the PNW, El Niño Southern Oscillation (ENSO), creates anomalously warm and dry winters for the PNW in its El Niño phase and anomalously cool and wet PNW winters in its La Niña phase (NOAA PSL, 2023). More ARs occur in the PNW during La Niña and fewer during El Niño (Mundhenk et al., 2016), although this relationship is less pronounced in the PNW than elsewhere on the eastern Pacific coast (Payne & Magnusdottir, 2014). While ENSO was not found to significantly relate to PE variability in southwest BC (Spry et al., 2014), ENSO variability has been shown to correlate significantly with tree ring $\delta^{18}O$ elsewhere (Brienen et al., 2012), indicating its use in this study.

The Pacific Decadal Oscillation (PDO) and North Pacific Gyre Oscillation (NPGO) are also included in the analysis for their potential impact on tree ring $\delta^{18}O$. In

the positive PDO phase, ocean-to-land moisture transport is reduced over the PNW, and in the positive NPGO phase, ocean-to-land moisture transport is enhanced (X. Liu et al., 2016). These oscillations are also associated with variations in Pacific Ocean sea surface temperature (SST) (Di Lorenzo et al., 2008; Mantua & Hare, 2002), driving air temperature variability in the PNW (Mass et al., 2022). Tree ring $\delta^{18}O$ records have been found to record PDO and NPGO variability (Sakashita et al., 2017; C. Xu et al., 2019), supporting their inclusion in this study.

The Arctic Oscillation (AO), Madden-Julian Oscillation (MJO), and Pacific/North American pattern (PNA) are included in the analysis as the three may individually and in combination have impacts on $\delta^{18}O$ variability and AR patterns. Anomalously low Arctic air pressure during the AO's positive phase shifts storms northward of their usual paths, while anomalously high Arctic air pressure during the negative phase shifts storms equatorward (Thompson et al., 2003). In California, more ARs were shown to occur during the negative phase of AO (Guan et al., 2013). The MJO, meanwhile, exhibits an alternating negative phase of enhanced convection and rainfall and positive phase of suppressed convection and rainfall (National Weather Service Climate Prediction Center, 2023b). AR activity has been shown to vary significantly with the location of the MJO convective phase (Guan et al., 2012), including significant negative correlations between the percent contribution of PE storms to annual precipitation and the MJO phase in southwest BC (Spry et al., 2014). The PNA, meanwhile, is determined by differences in air pressure anomalies over the Pacific Ocean and North America. In the PNA positive phase, air pressure anomalies strengthen the mid-latitude jet stream and decrease precipitation in the PNW (Z. Liu et al., 2017). However, more ARs occur in the PNW during the PNA positive phase (Toride & Hakim, 2021). These oscillations and teleconnections also have an interactive relationship with ARs; for example, PNA phase has been found to correlate with the MJO's teleconnection to AR activity (Toride & Hakim, 2021). Tree ring $\delta^{18}O$ has also been found to reflect summer AO variability in northeastern Canada and May AO variability in the Siberian sub-Arctic (Churakova Sidorova et al., 2021; Dinis et al., 2019), but tree ring $\delta^{18}O$ relationships with AO, PNA, or MJO have not been tested for the PNW. This study also analyzed these climate oscillations for their potential to explain PE variability.

Water-year records of temperature, precipitation, SWE, SPEI, ENSO, PDO, NPGO, AO, MJO, and PNA were included in the GAM analysis alongside PE variables.

Records for all variables, except SWE and GS-RH, were also assembled seasonally, with seasons defined as winter (January, February, March - JFM), spring (April, May, June - AMJ), summer (July, August, September - JAS), and fall (October, November, December - OND). GS-RH was assembled for the growing season, June through September, and mean SWE was only assembled by WY. Complete data details, region, and sources are described in Table 3.2.

Table 3.2 AR and climate data sources.

Variable	Description	Data region	Time period	Data source
PE variables				
PE count	Number of PE days, where a PE day is any day with at least one 3-hour time step classified by Shields & Kiehl (2016b) as a PE time step. PE records were available for WYs 1981-2016 at 0.5° latitude and 0.625° longitude resolution.	49, 49.5, -123.125, -122.5	Seasonal and WY	(Shields & Kiehl, 2016b)
Intense PE count	Number of PE days exceeding the 90th percentile for daily precipitation at Capilano or MKRF-2.	49, 49.5, -123.125, -122.5	Seasonal and WY	PE days: (Shields & Kiehl, 2016b) Capilano precipitation: (ECCC, 2023e, 2023g, 2023f) MKRF-2 precipitation: (ECCC, 2023d, 2023h, 2023i, 2023j)
% PE precipitation	The percentage of total WY or seasonal precipitation falling on PE days. Precipitation data sources are described below under "total precipitation."	49, 49.5, -123.125, -122.5	Seasonal and WY	PE days: (Shields & Kiehl, 2016b) Capilano precipitation: (ECCC, 2023e, 2023g, 2023f) MKRF-2 precipitation: (ECCC, 2023d, 2023h, 2023i, 2023j)

Variable	Description	Data region	Time period	Data source
Climate variables				
Total precipitation	Capilano: Daily precipitation totals were sourced from the N Vancouver Wharves weather station records (Station ID: 1105669). Where data were missing from this station, data were inserted from the Vancouver International Airport weather station (Station ID: 1108447) using the shift factor method described in Chapter 2. On days where data from both N Vancouver Wharves and Vancouver International Airport were missing (5 days), shifted data from the nearby Vancouver Harbour station (Station ID: 1108446) were used. MKRF-2: Daily precipitation totals recorded at the Haney UBC RF Admin weather station (Station ID: 1103332). Where data were missing from the Haney UBC RF Admin record, precipitation data from Abbotsford Airport (Station IDs: 1100030, 1100031) and Pitt Meadows CS (Station ID: 1106178) were inserted using the shift factor method. Precipitation records were reported in mm.	Stations: *N Vancouver Wharves* 49.3148, -123.1153 *Vancouver International Airport* 49.1950, -123.1819 *Vancouver Harbour* 49.2944, -123.1114 *Haney UBC RF Admin* 49.2645, -122.5732 *Abbotsford Airport* 49.0253, -122.3600 *Pitt Meadows CS* 49.2083, -122.6900	Seasonal and WY	Capilano: N Vancouver Wharves: (ECCC, 2023e) Vancouver International Airport: (ECCC, 2023g) Vancouver Harbour: (ECCC, 2023f) MKRF-2: Haney UBC RF Admin: (ECCC, 2023j) Abbotsford Airport: (ECCC, 2023d) (ECCC, 2023h) Pitt Meadows CS: (ECCC, 2023i)

Variable	Description	Data region	Time period	Data source
Mean temperature	Mean daily temperature data were sourced from the same stations as the precipitation records. Temperature data were reported in °C.	Stations: *N Vancouver Wharves* 49.3148, -123.1153 *Vancouver International Airport* 49.1950, -123.1819 *Vancouver Harbour* 49.2944, -123.1114 *Haney UBC RF Admin* 49.2645, -122.5732 *Abbotsford Airport* 49.0253, -122.3600 *Pitt Meadows CS* 49.2083, -122.6900	Seasonal and WY	Capilano: N Vancouver Wharves: (ECCC, 2023e) Vancouver International Airport: (ECCC, 2023g) Vancouver Harbour: (ECCC, 2023f) MKRF-2: Haney UBC RF Admin: (ECCC, 2023j) Abbotsford Airport: (ECCC, 2023h, 2023d) Pitt Meadows CS: (ECCC, 2023i)

Variable	Description	Data region	Time period	Data source
GS-RH	Relative humidity is expressed as a percentage of the amount of water vapour in the air compared to how much water vapour could be potentially held by air at the same temperature. RH data were sourced from a 5x5° gridded dataset interpolated using station records. Mean RH was calculated for each WY growing season from 1981-2016.	47.5, 52.5, -122.5, -127.5	Growing season (June-September)	(Willett, 2023)
SWE	Mean WY SWE was calculated as the average of monthly SWE and is reported in metres of water equivalent. (ECCC, 2021) determines SWE using MERRA-2 reanalysis, temperature and snowpack models, satellite records, and climate station data and interpolates these records over a 0.25°x0.25° grid. SWE data were available for calendar years 1981-2016, so water-year records were truncated to 1982-2015.	49, 49.5, -122.5, -123.125	WY	(ECCC, 2021)
Climate indices				
SPEI	SPEI is a drought index calculated using precipitation and potential evapotranspiration (Beguería et al., 2010). Mean seasonal and WY SPEI were calculated using gridded data with 0.5°x0.5° resolution for the adjacent grid cells covering the both study areas.	49, 49.5, -122.25, -123.75	Seasonal and WY	(Beguería et al., 2023)
ENSO	ENSO is a 3-to-7-year oscillation with low atmospheric pressures and high sea surface temperatures occurring in the tropical eastern Pacific during the El Niño phase. The Niño 3.4 index was selected for this study as it is commonly used for ENSO analysis in North America and is defined by sea surface temperatures between 5°N-5°S, 170°W-120°W (ESRL/NOAA, 2023). This record provided monthly Niño 3.4 index data.	Global	Seasonal and WY	(ESRL/NOAA, 2023)

Variable	Description	Data region	Time period	Data source
PDO	The PDO is a 20-to-30-year oscillation defined by Pacific Ocean temperature and sea level pressure. When interior North Pacific sea surface temperatures and sea level pressures are anomalously low, the PDO is in its positive phase (NOAA, 2023). PDO index data were available at monthly resolution.	Global	Seasonal and WY	(NOAA, 2023)
AO	The AO is a weeks- to months-long oscillation characterized by atmospheric pressure over the arctic and northern Pacific and Atlantic oceans. When Arctic atmospheric pressure is anomalously low and north Pacific and Atlantic atmospheric pressure is anomalously high, the AO is in its positive phase (Thompson et al., 2003). AO index data were available at monthly resolution.	Global	Seasonal and WY	(National Weather Service Climate Prediction Center, 2023a)
MJO	The MJO is a 30-to-60-day oscillation which creates regions of enhanced and suppressed tropical rainfall. MJO records were determined by 200 hPa velocity potential anomalies within 0-30°N, normalized by standard deviation during ENSO-neutral and weak ENSO winters (National Weather Service Climate Prediction Center, 2023b). Weekly MJO records for the 120°W region (the eastern tropical Pacific) were used in this study.	120°W region	Seasonal and WY	(National Weather Service Climate Prediction Center, 2023b)
NPGO	The NPGO is a decadal-scale ocean oscillation defined by sea surface height anomaly in the northeast Pacific (Di Lorenzo et al., 2008). NPGO index data were available at monthly resolution.	Global	Seasonal and WY	(Di Lorenzo, 2023)
PNA	The PNA teleconnection is a sub-seasonal variation defined by 550 millibar height anomalies and affects the Northern Hemisphere extratropics. The positive phase of the PNA features above-average heights (above-average temperatures) in the tropical Pacific and western North America (National Weather Service Climate Prediction Center, 2023c). PNA index data were available at monthly resolution.	Global	Seasonal and WY	(National Weather Service Climate Prediction Center, 2023c)

3.2.5. Analysis of PE records and tree ring $\delta^{18}O$ chronologies

Analyzing relationships between $\delta^{18}O$, PE, and climate data

GAMs were used to assess relationships between PE and climate variables and tree-ring $\delta^{18}O$. GAMs examine the associations between the sums of smoothed functions of predictor variables (covariates) and a univariate response variable (Wood, 2017); here, the predictor variables are the annual and seasonal PE, climate, and climate index variables, and the response variable is tree ring $\delta^{18}O$. Linear relationships cannot be assumed between the predictor variables and $\delta^{18}O$, making GAMs a suitable choice as they model both linear and non-linear relationships. Due to the large number of predictor variables, single-predictor GAMs were first created between each predictor variable and the response variables, $\delta^{18}O$ at Capilano and MKRF-2, to determine which predictors demonstrated the strongest individual relationships with $\delta^{18}O$ records. Then, the predictor variables with the strongest individual relationships to $\delta^{18}O$ were included alongside PE data in multi-predictor GAMs to determine whether PE data improved model fit. This process is described in detail below. GAM refinements, including smoothing parameter selection, limitation to the models' degrees of freedom, automatic term selection, and k-index review were identical to those described in Chapter 2.

To assess individual relationships between PE and climate variables and $\delta^{18}O$, single-predictor GAMs were first created. These GAMs were assessed according to their 1) *p* values, where the *p* value approximates the likelihood that a model's smooth covariate equals zero, and 2) adjusted R^2, the proportion of variance explained where original variance and residual variance are both approximated using unbiased estimators (Wood, 2017). Single-predictor GAMs (i.e., GAMs testing one climate predictor variable with the $\delta^{18}O$ response variable) were created for all PE and climate variables (WY and seasonalized). These GAMs modeled the effects of the smooth functions of predictor variables on the response variables (i.e., the smooth function of the predictor variable's association with the response variable). Of these GAMs, covariates exceeding the level of significance ($p<0.05$) were selected for inclusion in multi-predictor GAMs. This method of refining the covariates used in the multi-predictor GAMs was applied due to the number of predictor covariates exceeding the number of $\delta^{18}O$ data points. GAMs require more response data than predictor variables (Wood, 2017), which this method achieved.

To determine whether PE data improved GAM outputs, multi-predictor GAMs were first created with only the selected (p<0.05 in single-predictor GAMs) non-PE covariates. Then, PE variables were added to the GAM and model fits were compared before and after PE variable inclusion. To limit the number of predictor variables, only WY and seasonalized PE count and % PE precipitation (not intense PE count) were analyzed in the multi-predictor GAMs; intense PE count was excluded after noting its lack of significant (p<0.05) relationships with either site's $\delta^{18}O$ by WY or season.

Due to the large number of covariates, multiple iterations of the multi-predictor GAMs were carried out to avoid the model having more predictor variables than response variable observations. At each GAM iteration, double penalty shrinkage automatic term selection was enabled to penalize variables poorly explaining $\delta^{18}O$ from the model. Variables were also assessed for concurvity at each iteration, and for non-penalized variable pairs with estimate concurvity >0.5, the variable with the lower p value was removed from the subsequent GAM iteration (as described in Chapter 2). The quality of the final non-PE and including-PE models were compared using their p values, adjusted R^2 values, and Akaike Information Criterion (AIC). AIC evaluates models by taking both their accuracy and parsimony (number of predictor variables) into account, with lower AIC indicating a more accurate model with fewer parameters (Wagenmakers & Farrell, 2004). The final model comparison allowed for a determination of whether PE variable inclusion alongside likely determinants of tree ring $\delta^{18}O$ improved model output (i.e., whether PE data explained $\delta^{18}O$ variability not explained by other $\delta^{18}O$ predictors).

The GAMs were used to assess a large number of annual and seasonal PE, climate, and climate oscillation variables as potential predictors of $\delta^{18}O$. Considering that little research exists on tree ring $\delta^{18}O$-climate correlations in the PNW, these analyses were exploratory by design and intended to evaluate many potential sources of $\delta^{18}O$ variability. To constrain the risk of type I errors resulting from the large number of predictor variables tested, this study also compared the GAM results with other North American studies on tree ring $\delta^{18}O$-climate relationships. This pairing of the GAM results with available literature clarified how the GAM results were similar or dissimilar to trends identified elsewhere and allowed for a more comprehensive evaluation of potential mechanisms for environmental control on tree ring $\delta^{18}O$ beyond the GAM.

Analyzing site records

Summary statistics were calculated to compare Capilano and MKRF-2 $\delta^{18}O$ records. Standard deviations for each pooled year at Capilano and MKRF-2, alongside the standard deviation for each complete record, were calculated to assess the error associated with pooling.

To evaluate how the MKRF-2 and Capilano $\delta^{18}O$ records compared with each other and within a regional context, Pearson correlation coefficients were calculated between MKRF-2, Capilano, and other tree cellulose $\delta^{18}O$ records from western North America. All annually-resolved, multi-tree cellulose $\delta^{18}O$ chronologies sampled in western North America and available on the International Tree Ring Database (ITRDB) were assessed (NOAA, 2024c). Tree cellulose $\delta^{18}O$ records from this region identified through Web of Science keyword searches which were available at the time of this study were also included in the analysis. Searches including the keywords "tree ring" and "$\delta^{18}O$" followed by political boundaries in western North America (California, Oregon, Washington, British Columbia, Yukon, and Alaska) were performed. Chronology locations and data sources can be found in Table C2.

Hierarchical cluster analyses were also used to assess similarities between the North American records. The records described in Table C2 do not fully temporally overlap with each other or this study's records, and complete data (no missing values) are required for hierarchical cluster calculations. To address this, two subsets of records with data overlapping temporally with the Capilano and MKRF-2 records were analyzed. MKRF-2, Capilano, and records collected to the north of Capilano and MKRF-2 in Alaska (Csank et al. [2016] and Porter et al. [2014]) and the Northwest Territories (Hudson et al. [2015]) were one grouping; MKRF-2, Capilano, and records collected to the south in Washington, Idaho, and Oregon (Schmidt-Simard [2022] for all) were the second group. Each group's records overlapped for thirteen years. Sites identified in the ITRDB and literature search that did not measure or pool more than one tree's $\delta^{18}O$ per site were excluded from the hierarchical cluster analysis. Additionally, one site recorded in Csank et al. (2016), Csank_BR, was excluded from the analysis for its poor temporal overlap with MKRF-2 and Capilano. To carry out the hierarchical cluster analyses, data were scaled across years using the 'scale' function in the R base package (R Core Team, 2022), which subtracts the year's mean $\delta^{18}O$ from each $\delta^{18}O$ observation then divides by

the year's standard deviation. Agglomerative hierarchical clusters with average linkage clustering were then computed for the two groups using the 'hclust' function in the R base package (R Core Team, 2022).

3.3. Results

3.3.1. Annual tree ring isotope records

The cross-dating program COFECHA confirmed successful cross-dating at both sites, with correlations above the significance level (r>0.328) between series segments and the master sequence for Capilano and MKRF-2 (Holmes, 1983). Between 1981 and 2021, $\delta^{18}O$ measured at Capilano ranged from 20.53 ± 0.17‰ to 25.52 ± 0.28‰ with a mean of 23.13 ± 0.15‰ (Figure 3.3A). Mean $\delta^{18}O$ measured at MKRF-2 was higher at 24.02 ± 0.14‰, and its values ranged from 20.87 ± 0.17‰ to 27.63 ± 0.14‰ (Figure 3.3B).

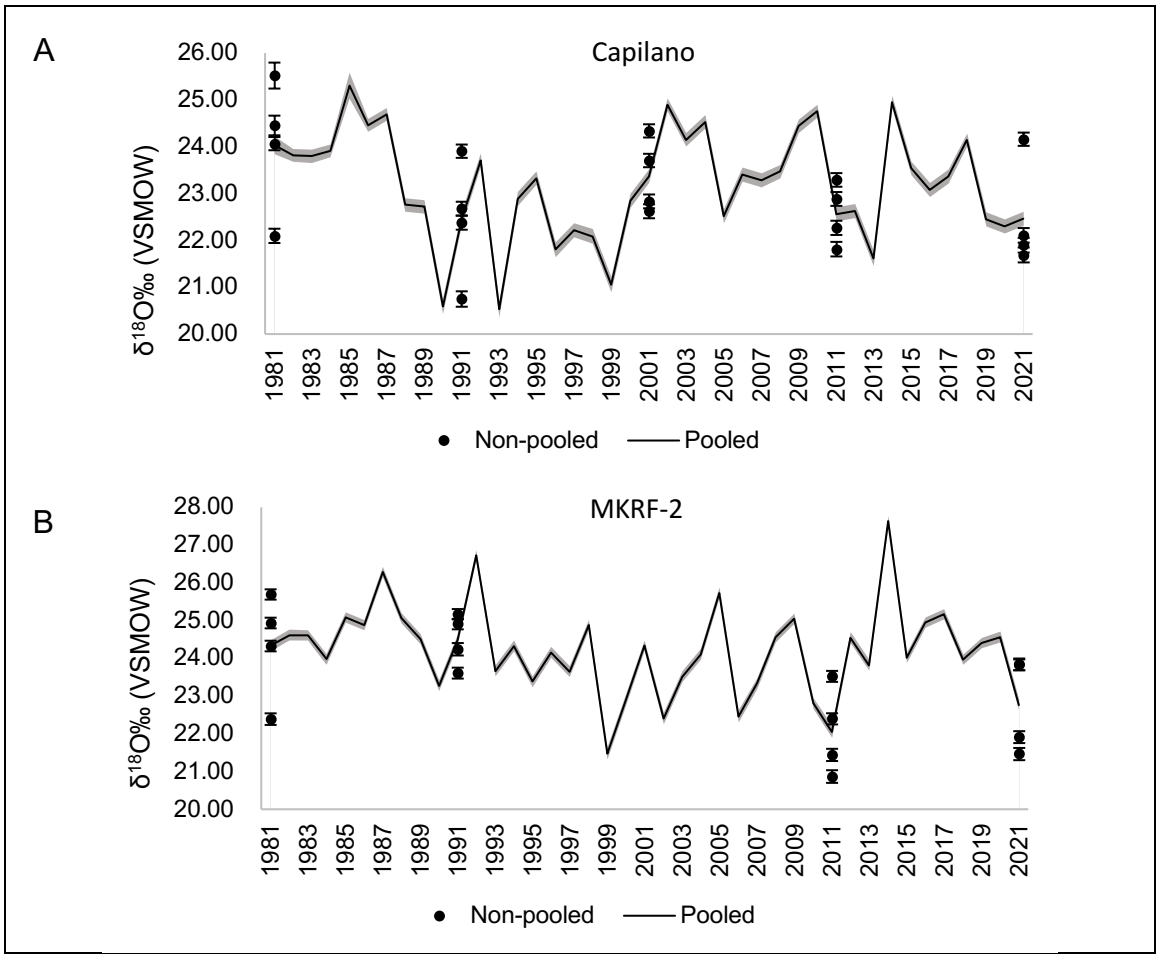

Figure 3.3 Annual tree ring $\delta^{18}O$ measured at (A) Capilano and (B) MKRF-2. The solid line represents the pooled $\delta^{18}O$ record and points represent individual trees' $\delta^{18}O$ for non-pooled years. Where the solid lines coincide with non-pooled years, the solid lines are the average of the individual trees' $\delta^{18}O$ for that year. Error bars and error shading indicate the uncertainty associated with $\delta^{18}O$ measurements.

For Capilano, four of the five non-pooled years are less dispersed (have lower standard deviations) than the entire pooled Capilano record (Figure 3.4A). At MKRF-2, three of the four non-pooled years are less dispersed than the entire pooled MKRF-2 record (Figure 3.4B).

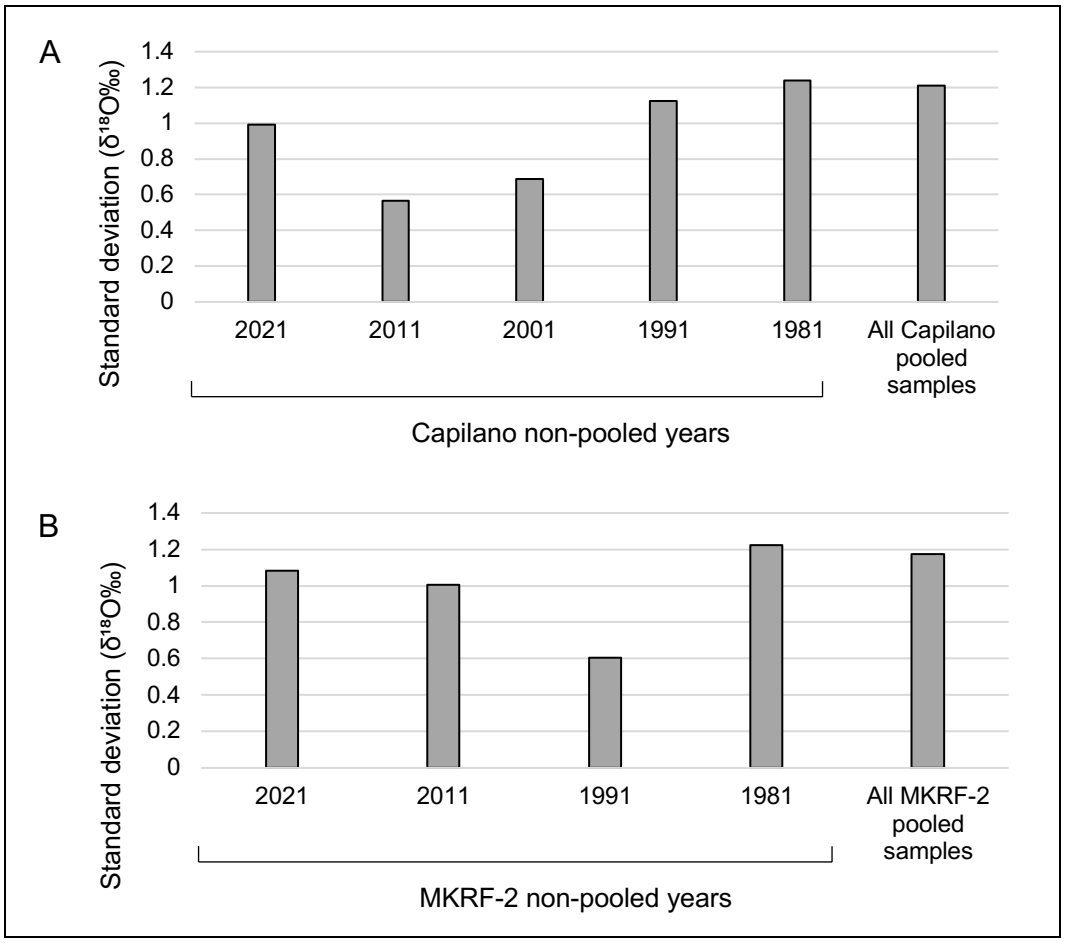

Figure 3.4 **Standard deviations for non-pooled years' $\delta^{18}O$ at (A) Capilano and (B) MKRF-2 alongside the standard deviation for all pooled samples at each site.**

Mean $\delta^{18}O$ of the non-pooled years for each tree is shown in Figure 3.5A for Capilano and Figure 3.5B for MKRF-2.

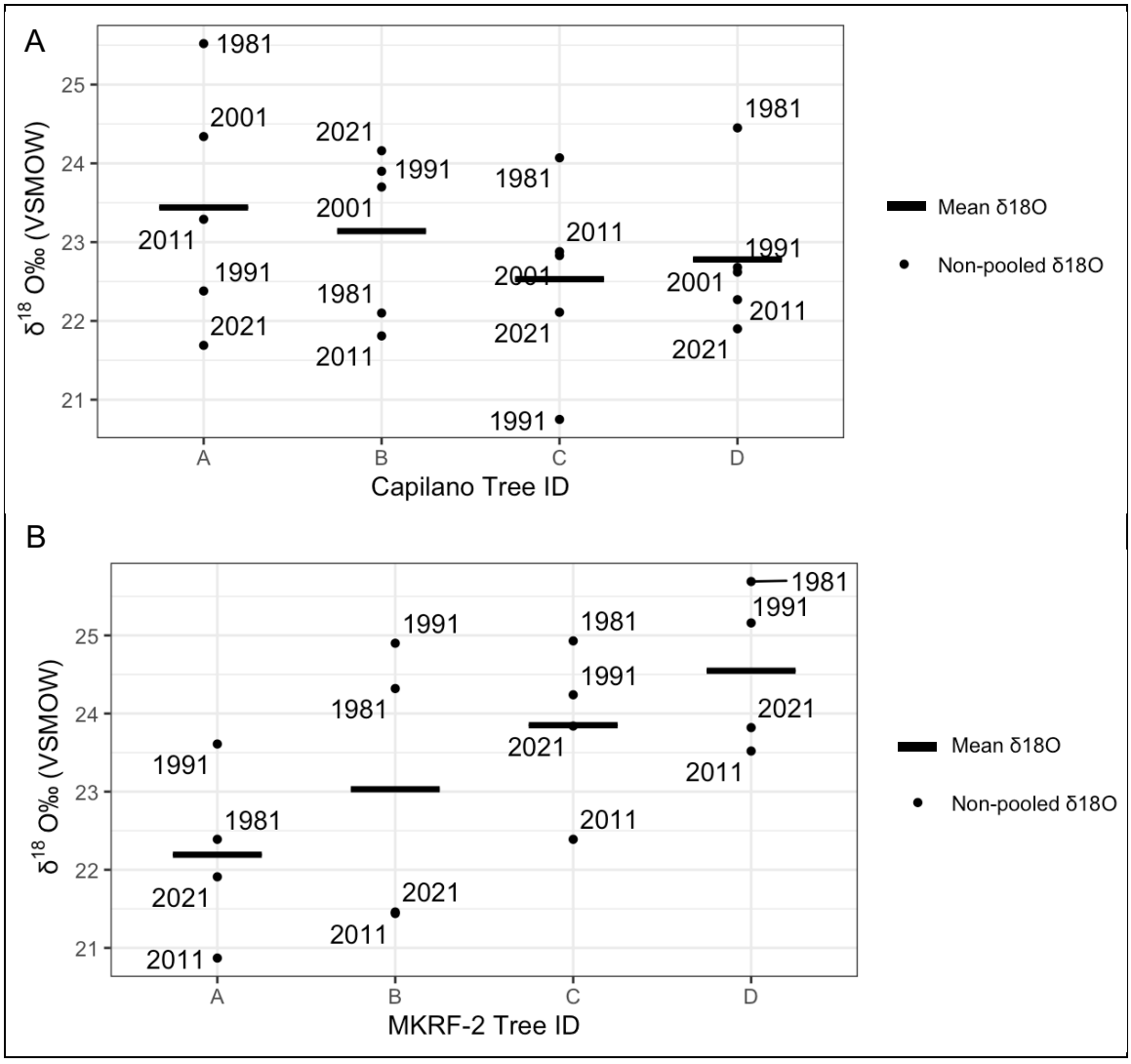

Figure 3.5 Non-pooled $\delta^{18}O$ raw values and means for each tree at (A) Capilano and (B) MKRF-2. Labels indicate the growth years for the non-pooled samples.

3.3.2. PE records

WY PE count in the study area ranged from 11 to 39 with a mean of 25 (Figure 3.6A). PEs were most frequent in the OND season; however, they made up the largest fraction of total precipitation in the JFM season (Figure 3.6B). Annually, MKRF-2 received a larger percentage of its precipitation from PEs than Capilano (Figure 3.6B).

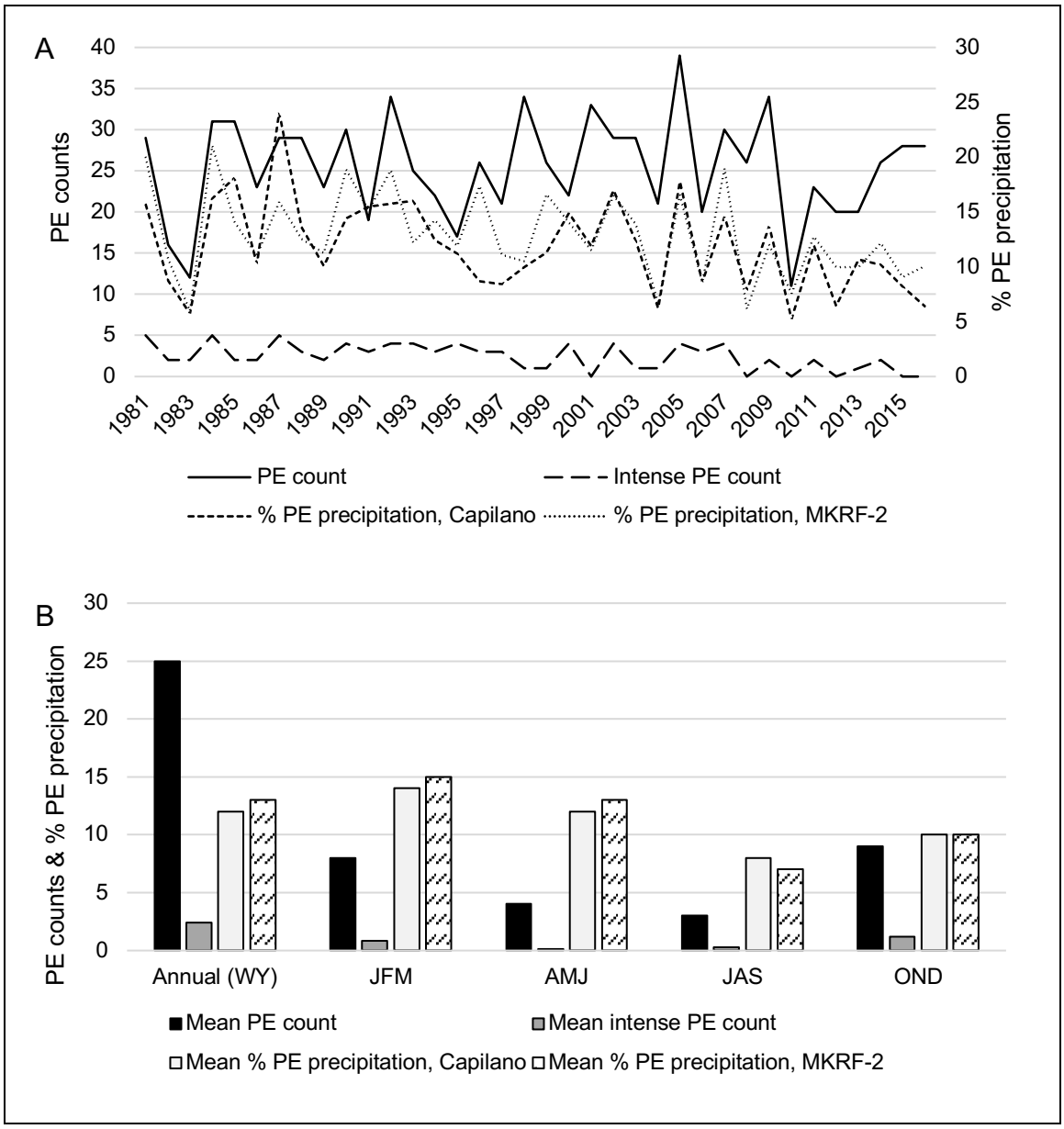

Figure 3.6 (A) WY PE count and % PE precipitation at Capilano and MKRF-2 and (B) mean PE count and % PE precipitation by WY and season for the sites, both for 1981-2021.

3.3.3. Relationships between $\delta^{18}O$, PE, and climate data

Capilano results

Results from single-predictor GAMs between PE predictor variables (PE count and % PE precipitation) and the Capilano $\delta^{18}O$ response variable indicate no significant (p<0.05) relationships between the two (Table C3). Significant p values were found for AMJ AO, OND temperature, WY SPEI, and GS-RH (Table C3, Figure 3.7).

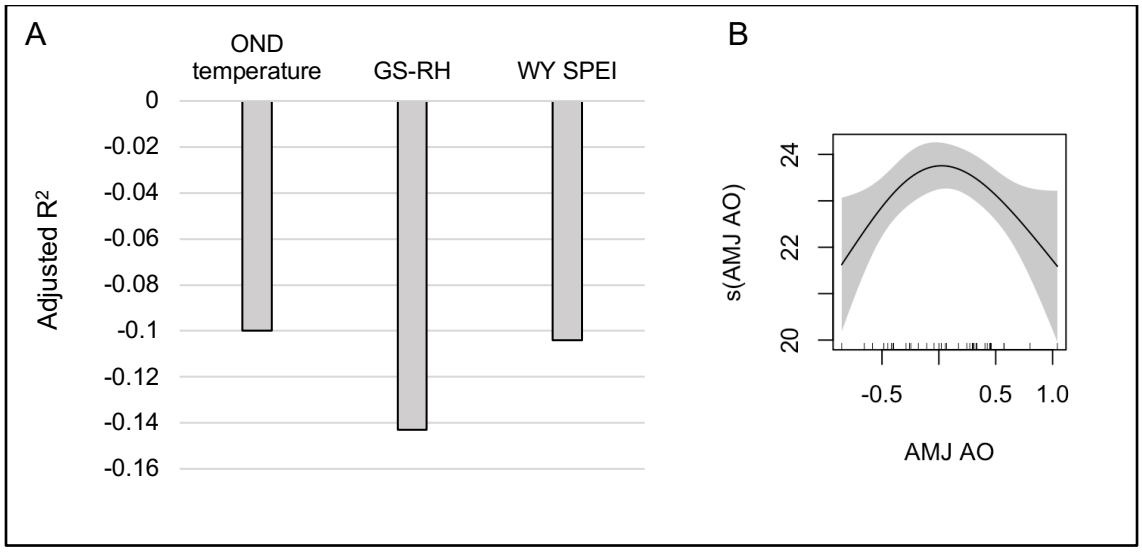

Figure 3.7 Climate variables with significant (p <0.05) relationships with $\delta^{18}O$ in Capilano single-predictor GAMs. (A) the adjusted R^2 values and direction of relationship (assessed visually, as adjusted R^2 values do not have a sign) for predictor variables with linear relationships to the response variable. (B) the relationship between the only non-linear significant (p<0.05) variable and the response variable. Note that y-axis in B indicates the smooth effect of AMJ AO on $\delta^{18}O$, with small vertical lines denoting the distribution of AMJ AO data.

Multi-predictor GAM results for Capilano show an increased model R^2 when PE variables are included. While the selected (p<0.05) non-PE variables return a GAM with an R^2 of 0.45 (GAM iteration 1), the final iteration which includes PE variables returns a GAM with an R^2 of 0.561 (GAM iteration 4) (Table 3.4). AIC is also lower when PE variables are included in the GAM (AIC=102 at GAM iteration 1, AIC=97.5 at the final GAM iteration) (Table 3.3).

Table 3.3 Capilano multi-predictor GAM iterations.

GAM iteration	Variables	R^2 (adjusted)	Deviance explained (%)	AIC	Penalized variables	Non-penalized variables with concurvity above 0.5
1 Significant non-PE variables	AMJ AO WY SPEI Mean OND temperature GS-RH	0.453	51.3	101.6	None	None

GAM iteration	Variables	R^2 (adjusted)	Deviance explained (%)	AIC	Penalized variables	Non-penalized variables with concurvity above 0.5
2 Add PE variables	AMJ AO WY SPEI Mean OND temperature GS-RH OND PE count JFM PE count AMJ PE count JAS PE count WY PE count WY % PE precipitation JAS % PE precipitation	0.556	64.2	97.8	OND PE count JFM PE count AMJ PE count JAS PE count WY PE count	None
3 Remove penalized variables and add remaining PE variables	AMJ AO WY SPEI Mean OND temperature GS-RH WY % PE precipitation JAS % PE precipitation OND % PE precipitation JFM % PE precipitation AMJ % PE precipitation	0.561	64.8	97.5	JFM % PE count OND % PE count	None

GAM iteration	Variables	R^2 (adjusted)	Deviance explained (%)	AIC	Penalized variables	Non-penalized variables with concurvity above 0.5
4 Remove penalized variables to create final GAM	AMJ AO WY SPEI Mean OND temperature GS-RH WY % PE precipitation JAS % PE precipitation AMJ % PE precipitation	0.561	64.8	97.5	None	None

Variables retained in the final GAM iteration were AMJ AO, WY SPEI, OND temperature, GS-RH, WY % PE precipitation, JAS % PE precipitation, and AMJ % PE precipitation (Table 3.3). AMJ AO, WY SPEI, OND temperature, and WY % PE precipitation had significant *p* values (Table 3.4).

Table 3.4 Summary results of final multi-predictor GAM for Capilano. *P* values <0.05 are shown in bold. EDF indicates the variable's estimated degrees of freedom in the GAM.

Response variable	EDF	*F* statistic	*p* value
AMJ AO	1.79	3.98	**<0.01**
WY SPEI	0.91	3.22	**<0.01**
Mean OND temperature	0.87	2.18	**0.01**
GS-RH	0.22	0.10	0.25
WY % PE precipitation	1.61	1.85	**0.04**
JAS % PE precipitation	1.41	1.39	0.06
AMJ % PE precipitation	0.13	0.05	0.27

WY SPEI and OND temperature exhibit the strongest negative relationships with $\delta^{18}O$ (i.e., wetter conditions and higher temperatures result in lower values of $\delta^{18}O$). AMJ % PE precipitation and GS-RH also vary negatively with $\delta^{18}O$, although to a lesser extent than WY SPEI or OND temperature. The percentage of PE precipitation by WY has a non-linear relationship with $\delta^{18}O$, with decreasing $\delta^{18}O$ at lower percentages and

increasing $\delta^{18}O$ at higher percentages. JAS percentage of PE precipitation also has a non-linear relationship with $\delta^{18}O$; $\delta^{18}O$ increases at low percentages and decreases at high percentages. AMJ AO also has a non-linear relationship, with low $\delta^{18}O$ at strong negative and positive AO phases and no effect on $\delta^{18}O$ at the neutral AO phase (Figure 3.8).

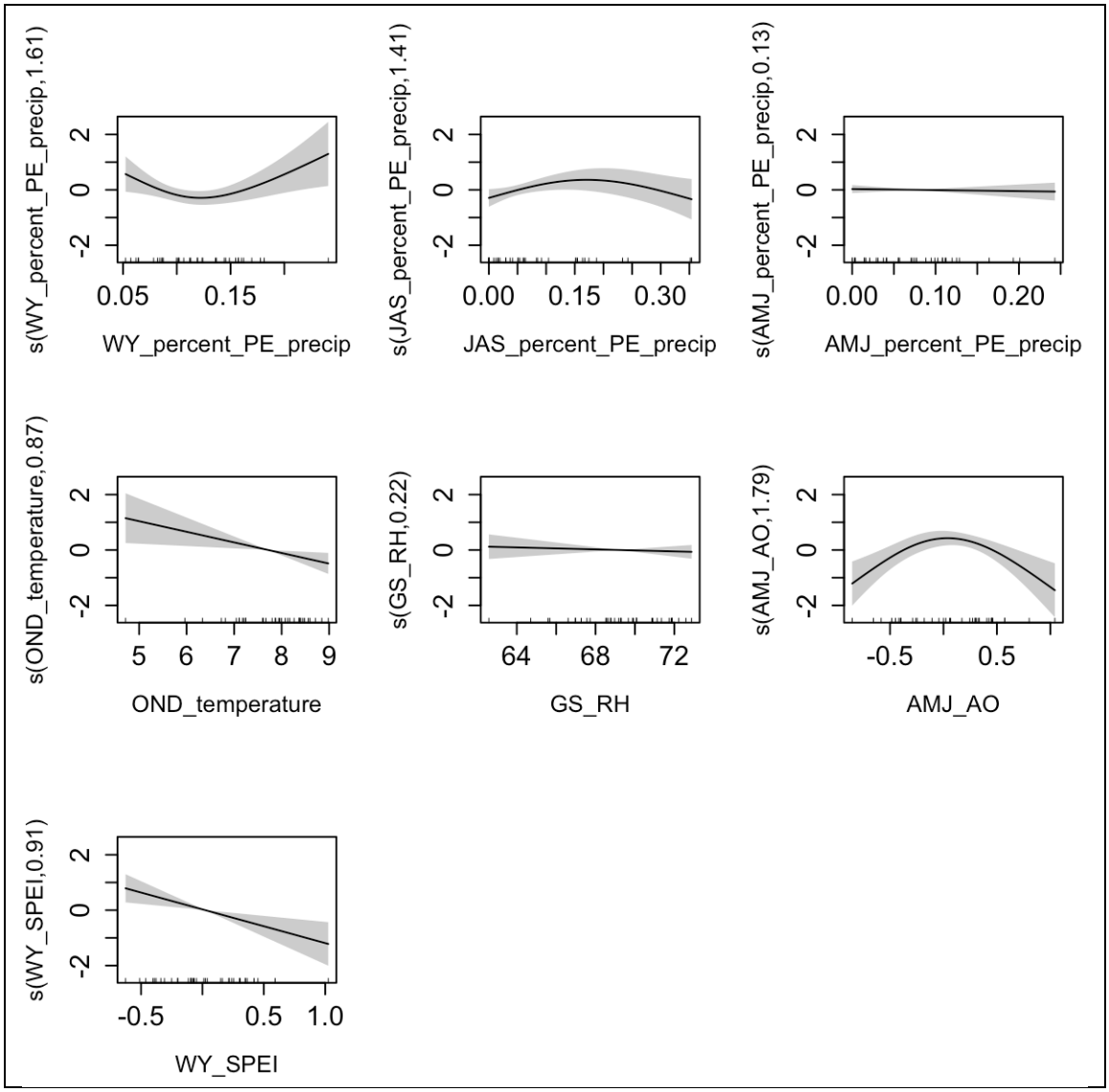

Figure 3.8 **Individual partial effects of the smooth functions of predictor variables on the Capilano $\delta^{18}O$ response variable. The predictor variables included are those retained (i.e., not penalized) in the final multi-predictor GAM. Y-axis values are zero-centered, and the numbers following the y-axis labels are the models' effective degrees of freedom in the GAM. The shaded area indicates the 95% confidence interval and small vertical lines on the x-axes denote the distribution of PE and climate data.**

MKRF-2 results

Results from single-predictor GAMs indicate significant (p<0.05) correlations between $\delta^{18}O$ and 13 predictor variables. Of PE predictor variables, only OND % PE precipitation had significant p values (Table C4). Significant climate oscillation indices were WY PDO, WY ENSO, AMJ ENSO, OND AO, and AMJ NPGO. Significant climate variables were AMJ mean temperature, WY total precipitation, OND total precipitation, WY SPEI, OND SPEI, WY mean SWE, and mean GS-RH (Table C4) with the direction of relationships shown in Figure 3.9.

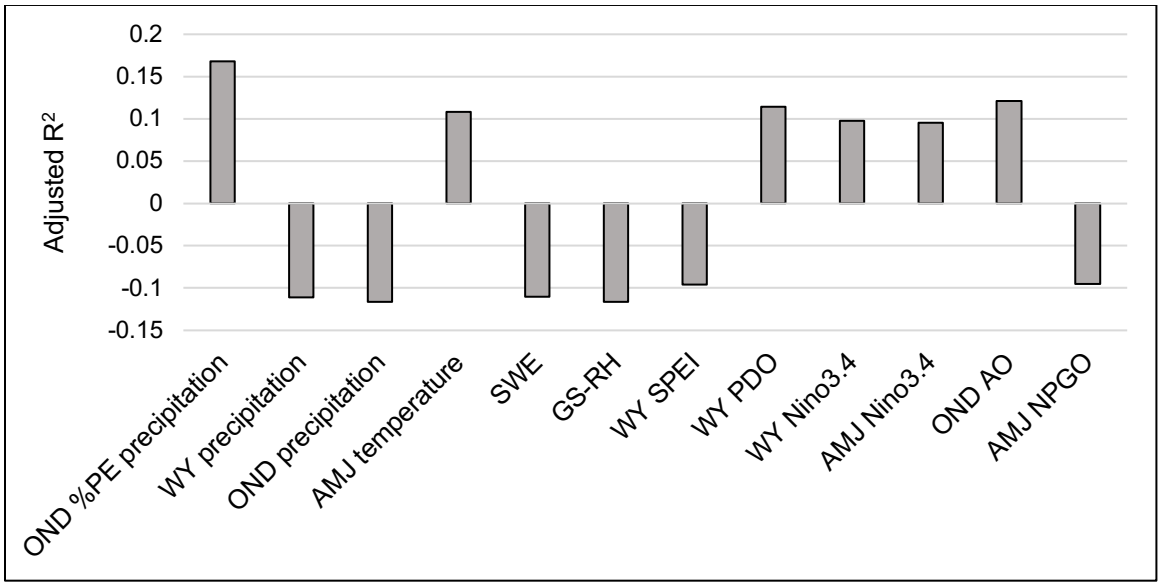

Figure 3.9 Variables with significant (p<0.05) relationships with $\delta^{18}O$ in MKRF-2 single-predictor GAMs. All significant variables displayed linear relationships with $\delta^{18}O$ in the GAMs. The sign of the adjusted R^2 values indicates the direction of the relationship (note that the directions of the relationships were assessed visually, as adjusted R^2 values do not have a sign).

To additionally evaluate the linear relationship between OND % PE precipitation and MKRF-2 $\delta^{18}O$, normality of the two variables was confirmed with Shapiro-Wilk tests and a post-hoc Pearson correlation coefficient was calculated. This revealed OND % PE precipitation as explaining 44% of MKRF-2 $\delta^{18}O$'s variance (r[34]=0.44, p=0.01).

Multi-predictor GAM results for MKRF-2 show an increased model R^2 when PE variables are included. While the significant (p<0.05) non-PE variables return a GAM with R^2=0.415 (GAM iteration 1), the final iteration which includes PE variables returns a GAM with R^2=0.428 (GAM iteration 9) (Table 3.5). However, AIC is higher when PE

variables are included in the GAM (AIC=104 at GAM iteration 1 vs. AIC=108 at the final GAM iteration) (Table 3.5).

Table 3.5 MKRF-2 multi-predictor GAM iterations. For variables with concurvity>0.5, only the underlined variables were retained in the subsequent GAM iteration.

GAM iteration	Variables	R^2 (adjusted)	Deviance explained (%)	AIC	Penalized variables	Non-penalized variables with concurvity above 0.5
1 Significant non-PE variables	OND SPEI OND AO OND precipitation WY precipitation Mean AMJ temperature SWE WY Niño 3.4 AMJ Niño 3.4 GS-RH AMJ NPGO WY SPEI WY PDO	0.415	48.7	104	WY precipitation Mean AMJ temperature SWE AMJ Niño 3.4 WY SPEI WY PDO	OND SPEI & <u>OND precipitation</u>
2 Remove penalized variables and high-concurvity variables, add PE variables	OND AO OND precipitation WY Niño 3.4 GS-RH AMJ NPGO OND % PE precipitation OND PE count JFM % PE precipitation WY PE count AMJ PE count AMJ % PE precipitation	0.428	50.3	108	OND % PE precipitation OND PE count JFM % PE precipitation AMJ PE count AMJ % PE precipitation	None

GAM iteration	Variables	R^2 (adjusted)	Deviance explained (%)	AIC	Penalized variables	Non-penalized variables with concurvity above 0.5
3 Remove penalized variables and add remaining PE variables	OND AO OND precipitation WY Niño 3.4 GS-RH AMJ NPGO WY PE count JAS PE count JAS % PE precipitation JFM PE count WY % PE precipitation	0.428	50.3	108	JAS PE count JAS % PE precipitation JFM PE count WY % PE precipitation	None
4 Remove penalized variables to create final GAM	OND AO OND precipitation WY Niño 3.4 GS-RH AMJ NPGO WY PE count	0.428	50.3	108	None	None

Variables retained in the final GAM iteration were OND AO, OND precipitation, WY Niño 3.4, GS-RH, AMJ NPGO, and WY PE count (Table 3.5). Only OND AO and OND precipitation had significant *p* values (Table 3.6).

Table 3.6 MKRF-2 final multi-predictor GAM results. *P* values <0.05 are shown in bold. EDF indicates the variable's estimated degrees of freedom in the GAM.

Predictor variable	EDF	*F* statistic	*p* value
OND AO	0.81	1.41	**0.03**
OND precipitation	0.86	2.02	**0.01**
WY Niño 3.4	0.50	0.33	0.15
GS-RH	0.63	0.56	0.10
AMJ NPGO	1.14	1.15	0.05
WY PE count	0.66	0.64	0.09

OND AO, WY Niño 3.4, and WY PE count have positive relationships with $\delta^{18}O$, while OND precipitation and GS-RH have negative relationships. AMJ NPGO has a non-linear but mostly negative relationship with $\delta^{18}O$ (Figure 3.10).

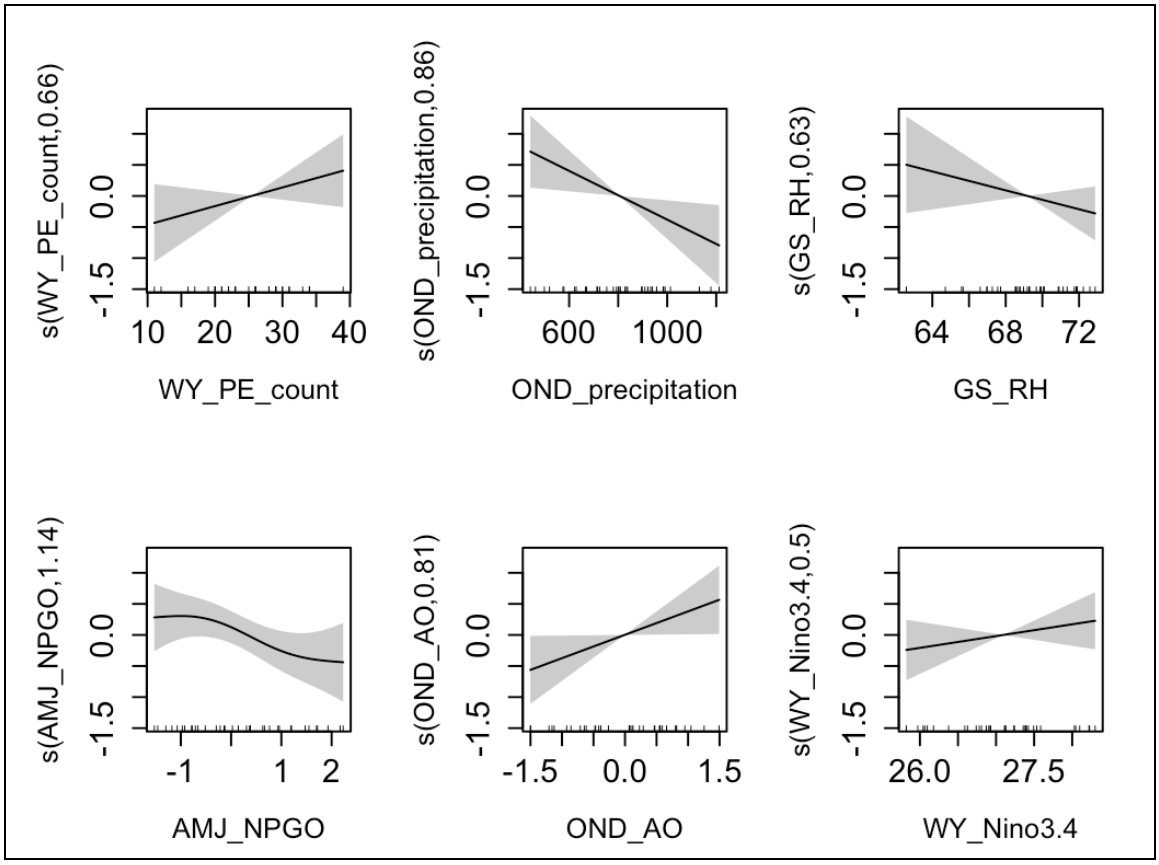

Figure 3.10 Individual partial effects of the smooth functions of predictor variables on the MKRF-2 $\delta^{18}O$ response variable. The predictor variables included are those retained (i.e., not penalized) in the final multi-predictor GAM. Y-axis values are zero-centered, and the numbers following the y-axis labels are the predictor variables' effective degrees of freedom in the GAM. The shaded area indicates the 95% confidence interval and small vertical lines on the x-axes denote the distribution of PE and climate data.

To evaluate relationships between predictor variables, a post-hoc Pearson correlation was calculated. After confirming normality with Shapiro-Wilk tests, Pearson correlations revealed a significant negative relationship between MKRF-2 OND % PE precipitation and mean SWE (r[32]=-0.48, p<0.01).

3.3.4. Site comparisons

GAMs indicated some overlap in the variables significantly related to the Capilano and MKRF-2 $\delta^{18}O$ records. Both sites' records were significantly related to GS-RH in single- and multi-predictor GAMs, and both sites' records were significantly related to SPEI in single-predictor GAMs. No other seasonalized significant variables were common between the sites, although the sites recorded significant relationships between $\delta^{18}O$ and % PE precipitation, temperature, SPEI, and AO in different seasons.

The Capilano and MKRF-2 $\delta^{18}O$ records were compared with each other and with nearby $\delta^{18}O$ records using Pearson correlations and hierarchical cluster analyses. Pearson correlation results show that the Capilano and MKRF-2 records were both most strongly correlated with each other ($r[39]=0.33$, $p=0.034$), with no other significant correlations found at the $p<0.05$ level (Table C5). Hierarchical cluster analyses revealed additional associations between sites' $\delta^{18}O$ records. In the first hierarchical cluster, Capilano and MKRF-2 $\delta^{18}O$ records were most similar to central Alaskan tree ring $\delta^{18}O$ records and most dissimilar to coastal Alaskan records (Figure 3.11). The second hierarchical cluster grouped the MKRF-2 and Capilano records together as a separate branch from the Washington, Idaho, and Oregon records (Figure 3.11).

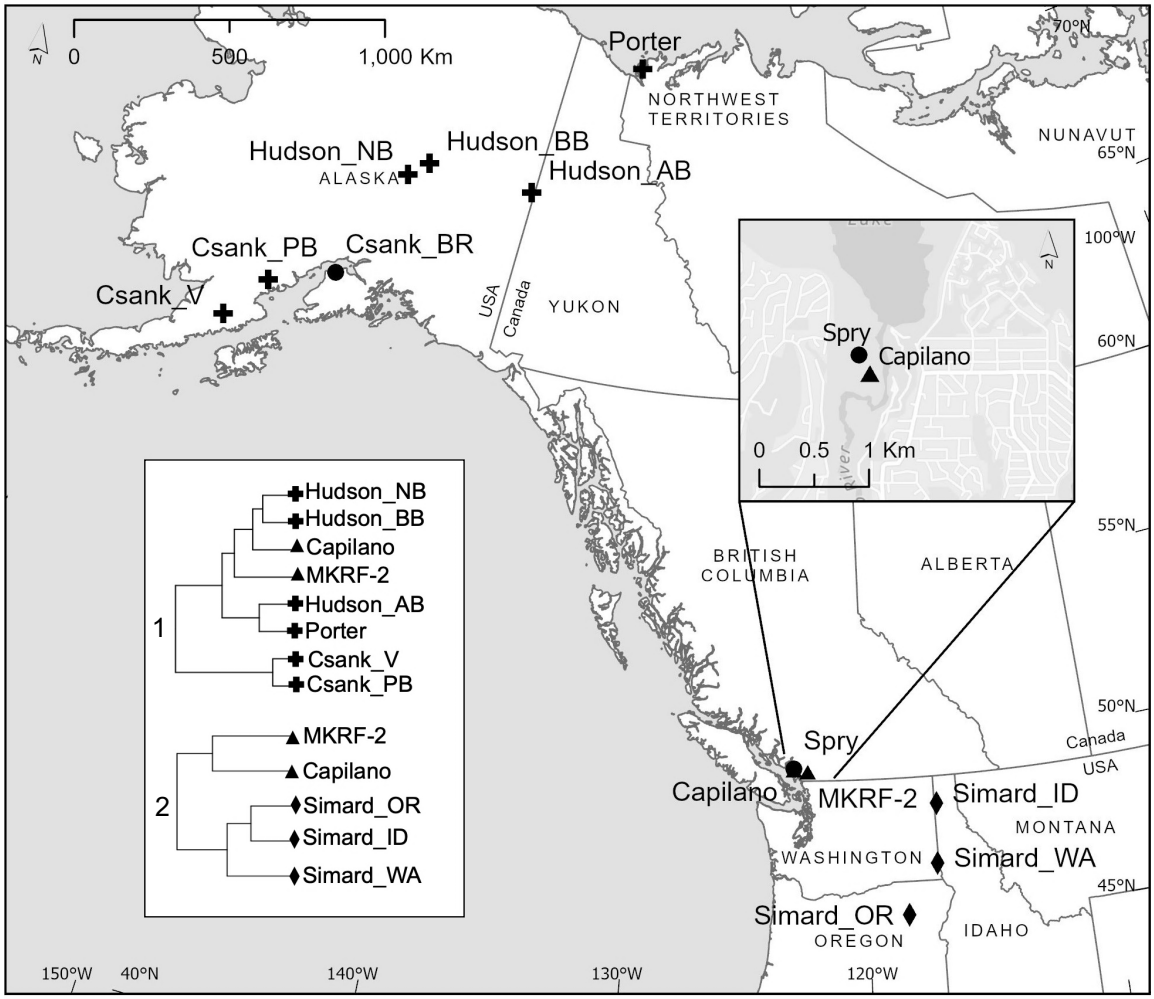

Figure 3.11 Locations of all available western North America cellulose $\delta^{18}O$ records overlaid with hierarchical cluster results for selected records (records with >1 tree per site and strong temporal overlap with the MKRF-2 and the Capilano records). Site symbols identify hierarchical cluster groupings, with triangles indicating the sites included in both groups and circles indicating the sites excluded from the hierarchical cluster analyses.

3.4. Discussion

3.4.1. Tree ring $\delta^{18}O$ as a PE proxy

This study's GAM results indicate that southwest BC tree ring $\delta^{18}O$ records documented a PE signature. Results from single-predictor PE GAMs (i.e., one PE variable compared with $\delta^{18}O$) identified only one PE variable, MKRF-2 OND % PE precipitation, as significant at the $p<0.05$ level. OND % PE precipitation varied linearly and positively with MKRF-2 $\delta^{18}O$ (Figure 3.7), and this linear relationship indicates the

potential for α-cellulose $\delta^{18}O$ to serve as a proxy for OND % PE precipitation, as linear regressions are typically applied in tree ring climate reconstructions (Speer, 2010). To confirm this point, a post-hoc Pearson correlation revealed that OND % PE precipitation explained 44% of MKRF-2 $\delta^{18}O$'s variance at a *p* value of 0.01. This finding establishes α-cellulose $\delta^{18}O$ as a meaningful proxy of OND % PE precipitation variability in southwest BC.

Whether PE-enriched water is responsible for this relationship, however, is uncertain. OND precipitation does not coincide with trees' growing seasons, so precipitation cannot be incorporated into trees' soil water at the time of, or shortly after, an OND precipitation event. However, initial rainfall after rainless summers has been found to persist in small soil pores throughout the winter in the PNW (Renée Brooks et al., 2010), potentially making OND precipitation available to trees at the start of their growing season. The positive relationship between MKRF-2 trees' $\delta^{18}O$ and OND % PE precipitation may reflect this relationship, though other PE effects on trees' environments may also explain the observed relationship. For example, PE-derived SWE effects on growing season lengths may drive the observed association between OND % PE precipitation and tree ring $\delta^{18}O$. Tree ring α-cellulose $\delta^{18}O$ has been found to negatively respond to snowpack depths across the globe (Foroozan et al., 2020; Qin et al., 2022), and Qin et al. (2022) attributes this to snowmelt's modulation of the start of springtime transpiration. Low snowpacks allow for transpiration to begin earlier in the year, and this enhances leaf water evaporative enrichment and α-cellulose $\delta^{18}O$ (Cooper et al., 2020; Roden et al., 2000). Persistent seasonal snowpacks occur at higher elevations in both the study sites' watersheds (Figure 3.2), and the timing of this snowpack's melt may affect soil temperatures, and thus the start of springtime transpiration (Mellander et al., 2004), at lower elevations such as at Capilano and MKRF-2. Additionally, the characteristically warm temperatures of cold-season PEs (Gonzales et al., 2022) make PEs likely to degrade snowpacks through rain-on-snow events (Guan et al., 2016). Therefore, years with frequent PEs may experience lower mountain snowpacks and an earlier snowmelt and start to spring transpiration, and this may cause the observed enriched α-cellulose $\delta^{18}O$. Considered together, OND PEs may enrich α-cellulose $\delta^{18}O$ if their precipitation water persists in soil pores throughout the winter, and they may also enrich α-cellulose $\delta^{18}O$ through snowpack depletion effects.

Multi-predictor GAM results affirm this mechanism. Despite OND % PE precipitation showing the strongest relationship of any tested climate variable by single-predictor GAM R^2, the multi-predictor GAM penalized this variable out of the model. This was likely a result of the model's regularization technique and automatic term selection, which can penalize redundant (i.e., correlated) predictors out of GAMs if other predictors better explain response data variability. While OND % PE precipitation was individually significant in the single-predictor GAM, the multi-predictor MKRF-2 GAM showed that other variables better explained the observed $\delta^{18}O$. This points to a variable correlated with PEs (e.g., SWE) as driving the OND % PE precipitation-$\delta^{18}O$ relationship, rather than the $\delta^{18}O$ signature of PE precipitation inputs.

However, the multi-predictor GAM results do indicate that PE variability affected $\delta^{18}O$ in a manner not explained by other predictor variables. Inclusion of PE data improved GAM model fit for both sites; for Capilano, the GAM adjusted R^2 increased by 0.111 with PE data inclusion, while for MKRF-2, GAM adjusted R^2 increased by 0.013. Although the GAMs for both sites showed increased R^2 with PE variable inclusion, AIC decreased when PE variables were included in the Capilano GAM (indicating a better-performing model), while AIC increased with PE variable inclusion for the MKRF-2 GAM (indicating a poorer-performing model). This increase in AIC may be a result of the final MKRF-2 including-PE model being more complex than the non-PE model, as model complexity increases AIC (Wagenmakers & Farrell, 2004). Regardless, the inclusion of PE variables in both sites' final GAMs while applying an automatic term selection penalization approach indicates that PE data explain $\delta^{18}O$ variability that is not explained by the other variables included in the models. PE variables' relationships with $\delta^{18}O$ in the final multi-predictor GAMs, alongside moisture, temperature, and climate oscillation relationships, are summarized in Figure 3.12.

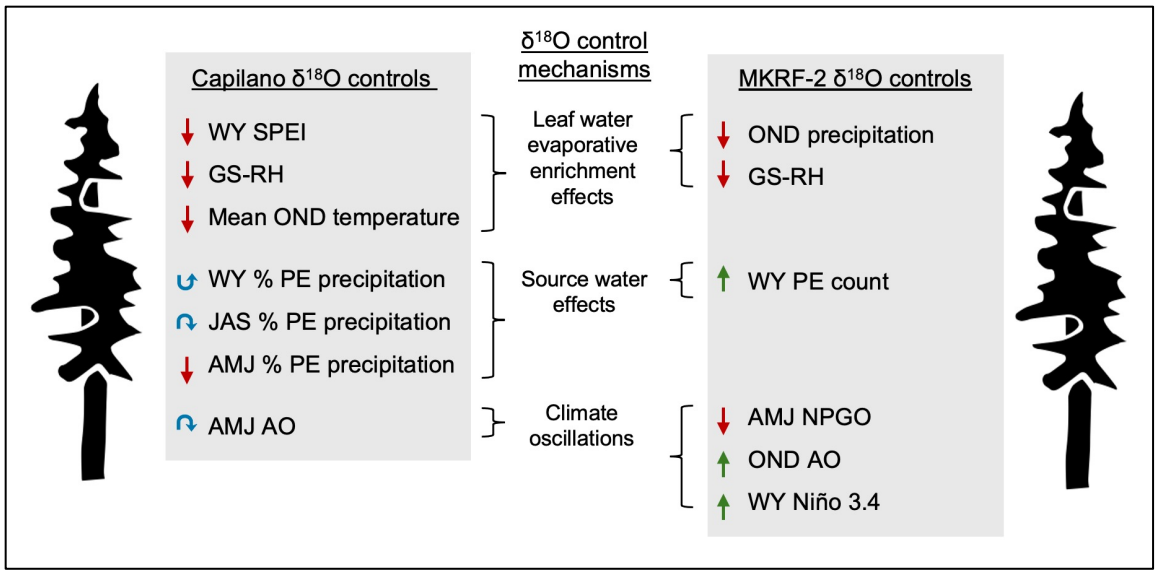

Figure 3.12 **PE and climate variables retained in the final Capilano and MKRF-2 multi-predictor GAMs, grouped by their $\delta^{18}O$ control mechanisms. Note that source water effects interact with leaf water evaporative enrichment effects and that climate oscillations can dictate the variability of the other two control mechanisms. Green upward arrows indicate a positive relationship between the variable and RWI, red downward arrows indicate a negative relationship between the variable and RWI, and blue curved arrows indicate a non-linear relationship between the variable and RWI as reflected in the direction of the curve. Tree image retrieved from McCune (2018).**

The PE variables retained in the final multi-predictor GAMs for both sites reveal interactions between exogenous controls on tree ring $\delta^{18}O$. For MKRF-2, the final GAM iteration identified a positive relationship between $\delta^{18}O$ and WY PE count, aligning with the hypothesis that $\delta^{18}O$-enriched water from PE storms affecting the area enriches α-cellulose $\delta^{18}O$. The Capilano chronology's recording of PE variability, however, was more nuanced. The final Capilano GAM showed a non-linear relationship between JAS % PE precipitation, with $\delta^{18}O$ increasing with JAS % PE precipitation from 0 - 15% and decreasing above 15% (Figure 3.8). This may be due to the behaviour of rainwater infiltration into soils during the dry season; PEs and AR storms generally tend to deliver intense precipitation (Waliser & Guan, 2017), which is more likely to exceed the maximum infiltration capacities of soils and generate more infiltration excess overland flow relative to less intense precipitation events (Bronstert et al., 2023). PE precipitation may, then, exceed the infiltration capacities of soils such that much of the precipitation leaves the catchment as overland flow and is unavailable to trees. For southwest BC, this scenario may be exacerbated during the region's dry summers (Odon et al., 2019),

when infrequent rain creates dry soils prior to PE events. The soil type at Capilano, sandy loam (Province of British Columbia, 2018), is especially water repellent under antecedent drought conditions (Gimbel et al., 2016). This combination of factors may create the nonlinear $\delta^{18}O$ – JAS % PE precipitation trend observed at Capilano. Under low JAS % PE precipitation conditions, PE precipitation more readily infiltrates the soil and is available for incorporation into trees' α-cellulose, creating the positive relationship between α-cellulose $\delta^{18}O$ and low JAS % PE precipitation. Meanwhile, under high JAS % PE precipitation, PE precipitation (received through intense rain events) is more likely to exceed the soil's infiltration capacity and be unavailable to trees, leading to a negative trend. Together, these may explain the non-linear relationship observed.

The non-linear PE relationship recorded at Capilano is further clarified by the other PE variable retained in Capilano's final GAM: WY % PE precipitation. For this variable, the final GAM identified a negative relationship between the two for 0 - 12% WY PE precipitation and a positive relationship for WY PE precipitation higher than 12%, i.e., a U-shaped curve (Figure 3.8). The shape of this relationship is opposite to that of JAS % PE precipitation, likely a result of PEs interacting with snowpacks to affect $\delta^{18}O$. Due to their subtropical origin, PEs tend to be warm storms (Gonzales et al., 2022), making cold-season PEs likely to deplete snowpacks through rain-on-snow events (Dettinger, 2004; Guan et al., 2016). This can cause earlier snowmelts, which enhance leaf water evaporative enrichment and therefore enhance tree ring α-cellulose $\delta^{18}O$, as described above. This PEs precipitation is likely enriched in $\delta^{18}O$ (Spry et al., 2014), but winter precipitation falling as rain does not coincide with trees' growing season and therefore is unlikely to be recorded in trees' α-cellulose. However, if winter PE precipitation falls as snow, its springtime melt *is* more available to trees as they grow. Such a PE snow contribution is more likely at low % PE precipitation than high % PE precipitation due to PEs' warm temperatures. These relationships can be summarized as: PE incidence and SWE relate negatively, PE incidence and α-cellulose $\delta^{18}O$ relate positively, and SWE and α-cellulose $\delta^{18}O$ relate negatively. The shape of the WY % PE precipitation curve reflects this interaction (Figure 3.8). At low WY % PE precipitation, PEs minimally degrade snowpacks, allowing PE precipitation to store in snow and become available to trees, but this PE enrichment of α-cellulose $\delta^{18}O$ decreases as % PE precipitation increases and the snowpack diminishes. Meanwhile, at high WY % PE

precipitation, PEs greatly reduce snowpacks, enhancing leaf water evaporative enrichment and α-cellulose $\delta^{18}O$ through earlier snowmelt.

The lack of significant relationships between any WY or seasonalized intense PE count variable and $\delta^{18}O$ at either site (Tables C3, C4) may point to these intense storms' precipitation rapidly leaving catchments. While lower-intensity precipitation is more likely to infiltrate soil and persist longer in catchments, higher-intensity precipitation is more likely to rapidly leave a catchment as overland flow (Bronstert et al., 2023), thus precluding its incorporation into cellulose $\delta^{18}O$.

Overall, these results indicate that PE variability affects α-cellulose $\delta^{18}O$ in a manner not explained by other climate variables included in the models. Some PE effects may be due to source water inputs, but other PE effects are better clarified by PEs' interactions with other climate variables affecting α-cellulose $\delta^{18}O$ such as SWE and soil infiltration rates. Despite this, the significant linear relationship between MKRF-2 OND % PE precipitation and α-cellulose $\delta^{18}O$ indicates the potential for α-cellulose $\delta^{18}O$ to reconstruct historical PE variability beyond instrumental records.

3.4.2. Additional sources of $\delta^{18}O$ variability

In addition to PE variability, the variability of several climate measures appeared to affect tree ring $\delta^{18}O$ at Capilano and MKRF-2. One such variable, GS-RH, varied with $\delta^{18}O$ at both sites and demonstrated a significant negative relationship with both sites' $\delta^{18}O$ in single-predictor GAMs (Figures 3.7, 3.9) and non-significant negative relationships in the final multi-predictor GAMs (Figures 3.8, 3.10). These results are consistent with negative relationships identified between GS-RH and tree ring cellulose $\delta^{18}O$ documented in other studies (An et al., 2014; Churakova (Sidorova) et al., 2023; Labuhn et al., 2014; Shi et al., 2011; Y. Wu et al., 2023), a probable result of leaf water evaporative enrichment effects (Roden et al., 2000). When trees transpire, the lighter (^{16}O-containing) water molecules preferentially evaporate from leaves before the heavier (^{18}O-containing) water molecules. Leaf water (and its $\delta^{18}O$) form the trees' sucrose, which developing cambial cells break down to form the cellulose composing the year's growth ring (Roden et al., 2000). RH, which strongly mediates stomatal conductance, enhances transpiration rates at low RH and suppresses transpiration rates at high RH (Grantz, 1990). The relationship between RH and α-cellulose $\delta^{18}O$, then, is negative; low

GS-RH enriches α-cellulose $\delta^{18}O$, while high GS-RH depletes it (Roden et al., 2000). This aligns with the GS-RH relationships observed at Capilano and MKRF-2 as well as SPEI results. WY SPEI, which increases with RH (Beguería et al., 2010), varied significantly negatively with $\delta^{18}O$ in the Capilano single- and multi-predictor GAMs and the MKRF-2 single-predictor GAM. Together, these results indicate a strong GS-RH effect on MKRF-2 and Capilano α-cellulose $\delta^{18}O$.

Both WY and season-specific precipitation amounts also showed relationships with $\delta^{18}O$, including significant relationships in the MKRF-2 GAMs. WY precipitation varied negatively with MKRF-2 $\delta^{18}O$ in the single-predictor GAM (Figure 3.9), while OND precipitation varied negatively with MKRF-2 $\delta^{18}O$ in both single and multi-predictor GAMs (Figures 3.9, 3.10). This result is likely a combination of leaf water evaporative enrichment effects and the "amount effect." Precipitation varies positively with RH, supporting a negative relationship between precipitation and cellulose $\delta^{18}O$ due to evaporative enrichment as also documented in Tsuji et al. (2006) and Sano et al. (2013). The amount effect, which refers to the negative relationship often observed between meteoric water $\delta^{18}O$ and precipitation amounts (Vystavna et al., 2021), occurs due to the preferential precipitation of heavy water molecules. At low precipitation amounts, only a heavier ($\delta^{18}O$-enriched) fraction of water vapour precipitates, while at high precipitation amounts, more of the total water vapour plume precipitates, contributing more ^{16}O-containing water to an area (Dansgaard, 1964). The combination of these two negative associations likely shaped the negative α-cellulose $\delta^{18}O$-precipitation amount relationships identified at MRKF-2.

Temperature also demonstrated an effect on tree ring $\delta^{18}O$, with AMJ temperature showing a significant positive relationship with $\delta^{18}O$ in the MKRF-2 single-predictor GAM (Figure 3.9). This positive relationship is consistent with trends identified in similar tree ring cellulose $\delta^{18}O$ studies (Labuhn et al., 2014; Rebetez et al., 2003; Saurer et al., 2008; Shi et al., 2011; G. Xu et al., 2014), an association derived from the evaporative enrichment of soil water with increasing temperatures (Sano et al., 2013). However, OND temperature showed significant negative relationships with Capilano $\delta^{18}O$ in both the single- and multi-predictor GAMs (Figures 3.7, 3.8), a potential result of PE and SWE effects. Considering that the negative temperature- $\delta^{18}O$ relationship was only significant for OND and that PEs are most frequent in the OND season at Capilano (Figure 3.6), an OND-SWE interaction may be driving the observed association. In

warmer fall seasons, PE precipitation is more likely to rapidly leave the site catchment as overland or subsurface flow than persist throughout the cold season as snowpack. This means that PE-derived enriched $\delta^{18}O$ is less likely to be available to trees during their growing season as snowmelt for warm OND seasons compared to cooler ones, driving down $\delta^{18}O$ as temperature increases. The seasonality of both sites' trends strongly aligns with the findings of Xu et al. (2014); that study identified negative correlations between tree cellulose $\delta^{18}O$ and cold-season temperature and positive correlations with warm-season temperature. Although that study's location precludes it from PE effects, the results agree with those found at MKRF-2 and Capilano in that cold season temperature's effect on $\delta^{18}O$ deviates from the expected trend driven by soil water evaporative enrichment.

The simultaneous SWE, GS-RH, precipitation amount, and SPEI associations with the Capilano and MKRF-2 $\delta^{18}O$ records indicate a strong moisture availability control on tree ring $\delta^{18}O$. While this study did not specifically assess tree ring $\delta^{18}O$'s use as a drought proxy, similar studies have extended drought history by centuries using tree ring $\delta^{18}O$ (Labuhn et al., 2016; G. Xu et al., 2014, 2019). The use of tree ring stable isotopes to infer PNW drought history has not been thoroughly explored; however, future research could investigate its value in the region.

Several climate oscillations also showed significant relationships with the MKRF-2 and Capilano $\delta^{18}O$ records, including ENSO and PDO. WY PDO, WY Niño 3.4, and AMJ Niño 3.4 all varied positively with $\delta^{18}O$ in MKRF-2 single-predictor GAMs (Figure 3.9). PDO, sometimes described as a long-lived ENSO-like pattern of climate variability (Mantua & Hare, 2002) affects Pacific climates similarly to ENSO through cyclic variation in Pacific Ocean surface temperatures (Mantua & Hare, 2002; McPhaden et al., 2020). The positive phases of Niño 3.4 and the PDO index are associated with warmer temperatures in the PNW (Mantua & Hare, 2002; Yu et al., 2015), which aligns with the significant positive AMJ temperature-$\delta^{18}O$ relationship flagged in the MKRF-2 single-predictor GAM (Figure 3.9).

The AMJ NPGO index also showed a significant negative relationship with MKRF-2 $\delta^{18}O$ in the single-predictor GAM (Figure 3.9). The NPGO drives cyclic variation in sea surface temperature and height in the northeast Pacific Ocean, with negative NPGO phases associated with warmer SST along the North American Pacific Coast (Di

Lorenzo et al., 2008). SST varies positively with PNW air temperature, with the most significant correlations observed in spring and summer months (Mass et al., 2022). This spring and summer NPGO-air temperature effect may be driving the negative NPGO-$\delta^{18}O$ relationship at MKRF-2; the negative NPGO phases increase coastal PNW SST and air temperatures, which then increase α-cellulose $\delta^{18}O$. AMJ temperature varied significantly positively with $\delta^{18}O$ at MKRF-2 (Figure 3.9), aligning with the negative AMJ NPGO-$\delta^{18}O$ relationship.

The AO also showed significant positive relationships with α-cellulose $\delta^{18}O$. OND AO varied positively with MKRF-2 $\delta^{18}O$ in single and multi-predictor GAMs (Figures 3.9, 3.10), while AMJ AO varied non-linearly in Capilano single and multi-predictor GAMs with negative partial effects on $\delta^{18}O$ in positive and negative AO phases and positive partial effects on $\delta^{18}O$ in the neutral phase (Figures 3.7, 3.8). The MKRF-2 positive association between OND AO and $\delta^{18}O$ may be a result of the AO's modulation of winter snowpack. AO- (negative phase) is associated with more frequent cold air outbreaks to the mid-latitudes (Smith & Sheridan, 2022), and negative associations between the AO index and SWE have been identified in North America (Liner et al., 2022), with greater SWE during AO-. Additionally, SWE itself varies significantly negatively with $\delta^{18}O$ at MKRF-2 (Figure 3.9). Through this relationship, AO- may support high SWE and low α-cellulose $\delta^{18}O$ through delayed snowmelt and the suppression of leaf water evaporative enrichment. Although little research exists assessing tree ring $\delta^{18}O$ relationships with AO, Churakova Sidorova et al. (2021) did flag SWE as a potential modulating factor in the AO-tree ring $\delta^{18}O$ relationship. Meanwhile, the nonlinear relationship between Capilano $\delta^{18}O$ and AMJ AO may also be a result of SWE effects on $\delta^{18}O$. At AMJ AO-, which supports more frequent AMJ cold outbreaks to the mid-latitudes (Smith & Sheridan, 2022), the timing of snowmelt is likely to be later in the year due to cooler temperatures, reducing α-cellulose $\delta^{18}O$ through suppression of leaf water evaporative enrichment. This explains the positive trend (left side) of the Capilano AMJ AO-$\delta^{18}O$ relationship. However, warm moisture transport in the positive AMJ AO phase (AO+) may explain the negative trend (right side) of this relationship. Moisture transport above the east Pacific coast is enhanced in AO+ relative to neutral AO (Sun et al., 2022), potentially increasing RH and driving down $\delta^{18}O$ through the suppression of leaf water evaporative enrichment (Roden et al., 2000). While moisture transport above the east Pacific coast is also enhanced in AO- relative to neutral AO (Smith & Sheridan, 2022),

the colder AMJ AO- precipitation is more likely to delay snowmelt and suppress leaf water evaporative enrichment, while the warmer AMJ AO+ precipitation is more likely to contribute to high-RH suppression of leaf water evaporative enrichment, creating the non-linear trend observed. A similar relationship was hypothesized in Churakova Sidorova et al. (2021), who found a significant relationship between subarctic tree ring $\delta^{18}O$ and May AO and attributed the relationship to warm temperature effects of AO+ on snowmelt timing and evapotranspiration. The AO is also known to impact climates in a non-linear manner (Son et al., 2012; A. Wu et al., 2006), supporting the non-linear $\delta^{18}O$ effects observed at Capilano. The shape of the AO trend additionally supports the use of GAMs in this study, as the non-linear AO trend would not have been captured by a linear analysis.

Endogenous controls on α-cellulose $\delta^{18}O$ may have also impacted Capilano and MKRF-2 results, though these were not explored in this study. The rate of isotopic exchange with xylem water prior to cellulose synthesis has been shown to affect cellulose $\delta^{18}O$, with older trees capturing lower $\delta^{18}O$ in their new growth due to enhanced isotopic exchange with xylem water (Nakatsuka et al., 2020). Soil water $\delta^{18}O$ also varies with depth (Brinkmann et al., 2018), with shallow-rooting trees accessing soil water more representative of meteoric water $\delta^{18}O$ and deeper-rooting trees accessing groundwater with a more muted $\delta^{18}O$ response to meteoric water inputs (McCarroll & Loader, 2004b). Both rooting depth and the rate of xylem water isotopic exchange are functions of tree age (McCarroll & Loader, 2004b; Nakatsuka et al., 2020), potentially skewing the meteoric water $\delta^{18}O$ recorded by trees over time. To minimize this confounding effect, this study only analyzed the most recent 40 years of growth from centuries-old trees; however, these age-related effects may have influenced the results.

Overall, the results indicate that non-PE sources of $\delta^{18}O$ variability affected MKRF-2 and Capilano $\delta^{18}O$, including many moisture variables. These results generally align with known α-cellulose $\delta^{18}O$ responses to trees' environments, with some atypical results potentially derived from compounding SWE-PE and SWE-RH effects.

3.4.3. Regional context

Differences between the Capilano and MKRF-2 $\delta^{18}O$ records reveal exogenous controls on tree ring $\delta^{18}O$. Mean $\delta^{18}O$ was 0.89 ± 0.15‰ higher at MKRF-2; this may be

due to the site's 0.8°C warmer mean temperature over the study period (ECCC, 2023c, 2023b), as AMJ temperature conferred an $\delta^{18}O$ enrichment effect at MKRF-2 and similar positive associations between tree ring $\delta^{18}O$ and temperature have been documented elsewhere (Labuhn et al., 2014; Rebetez et al., 2003; Saurer et al., 2008; Shi et al., 2011; G. Xu et al., 2014). Mean MKRF-2 $\delta^{18}O$ may be additionally enriched due to the larger contribution of PE precipitation to total WY precipitation compared to Capilano (Figure 3.6). Moreover, the greater increase in the Capilano multi-predictor GAM adjusted R^2 after PE variable inclusion, relative to MKRF-2, may be a result of the site's nearer proximity to the coast. Heavier (^{18}O-containing) water molecules precipitate before lighter (^{18}O-containing) ones (McCarroll & Loader, 2004b), making Capilano likely to receive more of PE storms' enriched $\delta^{18}O$ than MKRF-2.

Despite differences between the records, Capilano and MKRF-2 $\delta^{18}O$ appear to have recorded site- and region-wide climate signals. The two sites' $\delta^{18}O$ records showed a significant positive correlation with each other (Table C5), a probable result of the sites' <50 km proximity and resulting similar environmental and source water conditions. This indicates that the two sites recorded a similar regional signal. Assessment of the individual $\delta^{18}O$ records also suggests that each record documented a site-wide signal, with $\delta^{18}O$ for all non-pooled years but one being less dispersed than the site's entire $\delta^{18}O$ record (Figure 3.4). Additionally, although trees do not record identical $\delta^{18}O$ in non-pooled years (Figure 3.3), the trees do appear to record similar inter-annual trends. For example, all MKRF-2 trees recorded 2011 as having the lowest $\delta^{18}O$ of the non-pooled years, and three of four Capilano trees recorded 1981 as having the highest $\delta^{18}O$ of the non-pooled years (Figure 3.5). While such trends are not consistent for all non-pooled years (Figure 3.5), the existence of the noted trends suggests that trees recorded similar inter-annual trends in their $\delta^{18}O$. Overall, site-wide signals appear to have been captured at Capilano and MKRF-2.

Comparison with other North American tree ring $\delta^{18}O$ records additionally contextualize the Capilano and MKRF-2 records. The hierarchical cluster analysis between this study's sites and tree ring $\delta^{18}O$ records to the north reveal that the Capilano and MKRF-2 records are more similar to central Alaskan tree ring $\delta^{18}O$ records than coastal Alaskan or northern Northwest Territories records (Figure 3.11). A second hierarchical cluster analysis grouped the Capilano and MKRF-2 records separately from Oregon, Idaho, and Washington records (Figure 3.11). Together, these results indicate

that Capilano and MKRF-2 recorded a unique PNW $\delta^{18}O$ signal with some similarity to central Alaskan signals and less similarity to coastal signals.

3.4.4. Water resource management implications

The significant relationships between PE variables and tree ring $\delta^{18}O$ identified in this study indicate the capacity for tree ring $\delta^{18}O$ to reconstruct past PE trends. While this study measured α-cellulose $\delta^{18}O$ for years within the instrumental PE record, tree ring $\delta^{18}O$ records older than the mid-20th century satellite era can extend knowledge of historical PE variability by decades or centuries. The strength of such a reconstruction could additionally improve with the use of more finely attuned PE data, as PE datasets that identify PEs by their sub-tropical origins and storm track exist (e.g., Dettinger [2004]) but were not applied in this study as they do not use the most modern reanalysis algorithms. Reconstructions of PE variability using tree ring $\delta^{18}O$ may reveal even stronger relationships than found in this study if a modern-quality reanalysis record of PEs, identified by their subtropical origin and storm track, becomes available in the future.

The PNW's unique water resource management context makes such a reconstruction especially valuable. The PNW generally experiences wet winters and dry summers (Peel et al., 2007), with mountain snowpacks serving as natural reservoirs to offset low summer precipitation, sustain summer streamflow, and meet warm-season water demands (Metro Vancouver, 2019b; Pike et al., 2011; Vano et al., 2015). Many human-made reservoirs in the PNW rely on this snowmelt regime for in-season resupply; for example, the PNW's Columbia River dams can only store about 30% of the watershed's average yearly runoff at a time (Federal Columbia River Power System et al., 2001). As climate change brings longer summer dry spells and warmer year-round temperatures to the PNW (Curry & Sobie, 2023; Mote & Salathé, 2010), snowmelt-modulated water resources are likely to become more tenuous (Siirila-Woodburn et al., 2021). This trend may be consequential in warmer and lower-elevation PNW watersheds such as the Capilano watershed serving the Metro Vancouver, BC water supply. Dierauer et al. (2021) projects this catchment to experience a >90% decrease in peak SWE and earlier melt-out for the 2080s relative to the 1980s under a high-emissions climate scenario. Climate change is also projected to drive more frequent and severe snow droughts in the Capilano watershed, with snow droughts more likely to propagate

into summer streamflow drought conditions as the climate warms (Dierauer et al., 2021). In response to these projections, municipal water management agencies in the region have identified a need to expand water storage capacity to avert summer water shortages in the coming decades (Metro Vancouver, 2019b; Seattle Public Utilities, 2019).

PEs are likely to especially challenge PNW water resources in a warming climate. While the intense precipitation characteristic to ARs contributes to snowpacks and has broken droughts across North America (Chen et al., 2018; Dettinger, 2013; Eldardiry et al., 2019; Waliser & Guan, 2017), PEs may not provide the same beneficial contributions to water budgets. The warmer temperatures of PEs relative to non-PE ARs makes them more likely to precipitate as rain than snow (Gonzales et al., 2022), and higher AR temperature is associated with higher rain-on-snow-triggered snowpack degradation (Guan et al., 2016). Therefore, despite providing substantial moisture inputs in cold seasons, PEs may reduce winter snowpacks, thus reducing warm-season streamflow in catchments with snowmelt-modulated hydrological regimes. Alongside the PNW's snow and summer streamflow drought projections, the intensification and increased rain fraction of PEs with climate change (Gonzales et al., 2022; Payne et al., 2020) may increasingly deplete snowpacks and dictate summer water availability for municipal, agricultural, fisheries, and industrial needs as the climate warms.

Considering this challenging context, tree ring $\delta^{18}O$ records of historical PE variability can provide important knowledge to inform future water resource management. In the PNW, past AR variability is relatively consistent with projected future trends (compared to the larger increases in AR frequency and intensity projected for California and northwest BC (Radić et al., 2015; Shields & Kiehl, 2016a). Therefore, knowledge of historical PE variability, and particularly the frequency and extent of past high-PE and low-PE years, can inform the likely frequency and extent of this variability the future. This future-facing perspective is vital for clarifying water storage capacity needs in catchments with snowmelt-modulated hydrological regimes. If high-PE years increasingly exacerbate snow drought as the climate warms, knowledge of the extent and frequency of high-PE years can inform the water volumes needed to accommodate concomitant low-streamflow summers. As a whole, PE trends revealed using tree ring $\delta^{18}O$ are a valuable potential source of knowledge to inform plans for future water storage capacity needs in the PNW's changing climate.

3.5. Conclusions

This study establishes tree ring $\delta^{18}O$ as a viable proxy record for PE contribution to fall precipitation. PEs affected Capilano and MKRF-2 $\delta^{18}O$ distinctly from other environmental controls on tree ring $\delta^{18}O$, with WY % PE precipitation, WY PE count, and JAS % PE precipitation associated with higher $\delta^{18}O$ and AMJ % PE precipitation associated with decreased $\delta^{18}O$ in multi-predictor GAMs. While most results point toward PE effects on moisture availability as the primary α-cellulose $\delta^{18}O$ control mechanism, some PE-$\delta^{18}O$ relationships suggest that $\delta^{18}O$-enriched PE precipitation may have elevated α-cellulose $\delta^{18}O$. In multi-predictor GAMs, PE signals were recorded alongside similarly influential environmental signals (OND temperature, OND precipitation, GS-RH, and WY SPEI) and climate oscillation indices (AMJ AO, OND AO, AMJ NPGO, and WY Niño 3.4), additionally pointing to moisture availability's control on α-cellulose $\delta^{18}O$. This study also shows that GAMs are an effective means of evaluating interrelated and potentially non-linear predictors of $\delta^{18}O$ variability, as relationships between SWE and GS-RH likely explained other predictors' non-linear effects on $\delta^{18}O$. Overall, this study demonstrates evidence for the potential creation of a centuries-long record of PE variability using tree ring $\delta^{18}O$. Considering the ability of PEs to compound the effects of climate change on future PNW snow and streamflow droughts, a long-lived PE proxy record would provide valuable information to inform future water resource management in the region.

Chapter 4. General Conclusions

This research evaluated two dendrochronological methods, tree ring width and tree ring $\delta^{18}O$, for their ability to document historical atmospheric river (AR) variability in the Pacific Northwest (PNW). Chapter 2 presented annual growth and earlywood radial growth Pacific silver fir chronologies from southwest British Columbia (BC), 1931-2021. Generalized Additive Models (GAMs) revealed that AR data explained variability in these records that was not explained by other climate data, an indication that the sampled trees recorded a unique AR signal in their radial growth. This was a novel finding for southwest BC, as previous radial growth reconstructions of AR variability had not evaluated the Canadian west coast. The observed relationships between ARs and radial growth varied with AR intensity; while high total AR counts were associated with high radial growth, high intense (90^{th} percentile of daily precipitation) ARs were associated with low radial growth. The influence of AR intensity on snow-water equivalent (SWE) and soil moisture appeared to drive these trends, with intense ARs and concomitant high cold-season SWE and warm-season overland flow appearing to constrain radial growth, while total ARs, with concomitant low cold-season SWE, appeared to enhance radial growth.

Chapter 3 presented two tree ring $\delta^{18}O$ records from Douglas-firs in southwest BC, both 1981-2021. GAMs showed that Pineapple Express (PE) AR data explained $\delta^{18}O$ variability not explained by other tested environmental controls on $\delta^{18}O$ at both sites, indicating that the sampled trees' $\delta^{18}O$ responded to interannual PE AR variability. To our knowledge, these are the first tree ring $\delta^{18}O$ records showing a PE AR signal in North America. However, most of the observed PE AR-$\delta^{18}O$ relationships point to PE AR effects on moisture and transpiration, rather than PE AR enriched $\delta^{18}O$ inputs, as the primary α-cellulose $\delta^{18}O$ control mechanisms. PE AR signals were recorded alongside similarly influential environmental signals (fall temperature, fall precipitation, growing season relative humidity, and water year Standardized Precipitation Evaporation Index (SPEI) and climate oscillation indices (spring Arctic Oscillation [AO], fall AO, spring North Pacific Gyre Oscillation, and water year Niño 3.4) in the GAMs, supporting the posited moisture and transpiration controls on α-cellulose $\delta^{18}O$.

Evaluated together, southwest BC tree ring $\delta^{18}O$ exhibits stronger potential as a proxy record for historical PE AR variability than radial growth as a proxy for all ARs. The PE AR variable most strongly associated with $\delta^{18}O$, the percentage of fall precipitation from PEs, explained 44% of $\delta^{18}O$ variance at the MKRF-2 site. This relationship strength is similar to that documented in tree ring $\delta^{18}O$ moisture source and variability reconstructions (e.g., Labotka et al., 2016; Roden & Ehleringer, 2007; Shi et al., 2011; Xu et al., 2013). Meanwhile, the AR variable most strongly associated with radial growth, spring intense AR count, explained 32% of earlywood variance. This is much weaker than the strength of radial growth-AR relationships identified in coastal California, which commonly explain >50% of AR variance (Steinschneider et al., 2018). In this context, tree ring $\delta^{18}O$ is the more informative method for evaluating past AR variability in southwest BC. Although this method is limited to PE AR reconstructions, rather than all ARs, PE ARs exhibit distinct hydroclimate impacts compared to non-PE ARs (Gonzales et al., 2022). This makes PE ARs an important area of study and supports the creation of a potentially centuries-long southwest BC tree ring $\delta^{18}O$ record for use as a historical PE AR proxy record.

This research identified multiple points of future inquiry. The opposite associations of all ARs and intense ARs on southwest BC radial growth indicate that future AR-radial growth analyses should disaggregate AR data by intensity, as this may most clearly illuminate AR effects on radial growth. Future analysis of southwest BC drought history could also look to tree ring $\delta^{18}O$ as a proxy record, as this research identified strong associations between tree ring $\delta^{18}O$ records and historical moisture availability trends. Additionally, if a modern-quality reanalysis record of PE ARs – identified by their subtropical origin and storm track – becomes available, future research should evaluate this record's relationships with tree ring $\delta^{18}O$. This would improve upon this study's assessment of tree ring $\delta^{18}O$ as a PE AR proxy record.

ARs and climate change pose existential threats to the PNW's water resource management regime, and this research clarifies the ability of dendrochronological records to contextualize present and future AR-driven hydrological change. Such dendrochronological records are especially valuable in distinguishing the long-term frequency and extent of high and low AR occurrence years. As water resource managers in the PNW look to adapt water storage capacity to accommodate reduced snowpacks and meet warm-season water demands (Metro Vancouver, 2019b; Seattle

Public Utilities, 2019), dendrochronological records – and especially tree ring $\delta^{18}O$ – present a meaningful source of historical hydroclimate knowledge to inform this adaptation.

References

Albright, W. L., & Peterson, D. L. (2013). Tree growth and climate in the Pacific Northwest, North America: A broad-scale analysis of changing growth environments. *Journal of Biogeography*, *40*(11), 2119–2133. https://doi.org/10.1111/jbi.12157

An, W., Liu, X., Leavitt, S. W., Xu, G., Zeng, X., Wang, W., Qin, D., & Ren, J. (2014). Relative humidity history on the Batang-Litang Plateau of western China since 1755 reconstructed from tree-ring δ18O and δD. *CLIMATE DYNAMICS*, *42*(9–10), 2639–2654. https://doi.org/10.1007/s00382-013-1937-z

Araguás-Araguás, L., Froehlich, K., & Rozanski, K. (2000). Deuterium and oxygen-18 isotope composition of precipitation and atmospheric moisture. *Hydrological Processes*, *14*(8), 1341–1355. https://doi.org/10.1002/1099-1085(20000615)14:8<1341::AID-HYP983>3.0.CO;2-Z

Baek, S. H., & Lora, J. M. (2021). Counterbalancing influences of aerosols and greenhouse gases on atmospheric rivers. *Nature Climate Change*, *11*(11), Article 11. https://doi.org/10.1038/s41558-021-01166-8

Barth, N. A., Villarini, G., Nayak, M. A., & White, K. (2017). Mixed populations and annual flood frequency estimates in the western United States: The role of atmospheric rivers. *Water Resources Research*, *53*(1), 257–269. https://doi.org/10.1002/2016WR019064

B.C. Ministry of Forests. (2021). *Biogeoclimatic Ecosytem Classification Subzone/Variant Map for the Chilliwack Resource District, South Coast Region* [Map]. https://www.for.gov.bc.ca/ftp/HRE/external/!publish/becmaps/PaperMaps/field/DCK_ChilliwackResourceDistrict_SouthCoastRegion__field.pdf

Becker, E. J., & Tippett, M. K. (2024). Impact of ENSO and trends on the distribution of North American wintertime daily temperature. *Journal of Climate*, *1*(aop). https://doi.org/10.1175/JCLI-D-23-0569.1

Beguería, S., Latorre, B., Reig, F., & Vicente-Serrano, S. M. (2023). *Global SPEI Database* (2.8) [dataset]. https://spei.csic.es/database.html

Beguería, S., Vicente-Serrano, S. M., & Angulo-Martínez, M. (2010). A multi-scalar global drought data set: The SPEIbase: A new gridded product for the analysis of drought variability and impacts. *Bulletin of the American Meteorological Society*, *91*(10), 1351–1354.

Borkotoky, S. S., Williams, A. P., & Steinschneider, S. (2023). Six Hundred Years of Reconstructed Atmospheric River Activity Along the US West Coast. *Journal of Geophysical Research: Atmospheres*, *128*(12), e2022JD038321. https://doi.org/10.1029/2022JD038321

Brienen, R. J. W., Helle, G., Pons, T. L., Guyot, J.-L., & Gloor, M. (2012). Oxygen isotopes in tree rings are a good proxy for Amazon precipitation and El Niño-Southern Oscillation variability. *Proceedings of the National Academy of Sciences*, *109*(42), 16957–16962. https://doi.org/10.1073/pnas.1205977109

Brinkmann, N., Seeger, S., Weiler, M., Buchmann, N., Eugster, W., & Kahmen, A. (2018). Employing stable isotopes to determine the residence times of soil water and the temporal origin of water taken up by Fagus sylvatica and Picea abies in a temperate forest. *New Phytologist*, *219*(4), 1300–1313. https://doi.org/10.1111/nph.15255

Bronstert, A., Niehoff, D., & Schiffler, G. R. (2023). Modelling infiltration and infiltration excess: The importance of fast and local processes. *Hydrological Processes*, *37*(4), e14875. https://doi.org/10.1002/hyp.14875

Buenning, N. H., Stott, L., Yoshimura, K., & Berkelhammer, M. (2012). The cause of the seasonal variation in the oxygen isotopic composition of precipitation along the western U.S. coast. *Journal of Geophysical Research: Atmospheres*, *117*(D18). https://doi.org/10.1029/2012JD018050

Bunn, A. G. (2008). A dendrochronology program library in R (dplR). *Dendrochronologia*, *26*(2), 115–124. https://doi.org/10.1016/j.dendro.2008.01.002

Case, M. J., Johnson, B. G., Bartowitz, K. J., & Hudiburg, T. W. (2021). Forests of the future: Climate change impacts and implications for carbon storage in the Pacific Northwest, USA. *Forest Ecology and Management*, *482*, 118886. https://doi.org/10.1016/j.foreco.2020.118886

Chen, X., Leung, L. R., Gao, Y., Liu, Y., Wigmosta, M., & Richmond, M. (2018). Predictability of Extreme Precipitation in Western U.S. Watersheds Based on Atmospheric River Occurrence, Intensity, and Duration. *Geophysical Research Letters*, *45*(21), 11,693-11,701. https://doi.org/10.1029/2018GL079831

Chen, X., Leung, L. R., Wigmosta, M., & Richmond, M. (2019). Impact of Atmospheric Rivers on Surface Hydrological Processes in Western U.S. Watersheds. *Journal of Geophysical Research: Atmospheres*, *124*(16), 8896–8916. https://doi.org/10.1029/2019JD030468

Churakova (Sidorova), O. V., Porter, T. J., Zharkov, M. S., Fonti, M. V., Barinov, V. V., Taynik, A. V., Kirdyanov, A. V., Knorre, A. A., Wegmann, M., Trushkina, T. V., Koshurnikova, N. N., Vaganov, E. A., Myglan, V. S., Siegwolf, R. T. W., & Saurer, M. (2023). Climate impacts on tree-ring stable isotopes across the Northern Hemispheric boreal zone. *Science of The Total Environment*, *870*, 161644. https://doi.org/10.1016/j.scitotenv.2023.161644

Churakova Sidorova, O. V., Siegwolf, R. T. W., Fonti, M. V., Vaganov, E. A., & Saurer, M. (2021). Spring arctic oscillation as a trigger of summer drought in Siberian subarctic over the past 1494 years. *Scientific Reports*, *11*(1), Article 1. https://doi.org/10.1038/s41598-021-97911-2

CIMSS. (2024). *MIMIC-TPW*. https://tropic.ssec.wisc.edu/real-time/mimic-tpw/natl/main.html

Cook, E. R., & Kairiukstis, L. A. (1990). *Methods of Dendrochronology: Applications in the Environmental Sciences*. Kluwer Academic Publishers.

Cooper, A. E., Kirchner, J. W., Wolf, S., Lombardozzi, D. L., Sullivan, B. W., Tyler, S. W., & Harpold, A. A. (2020). Snowmelt causes different limitations on transpiration in a Sierra Nevada conifer forest. *Agricultural and Forest Meteorology*, *291*, 108089. https://doi.org/10.1016/j.agrformet.2020.108089

Corringham, T. W., Ralph, F. M., Gershunov, A., Cayan, D. R., & Talbot, C. A. (2019). Atmospheric rivers drive flood damages in the western United States. *Science Advances*, *5*(12), eaax4631. https://doi.org/10.1126/sciadv.aax4631

Coulthard, B., & Smith, D. J. (2016). A 477-year dendrohydrological assessment of drought severity for Tsable River, Vancouver Island, British Columbia, Canada. *Hydrological Processes*, *30*(11), 1676–1690. https://doi.org/10.1002/hyp.10726

Crawford, C. J., Griffin, D., & Kipfmueller, K. F. (2015). Capturing season-specific precipitation signals in the northern Rocky Mountains, USA, using earlywood and latewood tree rings. *Journal of Geophysical Research: Biogeosciences*, *120*(3), 428–440. https://doi.org/10.1002/2014JG002740

Csank, A. Z., Miller, A. E., Sherriff, R. L., Berg, E. E., & Welker, J. M. (2016). Tree-ring isotopes reveal drought sensitivity in trees killed by spruce beetle outbreaks in south-central Alaska. *Ecological Applications*, *26*(7), 2001–2020. https://doi.org/10.1002/eap.1365

Curry, C. L., & Sobie, S. R. (2023). *Climate Projections for the City of Vancouver: Highlights Report* (p. 29). Pacific Climate Impacts Consortium, University of Victoria.

https://www.pacificclimate.org/sites/default/files/publications/CityVan_rca_updated_120723.pdf

Cybis Dendrochronology. (2022). *CooRecorder* (9.8.1) [Computer software].

Dannenberg, M. P., & Wise, E. K. (2016). Seasonal climate signals from multiple tree ring metrics: A case study of Pinus ponderosa in the upper Columbia River Basin. *Journal of Geophysical Research: Biogeosciences*, *121*(4), 1178–1189. https://doi.org/10.1002/2015JG003155

Dansgaard, W. (1964). Stable isotopes in precipitation. *Tellus*, *16*(4), 436–468. https://doi.org/10.1111/j.2153-3490.1964.tb00181.x

D'Arrigo, R. D., Cook, E. R., Mann, M. E., & Jacoby, G. C. (2003). Tree-ring reconstructions of temperature and sea-level pressure variability associated with the warm-season Arctic Oscillation since AD 1650. *Geophysical Research Letters*, *30*(11). https://doi.org/10.1029/2003GL017250

Dettinger, M. (2004). *Fifty-two years of "Pineapple Express" storms across the west coast of North America*. U.S. Geological Survey, Scripps Institution of Oceanography. https://citeseerx.ist.psu.edu/document?repid=rep1&type=pdf&doi=bde074e11d46a8063dc0f5f66b13e594954ffe42

Dettinger, M. (2013). Atmospheric Rivers as Drought Busters on the U.S. West Coast. *Journal of Hydrometeorology*, *14*(6), 1721–1732. https://doi.org/10.1175/JHM-D-13-02.1

Dettinger, M., Ralph, F. M., Das, T., Neiman, P. J., & Cayan, D. R. (2011). Atmospheric Rivers, Floods and the Water Resources of California. *Water*, *3*(2), Article 2. https://doi.org/10.3390/w3020445

Di Lorenzo, E. (2023). *North Pacific Gyre Oscillation* [dataset]. http://www.o3d.org/npgo/

Di Lorenzo, E., Schneider, N., Cobb, K. M., Franks, P. J. S., Chhak, K., Miller, A. J., McWilliams, J. C., Bograd, S. J., Arango, H., Curchitser, E., Powell, T. M., & Rivière, P. (2008). North Pacific Gyre Oscillation links ocean climate and ecosystem change. *Geophysical Research Letters*, *35*(8). https://doi.org/10.1029/2007GL032838

Dierauer, J. R., Allen, D. M., & Whitfield, P. H. (2021). Climate change impacts on snow and streamflow drought regimes in four ecoregions of British Columbia. *Canadian Water Resources Journal / Revue Canadienne Des Ressources Hydriques*, *46*(4), 168–193. https://doi.org/10.1080/07011784.2021.1960894

Dinis, L., Bégin, C., Savard, M. M., Marion, J., Brigode, P., & Alvarez, C. (2019). Tree-ring stable isotopes for regional discharge reconstruction in eastern Labrador and teleconnection with the Arctic Oscillation. *Climate Dynamics*, *53*(5), 3625–3640. https://doi.org/10.1007/s00382-019-04731-2

Dong, Z., Zhou, F., Zheng, Z., & Fang, K. (2022). Increased amplitude of the North Pacific Gyre Oscillation towards recent: Evidence from tree-ring-based reconstruction since 1596. *International Journal of Climatology*, *42*(12), 6403–6412. https://doi.org/10.1002/joc.7596

Douville, H., Raghavan, K., Renwick, J., Allan, R. P., Arias, P. A., Barlow, M., Cerezo-Mota, R., Cherchi, A., Gan, T. Y., Gergis, J., Jiang, D., Khan, A., Mba, W. P., Rosenfeld, D., Tierney, J., & Zolina, O. (2021). *Water cycle changes* (pp. 1055–1210). Cambridge University Press. https://www.ipcc.ch/report/ar6/wg1/downloads/report/IPCC_AR6_WGI_Chapter08.pdf

ECCC. (2021). *Historical gridded snow water equivalent and snow cover fraction over Canada from remote sensing and land surface models* [dataset]. https://climate-scenarios.canada.ca/?page=blended-snow-data#refs

ECCC. (2023a, March 29). *Canadian Climate Normals 1981-2010 N VAN SEYMOUR HATCHERY*. https://climate.weather.gc.ca/climate_normals/results_1981_2010_e.html?searchType=stnProx&txtRadius=25&selCity=&selPark=&txtCentralLatDeg=&txtCentralLatMin=0&txtCentralLatSec=0&txtCentralLongDeg=&txtCentralLongMin=0&txtCentralLongSec=0&optProxType=decimal&txtLatDecDeg=49.3575&txtLongDecDeg=-123.1125&stnID=698&dispBack=0

ECCC. (2023b, March 29). *Canadian Climate Normals 1981-2010 N VANCOUVER CLEVELAND*. https://climate.weather.gc.ca/climate_normals/results_1981_2010_e.html?searchType=stnProx&txtRadius=25&selCity=&selPark=&txtCentralLatDeg=&txtCentralLatMin=0&txtCentralLatSec=0&txtCentralLongDeg=&txtCentralLongMin=0&txtCentralLongSec=0&optProxType=decimal&txtLatDecDeg=49.3575&txtLongDecDeg=-123.1125&stnID=680&dispBack=0

ECCC. (2023c, March 29). *Canadian Climate Normals 1981-2010 Station Data—HANEY UBC RF ADMIN*. https://climate.weather.gc.ca/climate_normals/results_1981_2010_e.html?searchType=stnName&txtStationName=haney&searchMethod=contains&txtCentralLatMin=0&txtCentralLatSec=0&txtCentralLongMin=0&txtCentralLongSec=0&stnID=776&dispBack=0

ECCC. (2023d, March 29). *Daily Data Report for April 2023—Abbotsford A*. https://climate.weather.gc.ca/climate_data/daily_data_e.html?hlyRange=2011-10-07%7C2023-04-16&dlyRange=2012-06-21%7C2023-04-

15&mlyRange=%7C&StationID=50308&Prov=BC&urlExtension=_e.html&searchType=stnName&optLimit=yearRange&StartYear=1840&EndYear=2023&selRowPerPage=25&Line=2&searchMethod=contains&Month=4&Day=16&txtStationName=abbotsford&timeframe=2&Year=2023

ECCC. (2023e, March 29). *Daily Data Report for April 2023—N Vancouver Wharves*. https://climate.weather.gc.ca/climate_data/daily_data_e.html?hlyRange=%7C&dlyRange=1962-03-01%7C2023-04-15&mlyRange=1962-01-01%7C2007-02-01&StationID=833&Prov=BC&urlExtension=_e.html&searchType=stnName&optLimit=yearRange&StartYear=1840&EndYear=2023&selRowPerPage=25&Line=0&searchMethod=contains&Month=4&Day=17&txtStationName=wharves&timeframe=2&Year=2023

ECCC. (2023f, March 29). *Daily Data Report for April 2023—VANCOUVER HARBOUR CS*. https://climate.weather.gc.ca/climate_data/daily_data_e.html?hlyRange=1976-01-20%7C2023-04-18&dlyRange=1925-11-01%7C2023-04-18&mlyRange=1925-01-01%7C2007-02-01&StationID=888&Prov=BC&urlExtension=_e.html&searchType=stnName&optLimit=yearRange&StartYear=1840&EndYear=2023&selRowPerPage=25&Line=55&searchMethod=contains&Month=4&Day=18&txtStationName=harbour&timeframe=2&Year=2023&time=LST

ECCC. (2023g, March 29). *Daily Data Report for January 2013—VANCOUVER INT'L A*. https://climate.weather.gc.ca/climate_data/daily_data_e.html?hlyRange=1953-01-01%7C2013-06-13&dlyRange=1937-01-01%7C2013-06-12&mlyRange=1937-01-01%7C2013-06-01&StationID=889&Prov=BC&urlExtension=_e.html&searchType=stnProx&optLimit=yearRange&StartYear=1840&EndYear=2023&selRowPerPage=25&Line=71&txtRadius=25&optProxType=city&selCity=49%7C17%7C123%7C8%7CVancouver&selPark=&txtCentralLatDeg=&txtCentralLatMin=0&txtCentralLatSec=0&txtCentralLongDeg=&txtCentralLongMin=0&txtCentralLongSec=0&txtLatDecDeg=&txtLongDecDeg=&timeframe=2&Day=17&Year=2013&Month=1#

ECCC. (2023h, March 29). *Daily Data Report for June 2012—Abbotsford A*. https://climate.weather.gc.ca/climate_data/daily_data_e.html?hlyRange=1953-01-01%7C2012-06-21&dlyRange=1944-10-01%7C2012-06-20&mlyRange=1944-01-01%7C2012-06-01&StationID=702&Prov=BC&urlExtension=_e.html&searchType=stnName&optLimit=yearRange&StartYear=1840&EndYear=2023&selRowPerPage=25&Line=3&searchMethod=contains&Month=6&Day=16&txtStationName=abbotsford&timeframe=2&Year=2012

ECCC. (2023i, March 29). *Daily Data Report for March 2014—Pitt Meadows CS*. https://climate.weather.gc.ca/climate_data/daily_data_e.html?hlyRange=1994-02-01%7C2023-04-17&dlyRange=1993-10-01%7C2023-04-17&mlyRange=1993-01-01%7C2007-02-01&StationID=6830&Prov=BC&urlExtension=_e.html&searchType=stnProx&optLimit=specDate&Month=3&Day=17&StartYear=2014&EndYear=2014&Year=2014&selRowPerPage=25&Line=0&txtRadius=25&optProxType=navLink&txtLatDecDeg=49.264472222222&txtLongDecDeg=-122.57316666667&timeframe=2&time=LST

ECCC. (2024, March 27). *Canadian Climate Normals 1981-2010 N VANC GROUSE MTN RESORT*. https://climate.weather.gc.ca/climate_normals/results_1981_2010_e.html?searchType=stnProx&txtRadius=25&optProxType=city&selCity=49%7C17%7C123%7C8%7CVancouver&selPark=&txtCentralLatDeg=&txtCentralLatMin=0&txtCentralLatSec=0&txtCentralLongDeg=&txtCentralLongMin=0&txtCentralLongSec=0&txtLatDecDeg=&txtLongDecDeg=&stnID=823&dispBack=0

ECCC, C. (2023j, March 29). *Daily Data Report for March 2023—Haney UBC RF Admin*. https://climate.weather.gc.ca/climate_data/daily_data_e.html?hlyRange=%7C&dlyRange=1961-10-01%7C2023-03-14&mlyRange=1961-01-01%7C2007-02-01&StationID=776&Prov=BC&urlExtension=_e.html&searchType=stnName&optLimit=yearRange&StartYear=1840&EndYear=2023&selRowPerPage=25&Line=5&searchMethod=contains&Month=3&Day=27&txtStationName=haney&timeframe=2&Year=2023

Eldardiry, H., Mahmood, A., Chen, X., Hossain, F., Nijssen, B., & Lettenmaier, D. P. (2019). Atmospheric River–Induced Precipitation and Snowpack during the Western United States Cold Season. *Journal of Hydrometeorology*, *20*(4), 613–630. https://doi.org/10.1175/JHM-D-18-0228.1

ESRL/NOAA. (2023). *Nino 3.4, 1870-present based on HadISST* [dataset]. https://climatedataguide.ucar.edu/climate-data/nino-sst-indices-nino-12-3-34-4-oni-and-tni

Federal Columbia River Power System, Bonneville Power Administration, U.S. Bureau of Reclamation, & U.S. Army Corps of Engineers. (2001). *The Columbia River System Inside Story*. https://www.bpa.gov/-/media/Aep/power/hydropower-data-studies/columbia_river_inside_story.pdf

Foroozan, Z., Grießinger, J., Pourtahmasi, K., & Bräuning, A. (2019). Evaluation of Different Pooling Methods to Establish a Multi-Century δ18O

Chronology for Paleoclimate Reconstruction. *Geosciences*, *9*(6), Article 6. https://doi.org/10.3390/geosciences9060270

Foroozan, Z., Grießinger, J., Pourtahmasi, K., & Bräuning, A. (2020). 501 Years of Spring Precipitation History for the Semi-Arid Northern Iran Derived from Tree-Ring δ18O Data. *Atmosphere*, *11*(9), Article 9. https://doi.org/10.3390/atmos11090889

Gat, J. R. (1996). Oxygen and Hydrogen Isotopes in the Hydrologic Cycle. *Annual Review of Earth and Planetary Sciences*, *24*(1), 225–262. https://doi.org/10.1146/annurev.earth.24.1.225

Gershunov, A., Shulgina, T., Ralph, F. M., Lavers, D. A., & Rutz, J. J. (2017). Assessing the climate-scale variability of atmospheric rivers affecting western North America. *Geophysical Research Letters*, *44*(15), 7900–7908. https://doi.org/10.1002/2017GL074175

Gillett, N. P., Cannon, A. J., Malinina, E., Schnorbus, M., Anslow, F., Sun, Q., Kirchmeier-Young, M., Zwiers, F., Seiler, C., Zhang, X., Flato, G., Wan, H., Li, G., & Castellan, A. (2022). Human influence on the 2021 British Columbia floods. *Weather and Climate Extremes*, *36*, 100441. https://doi.org/10.1016/j.wace.2022.100441

Gimbel, K. F., Puhlmann, H., & Weiler, M. (2016). Does drought alter hydrological functions in forest soils? *Hydrology and Earth System Sciences*, *20*(3), 1301–1317. https://doi.org/10.5194/hess-20-1301-2016

Goldenson, N., Leung, L. R., Bitz, C. M., & Blanchard-Wrigglesworth, E. (2018). Influence of Atmospheric Rivers on Mountain Snowpack in the Western United States. *Journal of Climate*, *31*(24), 9921–9940. https://doi.org/10.1175/JCLI-D-18-0268.1

Gonzales, K. R., Swain, D. L., Nardi, K. M., Barnes, E. A., & Diffenbaugh, N. S. (2019). Recent Warming of Landfalling Atmospheric Rivers Along the West Coast of the United States. *Journal of Geophysical Research: Atmospheres*, *124*(13), 6810–6826. https://doi.org/10.1029/2018JD029860

Gonzales, K. R., Swain, D. L., Roop, H. A., & Diffenbaugh, N. S. (2022). Quantifying the Relationship Between Atmospheric River Origin Conditions and Landfall Temperature. *Journal of Geophysical Research: Atmospheres*, *127*(20), e2022JD037284. https://doi.org/10.1029/2022JD037284

Grantz, D. A. (1990). Plant response to atmospheric humidity. *Plant, Cell & Environment*, *13*(7), 667–679. https://doi.org/10.1111/j.1365-3040.1990.tb01082.x

Greenblat, A. T., Allen, D. M., & Hahm, W. J. (2024). Characterizing Isotopic Composition and Trajectories of Atmospheric River Events. *Atmosphere*, *15*(1), 74. https://doi.org/10.3390/atmos15010074

Grissino-Mayer, H. D. (2001). *Evaluating Crossdating Accuracy: A Manual and Tutorial for the Computer Program COFECHA*. https://repository.arizona.edu/handle/10150/251654

Guan, B., Molotch, N. P., Waliser, D. E., Fetzer, E. J., & Neiman, P. J. (2013). The 2010/2011 snow season in California's Sierra Nevada: Role of atmospheric rivers and modes of large-scale variability. *Water Resources Research*, *49*(10), 6731–6743. https://doi.org/10.1002/wrcr.20537

Guan, B., & Waliser, D. E. (2015). Detection of atmospheric rivers: Evaluation and application of an algorithm for global studies. *Journal of Geophysical Research: Atmospheres*, *120*(24), 12514–12535. https://doi.org/10.1002/2015JD024257

Guan, B., Waliser, D. E., Molotch, N. P., Fetzer, E. J., & Neiman, P. J. (2012). Does the Madden–Julian Oscillation Influence Wintertime Atmospheric Rivers and Snowpack in the Sierra Nevada? *Monthly Weather Review*, *140*(2), 325–342. https://doi.org/10.1175/MWR-D-11-00087.1

Guan, B., Waliser, D. E., Ralph, F. M., Fetzer, E. J., & Neiman, P. J. (2016). Hydrometeorological characteristics of rain-on-snow events associated with atmospheric rivers. *Geophysical Research Letters*, *43*(6), 2964–2973. https://doi.org/10.1002/2016GL067978

Gupta, R. S., Steinschneider, S., & Reed, P. M. (2023). A multi-objective paleo-informed reconstruction of western US weather regimes over the past 600 years. *Climate Dynamics*, *60*(1), 339–358. https://doi.org/10.1007/s00382-022-06302-4

Hagos, S. M., Leung, L. R., Yoon, J.-H., Lu, J., & Gao, Y. (2016). A projection of changes in landfalling atmospheric river frequency and extreme precipitation over western North America from the Large Ensemble CESM simulations. *Geophysical Research Letters*, *43*(3), 1357–1363. https://doi.org/10.1002/2015GL067392

Hamlet, A. F. (2011). Assessing water resources adaptive capacity to climate change impacts in the Pacific Northwest Region of North America. *Hydrology and Earth System Sciences*, *15*(5), 1427–1443. https://doi.org/10.5194/hess-15-1427-2011

Harley, G. L., Maxwell, R. S., Black, B. A., & Bekker, M. F. (2020). A multi-century, tree-ring-derived perspective of the North Cascades (USA) 2014–2016 snow drought. *Climatic Change*, *162*(1), 127–143. https://doi.org/10.1007/s10584-020-02719-0

He, S. (2004, December 3). *Generalized Additive Models for Data With Concurvity: Statistical Issues and a Novel Model Fitting Approach* [University of Pittsburgh ETD]. University of Pittsburgh. http://d-scholarship.pitt.edu/9944/

Held, I. M., & Soden, B. J. (2006). Robust Responses of the Hydrological Cycle to Global Warming. *Journal of Climate*, *19*(21), 5686–5699. https://doi.org/10.1175/JCLI3990.1

Henn, B., Weihs, R., Martin, A. C., Ralph, F. M., & Osborne, T. (2020). Skill of Rain–Snow Level Forecasts for Landfalling Atmospheric Rivers: A Multimodel Assessment Using California's Network of Vertically Profiling Radars. *Journal of Hydrometeorology*, *21*(4), 751–771. https://doi.org/10.1175/JHM-D-18-0212.1

Holmes, R. L. (1983). Computer-assisted quality control in tree-ring dating and measurement. *Tree-Ring Bulletin*, *43*, 69–78.

Howard, I. M., Stahle, D. W., Dettinger, M. D., Poulsen, C., Ralph, F. M., Torbenson, M. C. A., & Gershunov, A. (2023). A 440-Year Reconstruction of Heavy Precipitation in California from Blue Oak Tree Rings. *Journal of Hydrometeorology*, *24*(3), 463–477. https://doi.org/10.1175/JHM-D-22-0062.1

Hu, J. M., & Nolin, A. W. (2019). Snowpack Contributions and Temperature Characterization of Landfalling Atmospheric Rivers in the Western Cordillera of the United States. *Geophysical Research Letters*, *46*(12), 6663–6672. https://doi.org/10.1029/2019GL083564

Hudson, C. L., English, N. B., Lloyd, A. H., Mann, D. H., & Pendall, E. (2015). *Interior Alaska 19 Year Tree Ring Stable Isotope Data* [dataset]. https://www.ncei.noaa.gov/pub/data/paleo/treering/isotope/northamerica/usa/alaska/alces2015iso.txt

Hunter, S. C., Allen, D. M., & Kohfeld, K. E. (2020). Comparing Approaches for Reconstructing Groundwater Levels in the Mountainous Regions of Interior British Columbia, Canada, Using Tree Ring Widths. *Atmosphere*, *11*(12), Article 12. https://doi.org/10.3390/atmos11121374

Intergovernmental Panel on Climate Change. (2022). *Climate Change 2022: Impacts, Adaptation and Vulnerability* (Contribution of Working Group II to the Sixth Assessment Report of the Intergovernmental Panel on Climate Change, p. 3056). Cambridge University Press. doi:10.1017/9781009325844

Katzie First Nation. (2024). *Who We Are | Katzie First Nation*. https://katzie.ca/who-we-are/

Kirdyanov, A., Hughes, M., Vaganov, E., Schweingruber, F., & Silkin, P. (2003). The importance of early summer temperature and date of snow melt for tree growth in the Siberian Subarctic. *Trees*, *17*(1), 61–69. https://doi.org/10.1007/s00468-002-0209-z

Klinka, K., Worrall, J., Skoda, L., Varga, P., & Chourmouzis, C. (1999). *The distribution and synopsis of ecological and silvical characteristics of tree species of British Columbia's forests*. Forest Sciences Department, University of British Columbia. https://doi.org/10.14288/1.0107280

Kovács, L. (2022). Feature selection algorithms in generalized additive models under concurvity. *Computational Statistics*. https://doi.org/10.1007/s00180-022-01292-7

Kwon, H.-H., & Lall, U. (2016). A copula-based nonstationary frequency analysis for the 2012–2015 drought in California. *Water Resources Research*, *52*(7), 5662–5675. https://doi.org/10.1002/2016WR018959

Labotka, D. M., Grissino-Mayer, H. D., Mora, C. I., & Johnson, E. J. (2016). Patterns of moisture source and climate variability in the southeastern United States: A four-century seasonally resolved tree-ring oxygen-isotope record. *Climate Dynamics*, *46*(7), 2145–2154. https://doi.org/10.1007/s00382-015-2694-y

Labuhn, I., Daux, V., Girardclos, O., Stievenard, M., Pierre, M., & Masson-Delmotte, V. (2016). French summer droughts since 1326 CE: A reconstruction based on tree ring cellulose $\delta^{18}O$. *Climate of the Past*, *12*(5), 1101–1117. https://doi.org/10.5194/cp-12-1101-2016

Labuhn, I., Daux, V., Pierre, M., Stievenard, M., Girardclos, O., Féron, A., Genty, D., Masson-Delmotte, V., & Mestre, O. (2014). Tree age, site and climate controls on tree ring cellulose δ18O: A case study on oak trees from south-western France. *Dendrochronologia*, *32*(1), 78–89. https://doi.org/10.1016/j.dendro.2013.11.001

Larocque, S. J., & Smith, D. J. (2005). A dendroclimatological reconstruction of climate since AD 1700 in the Mt. Waddington area, British Columbia Coast Mountains, Canada. *Dendrochronologia*, *22*(2), 93–106. https://doi.org/10.1016/j.dendro.2005.02.003

Lavers, D. A., Allan, R. P., Wood, E. F., Villarini, G., Brayshaw, D. J., & Wade, A. J. (2011). Winter floods in Britain are connected to atmospheric rivers. *Geophysical Research Letters*, *38*(23). https://doi.org/10.1029/2011GL049783

Leach, J. A., & Moore, R. D. (2014). Winter stream temperature in the rain-on-snow zone of the Pacific Northwest: Influences of hillslope runoff and

transient snow cover. *Hydrology and Earth System Sciences*, *18*(2), 819–838. https://doi.org/10.5194/hess-18-819-2014

Leavitt, S. W. (2010). Tree-ring C–H–O isotope variability and sampling. *Science of The Total Environment*, *408*(22), 5244–5253. https://doi.org/10.1016/j.scitotenv.2010.07.057

Leavitt, S. W., & Danzer, S. R. (1993). Method for batch processing small wood samples to holocellulose for stable-carbon isotope analysis. *Analytical Chemistry*, *65*(1), 87–89. https://doi.org/10.1021/ac00049a017

Lee, S.-K., Mapes, B. E., Wang, C., Enfield, D. B., & Weaver, S. J. (2014). Springtime ENSO phase evolution and its relation to rainfall in the continental U.S. *Geophysical Research Letters*, *41*(5), 1673–1680. https://doi.org/10.1002/2013GL059137

LeGrande, A. N., & Schmidt, G. A. (2006). Global gridded data set of the oxygen isotopic composition in seawater. *Geophysical Research Letters*, *33*(12). https://doi.org/10.1029/2006GL026011

Leonelli, G., Battipaglia, G., Cherubini, P., Saurer, M., Siegwolf, R. T. W., Maugeri, M., Stenni, B., Fusco, S., Maggi, V., & Pelfini, M. (2017). *Larix decidua* δ18O tree-ring cellulose mainly reflects the isotopic signature of winter snow in a high-altitude glacial valley of the European Alps. *Science of The Total Environment*, *579*, 230–237. https://doi.org/10.1016/j.scitotenv.2016.11.129

Li, D., Lettenmaier, D. P., Margulis, S. A., & Andreadis, K. (2019). The Role of Rain-on-Snow in Flooding Over the Conterminous United States. *Water Resources Research*, *55*(11), 8492–8513. https://doi.org/10.1029/2019WR024950

Lin, I.-I., Camargo, S. J., Patricola, C. M., Boucharel, J., Chand, S., Klotzbach, P., Chan, J. C. L., Wang, B., Chang, P., Li, T., & Jin, F.-F. (2020). ENSO and Tropical Cyclones. In *El Niño Southern Oscillation in a Changing Climate* (pp. 377–408). American Geophysical Union (AGU). https://doi.org/10.1002/9781119548164.ch17

Liner, S., Ryoo, J.-M., & Chiao, S. (2022). On the Relationship of Arctic Oscillation with Atmospheric Rivers and Snowpack in the Western United States Using Long-Term Multi-Platform Dataset. *Water*, *14*(15), Article 15. https://doi.org/10.3390/w14152392

Littell, J. S., Pederson, G. T., Gray, S. T., Tjoelker, M., Hamlet, A. F., & Woodhouse, C. A. (2016). Reconstructions of Columbia River Streamflow from Tree-Ring Chronologies in the Pacific Northwest, USA. *JAWRA Journal of the American Water Resources Association*, *52*(5), 1121–1141. https://doi.org/10.1111/1752-1688.12442

Liu, X., Ren, X., & Yang, X.-Q. (2016). Decadal Changes in Multiscale Water Vapor Transport and Atmospheric River Associated with the Pacific Decadal Oscillation and the North Pacific Gyre Oscillation. *Journal of Hydrometeorology*, *17*(1), 273–285. https://doi.org/10.1175/JHM-D-14-0195.1

Liu, Y., Wang, Y., Li, Q., Song, H., Zhang, Y., Yuan, Z., & Wang, Z. (2015). A tree-ring-based June–September mean relative humidity reconstruction since 1837 from the Yiwulü Mountain region, China. *International Journal of Climatology*, *35*(7), 1301–1308. https://doi.org/10.1002/joc.4057

Liu, Z., Tang, Y., Jian, Z., Poulsen, C. J., Welker, J. M., & Bowen, G. J. (2017). Pacific North American circulation pattern links external forcing and North American hydroclimatic change over the past millennium. *Proceedings of the National Academy of Sciences*, *114*(13), 3340–3345. https://doi.org/10.1073/pnas.1618201114

Ljungqvist, F. C., Piermattei, A., Seim, A., Krusic, P. J., Büntgen, U., He, M., Kirdyanov, A. V., Luterbacher, J., Schneider, L., Seftigen, K., Stahle, D. W., Villalba, R., Yang, B., & Esper, J. (2020). Ranking of tree-ring based hydroclimate reconstructions of the past millennium. *Quaternary Science Reviews*, *230*, 106074. https://doi.org/10.1016/j.quascirev.2019.106074

Loader, N. J., Robertson, I., Barker, A. C., Switsur, V. R., & Waterhouse, J. S. (1997). An improved technique for the batch processing of small wholewood samples to α-cellulose. *Chemical Geology*, *136*(3), 313–317. https://doi.org/10.1016/S0009-2541(96)00133-7

Lyu, L., Büntgen, U., Treydte, K., Yu, K., Liang, H., Reinig, F., Nievergelt, D., Li, M.-H., & Cherubini, P. (2019). Tree rings reveal hydroclimatic fingerprints of the Pacific Decadal Oscillation on the Tibetan Plateau. *Climate Dynamics*, *53*(1), 1023–1037. https://doi.org/10.1007/s00382-019-04629-z

Malcolm Knapp Research Forest. (n.d.). *History*. Malcolm Knapp Research Forest. Retrieved January 14, 2024, from https://www.mkrf.forestry.ubc.ca/about/history/

Mantua, N. J., & Hare, S. R. (2002). The Pacific Decadal Oscillation. *Journal of Oceanography*, *58*(1), 35–44. https://doi.org/10.1023/A:1015820616384

Marra, G., & Wood, S. N. (2011). Practical variable selection for generalized additive models. *Computational Statistics & Data Analysis*, *55*(7), 2372–2387. https://doi.org/10.1016/j.csda.2011.02.004

Martinez, L. (1996). *Useful Tree Species for Tree-Ring Dating*. https://www.ltrr.arizona.edu/lorim/good.html

Mass, C., Randall, C., Conrick, R., & Ovens, D. (2022). The Relationship between Northeast Pacific Sea Surface Temperatures, Synoptic Evolution, and Surface Air Temperatures over the Pacific Northwest. *Weather and Forecasting*, *37*(10), 1741–1759. https://doi.org/10.1175/WAF-D-22-0069.1

Maxwell, J. T., Harley, G. L., & Rahman, A. F. (2018). Annual Growth Rings in Two Mangrove Species from the Sundarbans, Bangladesh Demonstrate Linkages to Sea-Level Rise and Broad-Scale Ocean-Atmosphere Variability. *Wetlands*, *38*(6), 1159–1170. https://doi.org/10.1007/s13157-018-1079-5

McCabe-Glynn, S., Johnson, K. R., Strong, C., Zou, Y., Yu, J.-Y., Sellars, S., & Welker, J. M. (2016). Isotopic signature of extreme precipitation events in the western U.S. and associated phases of Arctic and tropical climate modes. *Journal of Geophysical Research: Atmospheres*, *121*(15), 8913–8924. https://doi.org/10.1002/2016JD025524

McCarroll, D., & Loader, N. J. (2004a). Stable isotopes in tree rings. *Quaternary Science Reviews*, *23*(7), 771–801. https://doi.org/10.1016/j.quascirev.2003.06.017

McCarroll, D., & Loader, N. J. (2004b). Stable isotopes in tree rings. *Quaternary Science Reviews*, *23*(7), 771–801. https://doi.org/10.1016/j.quascirev.2003.06.017

McCune, Z. (2018). *Douglas fir*. https://thenounproject.com/icon/douglas-fir-2114485/

McPhaden, M. J., Lee, T., Fournier, S., & Balmaseda, M. A. (2020). ENSO Observations. In *El Niño Southern Oscillation in a Changing Climate* (pp. 39–63). American Geophysical Union (AGU). https://doi.org/10.1002/9781119548164.ch3

Meidinger, D. V., & Pojar, J. (1991). *Ecosystems of British Columbia*. BC Ministry of Forests.

Meko, D. M., & Woodhouse, C. A. (2011). Application of Streamflow Reconstruction to Water Resources Management. In M. K. Hughes, T. W. Swetnam, & H. F. Diaz (Eds.), *Dendroclimatology: Progress and Prospects* (pp. 231–261). Springer Netherlands. https://doi.org/10.1007/978-1-4020-5725-0_8

Mellander, P.-E., Bishop, K., & Lundmark, T. (2004). The influence of soil temperature on transpiration: A plot scale manipulation in a young Scots pine stand. *Forest Ecology and Management*, *195*(1), 15–28. https://doi.org/10.1016/j.foreco.2004.02.051

Metro Vancouver. (2019a). *Climate 2050 Strategic Framework* (p. 40). http://www.metrovancouver.org/services/air-quality/AirQualityPublications/AQ_C2050-StrategicFramework.pdf

Metro Vancouver. (2019b). *Water Supply Outlook 2120*. Metro Vancouver. http://www.metrovancouver.org/services/water/WaterPublications/WaterSupplyOutlook2120.pdf

Miller, D. L., Mora, C. I., Grissino-Mayer, H. D., Mock, C. J., Uhle, M. E., & Sharp, Z. (2006). Tree-ring isotope records of tropical cyclone activity. *Proceedings of the National Academy of Sciences*, *103*(39), 14294–14297. https://doi.org/10.1073/pnas.0606549103

Miralles, D. G., van den Berg, M. J., Gash, J. H., Parinussa, R. M., de Jeu, R. A. M., Beck, H. E., Holmes, T. R. H., Jiménez, C., Verhoest, N. E. C., Dorigo, W. A., Teuling, A. J., & Johannes Dolman, A. (2014). El Niño–La Niña cycle and recent trends in continental evaporation. *Nature Climate Change*, *4*(2), 122–126. https://doi.org/10.1038/nclimate2068

Mood, B. J., Coulthard, B., & Smith, D. J. (2020). Three hundred years of snowpack variability in southwestern British Columbia reconstructed from tree-rings. *Hydrological Processes*, *34*(25), 5123–5133. https://doi.org/10.1002/hyp.13933

Mood, B. J., & Smith, D. J. (2021). A multi-century July-August streamflow reconstruction of Metro Vancouver's water supply contribution from the Capilano and Seymour watersheds in southwestern British Columbia, Canada. *Canadian Water Resources Journal / Revue Canadienne Des Ressources Hydriques*, *46*(3), 121–138. https://doi.org/10.1080/07011784.2021.1931458

Mote, P. W., & Salathé, E. P. (2010). Future climate in the Pacific Northwest. *Climatic Change*, *102*(1), 29–50. https://doi.org/10.1007/s10584-010-9848-z

Mundhenk, B. D., Barnes, E. A., & Maloney, E. D. (2016). All-Season Climatology and Variability of Atmospheric River Frequencies over the North Pacific. *Journal of Climate*, *29*(13), 4885–4903. https://doi.org/10.1175/JCLI-D-15-0655.1

Musqueam Indian Band. (2024). Musqueam Territory. *Musqueam*. https://www.musqueam.bc.ca/our-story/our-territory/

Nagavciuc, V., Ionita, M., Kern, Z., McCarroll, D., & Popa, I. (2022). A ~700 years perspective on the 21st century drying in the eastern part of Europe based on δ18O in tree ring cellulose. *Communications Earth & Environment*, *3*(1), Article 1. https://doi.org/10.1038/s43247-022-00605-4

Najibi, N., & Steinschneider, S. (2023). Extreme Precipitation-Temperature Scaling in California: The Role of Atmospheric Rivers. *Geophysical Research Letters*, *50*(14), e2023GL104606. https://doi.org/10.1029/2023GL104606

Nakatsuka, T., Sano, M., Li, Z., Xu, C., Tsushima, A., Shigeoka, Y., Sho, K., Ohnishi, K., Sakamoto, M., Ozaki, H., Higami, N., Nakao, N., Yokoyama, M., & Mitsutani, T. (2020). A 2600-year summer climate reconstruction in central Japan by integrating tree-ring stable oxygen and hydrogen isotopes. *Climate of the Past*, *16*(6), 2153–2172. https://doi.org/10.5194/cp-16-2153-2020

Nalley, D., Adamowski, J., Biswas, A., Gharabaghi, B., & Hu, W. (2019). A multiscale and multivariate analysis of precipitation and streamflow variability in relation to ENSO, NAO and PDO. *Journal of Hydrology*, *574*, 288–307. https://doi.org/10.1016/j.jhydrol.2019.04.024

National Weather Service Climate Prediction Center. (2023a). *Arctic Oscillation (AO)* [dataset]. https://www.cpc.ncep.noaa.gov/products/precip/CWlink/daily_ao_index/ao.shtml

National Weather Service Climate Prediction Center. (2023b). *Monitoring Weather & Climate—Pentad MJO Indices* [dataset]. https://www.cpc.ncep.noaa.gov/products/precip/CWlink/daily_mjo_index/pentad.shtml

National Weather Service Climate Prediction Center. (2023c). *Pacific/North American Pattern* [dataset]. https://www.cpc.ncep.noaa.gov/products/precip/CWlink/pna/pna.shtml

Neiman, P. J., Schick, L. J., Ralph, F. M., Hughes, M., & Wick, G. A. (2011). Flooding in Western Washington: The Connection to Atmospheric Rivers. *Journal of Hydrometeorology*, *12*(6), 1337–1358. https://doi.org/10.1175/2011JHM1358.1

Nemani, R. R., Keeling, C. D., Hashimoto, H., Jolly, W. M., Piper, S. C., Tucker, C. J., Myneni, R. B., & Running, S. W. (2003). Climate-Driven Increases in Global Terrestrial Net Primary Production from 1982 to 1999. *Science*, *300*(5625), 1560–1563. https://doi.org/10.1126/science.1082750

Nicklen, E. F., Roland, C. A., Csank, A. Z., Wilmking, M., Ruess, R. W., & Muldoon, L. A. (2019). Stand basal area and solar radiation amplify white spruce climate sensitivity in interior Alaska: Evidence from carbon isotopes and tree rings. *Global Change Biology*, *25*(3), 911–926. https://doi.org/10.1111/gcb.14511

NOAA. (2023). *NCEI PDO Index* [dataset]. https://www.ncei.noaa.gov/access/monitoring/pdo/

NOAA. (2024a). *NCEP-NCAR Reanalysis 1 Total Cloud Cover* [dataset]. https://psl.noaa.gov/mddb2/makePlot.html?variableID=158861

NOAA. (2024b). *NCEP-NCAR Reanalysis 1 weasd (Water Equiv. Of Accum. Snow Depth)* [dataset]. https://psl.noaa.gov/mddb2/makePlot.html?variableID=158891

NOAA. (2024c). *Tree Ring*. https://www.ncei.noaa.gov/products/paleoclimatology/tree-ring

NOAA PSL. (2023). *El Niño Southern Oscillation (ENSO)*. https://psl.noaa.gov/enso/

Odon, P., West, G., & Stull, R. (2019). Evaluation of Reanalyses over British Columbia. Part II: Daily and Extreme Precipitation. *Journal of Applied Meteorology and Climatology*, *58*(2), 291–315. https://doi.org/10.1175/JAMC-D-18-0188.1

Oster, J. L., Montañez, I. P., & Kelley, N. P. (2012). Response of a modern cave system to large seasonal precipitation variability. *Geochimica et Cosmochimica Acta*, *91*, 92–108. https://doi.org/10.1016/j.gca.2012.05.027

Pathak, P., Kalra, A., Lamb, K. W., Miller, W. P., Ahmad, S., Amerineni, R., & Ponugoti, D. P. (2018). Climatic variability of the Pacific and Atlantic Oceans and western US snowpack. *International Journal of Climatology*, *38*(3), 1257–1269. https://doi.org/10.1002/joc.5241

Patskoski, J., & Sankarasubramanian, A. (2015). Improved reservoir sizing utilizing observed and reconstructed streamflows within a Bayesian combination framework. *Water Resources Research*, *51*(7), 5677–5697. https://doi.org/10.1002/2014WR016189

Payne, A. E., Demory, M.-E., Leung, L. R., Ramos, A. M., Shields, C. A., Rutz, J. J., Siler, N., Villarini, G., Hall, A., & Ralph, F. M. (2020). Responses and impacts of atmospheric rivers to climate change. *Nature Reviews Earth & Environment*, *1*(3), Article 3. https://doi.org/10.1038/s43017-020-0030-5

Payne, A. E., & Magnusdottir, G. (2014). Dynamics of Landfalling Atmospheric Rivers over the North Pacific in 30 Years of MERRA Reanalysis. *Journal of Climate*, *27*(18), 7133–7150. https://doi.org/10.1175/JCLI-D-14-00034.1

Peel, M., Finlayson, B., & Mcmahon, T. (2007). Updated World Map of the Koppen-Geiger Climate Classification. *Hydrology and Earth System Sciences Discussions*, *4*. https://doi.org/10.5194/hess-11-1633-2007

Pike, R. G., Redding, T. E., Moore, R. D., Winkler, R. D., & Bladon, K. D. (2011). *Compendium of forest hydrology and geomorphology in British Columbia*. B.C. Ministry of Forests and Range, Forest Science Program. https://www.cabidigitallibrary.org/doi/full/10.5555/20113007393

Pitman, K. J., & Smith, D. J. (2012). Tree-ring derived Little Ice Age temperature trends from the central British Columbia Coast Mountains, Canada. *Quaternary Research*, *78*(3), 417–426. https://doi.org/10.1016/j.yqres.2012.08.009

Porter, T. J., Pisaric, M. F. J., Field, R. D., Kokelj, S. V., Edwards, T. W. D., deMontigny, P., Healy, R., & LeGrande, A. N. (2014). Spring-summer temperatures since AD 1780 reconstructed from stable oxygen isotope ratios in white spruce tree-rings from the Mackenzie Delta, northwestern Canada. *Climate Dynamics*, *42*(3), 771–785. https://doi.org/10.1007/s00382-013-1674-3

PRISM. (2024). *PRISM Climate Group at Oregon State University*. Northwest Alliance for Computational Science & Engineering. https://www.prism.oregonstate.edu/normals/

Province of British Columbia. (2018). *British Columbia Soil Information Finder Tool* [dataset]. https://governmentofbc.maps.arcgis.com/apps/MapSeries/index.html?appid=cc25e43525c5471ca7b13d639bbcd7aa

Province of British Columbia. (2024, January 25). *Amabilis fir*. Province of British Columbia. https://www2.gov.bc.ca/gov/content/industry/forestry/managing-our-forest-resources/silviculture/tree-species-selection/tree-species-compendium-index/amabilis-fir#geo

Qin, L., Bolatov, K., Shang, H., Yu, S., Gou, X., Bagila, M., Bolatova, A., Ainur, U., & Zhang, R. (2022). Reconstruction of alpine snowfall in southern Kazakhstan based on oxygen isotopes in tree rings. *Theoretical and Applied Climatology*, *148*(1), 727–737. https://doi.org/10.1007/s00704-022-03974-0

R Core Team. (2022). *R: A language and environemnt for statisitcal computing.* [Computer software]. R Foundation for Statistical Computing. https://www.R-project.org/

Radić, V., Cannon, A. J., Menounos, B., & Gi, N. (2015). Future changes in autumn atmospheric river events in British Columbia, Canada, as projected by CMIP5 global climate models. *Journal of Geophysical Research: Atmospheres*, *120*(18), 9279–9302. https://doi.org/10.1002/2015JD023279

Ralph, F. M., & Dettinger, M. D. (2011). Storms, floods, and the science of atmospheric rivers. *Eos, Transactions American Geophysical Union*, *92*(32), 265–266. https://doi.org/10.1029/2011EO320001

Ralph, F. M., Dettinger, M. D., Cairns, M. M., Galarneau, T. J., & Eylander, J. (2018). Defining “Atmospheric River”: How the Glossary of Meteorology Helped Resolve a Debate. *Bulletin of the American Meteorological Society*, *99*(4), 837–839. https://doi.org/10.1175/BAMS-D-17-0157.1

Ralph, F. M., Dettinger, M., Lavers, D., Gorodetskaya, I. V., Martin, A., Viale, M., White, A. B., Oakley, N., Rutz, J., Spackman, J. R., Wernli, H., & Cordeira, J. (2017). Atmospheric Rivers Emerge as a Global Science and Applications Focus. *Bulletin of the American Meteorological Society*, *98*(9), 1969–1973. https://doi.org/10.1175/BAMS-D-16-0262.1

Ralph, F. M., Neiman, P. J., & Wick, G. A. (2004). Satellite and CALJET Aircraft Observations of Atmospheric Rivers over the Eastern North Pacific Ocean during the Winter of 1997/98. *Monthly Weather Review*, *132*(7), 1721–1745. https://doi.org/10.1175/1520-0493(2004)132<1721:SACAOO>2.0.CO;2

Ralph, F. M., Rutz, J. J., Cordeira, J. M., Dettinger, M., Anderson, M., Reynolds, D., Schick, L. J., & Smallcomb, C. (2019). A Scale to Characterize the Strength and Impacts of Atmospheric Rivers. *Bulletin of the American Meteorological Society*, *100*(2), 269–289. https://doi.org/10.1175/BAMS-D-18-0023.1

Ramos, A. M., Trigo, R. M., Tomé, R., & Liberato, M. L. R. (2018). Impacts of Atmospheric Rivers in Extreme Precipitation on the European Macaronesian Islands. *Atmosphere*, *9*(8), Article 8. https://doi.org/10.3390/atmos9080325

Ratcliff, C. J., Voelker, S. L., & Nolin, A. W. (2018). Tree-Ring Carbon Isotope Records from the Western Oregon Cascade Mountains Primarily Record Summer Maximum Temperatures. *Tree-Ring Research*, *74*(2), 185–195. https://doi.org/10.3959/1536-1098-74.2.185

Rebetez, M., Saurer, M., & Cherubini, P. (2003). To What Extent Can Oxygen Isotopes in Tree Rings and Precipitation Be Used to Reconstruct Past Atmospheric Temperature? A Case Study. *Climatic Change*, *61*(1), 237–248. https://doi.org/10.1023/A:1026369000246

Renée Brooks, J., Barnard, H. R., Coulombe, R., & McDonnell, J. J. (2010). Ecohydrologic separation of water between trees and streams in a Mediterranean climate. *Nature Geoscience*, *3*(2), 100–104. https://doi.org/10.1038/ngeo722

Rhoades, A. M., Jones, A. D., Srivastava, A., Huang, H., O'Brien, T. A., Patricola, C. M., Ullrich, P. A., Wehner, M., & Zhou, Y. (2020). The Shifting Scales of Western U.S. Landfalling Atmospheric Rivers Under Climate Change. *Geophysical Research Letters*, *47*(17), e2020GL089096. https://doi.org/10.1029/2020GL089096

Roberge, A., Gyakum, J. R., & Atallah, E. H. (2009). Analysis of Intense Poleward Water Vapor Transports into High Latitudes of Western North America. *Weather and Forecasting*, *24*(6), 1732–1747. https://doi.org/10.1175/2009WAF2222198.1

Roden, J. S., & Ehleringer, J. R. (2007). Summer precipitation influences the stable oxygen and carbon isotopic composition of tree-ring cellulose in Pinus ponderosa. *Tree Physiology*, *27*(4), 491–501. https://doi.org/10.1093/treephys/27.4.491

Roden, J. S., Lin, G., & Ehleringer, J. R. (2000). A mechanistic model for interpretation of hydrogen and oxygen isotope ratios in tree-ring cellulose. *Geochimica et Cosmochimica Acta*, *64*(1), 21–35. https://doi.org/10.1016/S0016-7037(99)00195-7

Rutz, J. J., Shields, C. A., Lora, J. M., Payne, A. E., Guan, B., Ullrich, P., O'Brien, T., Leung, L. R., Ralph, F. M., Wehner, M., Brands, S., Collow, A., Goldenson, N., Gorodetskaya, I., Griffith, H., Kashinath, K., Kawzenuk, B., Krishnan, H., Kurlin, V., … Viale, M. (2019). The Atmospheric River Tracking Method Intercomparison Project (ARTMIP): Quantifying Uncertainties in Atmospheric River Climatology. *Journal of Geophysical Research: Atmospheres*, *124*(24), 13777–13802. https://doi.org/10.1029/2019JD030936

Ryu, Y., Jiang, C., Kobayashi, H., & Detto, M. (2018). MODIS-derived global land products of shortwave radiation and diffuse and total photosynthetically active radiation at 5 km resolution from 2000. *Remote Sensing of Environment*, *204*, 812–825. https://doi.org/10.1016/j.rse.2017.09.021

Sakashita, W., Miyahara, H., Yokoyama, Y., Aze, T., Obrochta, S. P., & Nakatsuka, T. (2017). Relationship between the Northern Pacific Gyre Oscillation and tree-ring cellulose oxygen isotopes in northeastern Japan. *Geoscience Letters*, *4*(1), 29. https://doi.org/10.1186/s40562-017-0095-2

Sanmiguel-Vallelado, A., Camarero, J. J., Gazol, A., Morán-Tejeda, E., Sangüesa-Barreda, G., Alonso-González, E., Gutiérrez, E., Alla, A. Q., Galván, J. D., & López-Moreno, J. I. (2019). Detecting snow-related signals in radial growth of *Pinus uncinata* mountain forests. *Dendrochronologia*, *57*, 125622. https://doi.org/10.1016/j.dendro.2019.125622

Sano, M., Tshering, P., Komori, J., Fujita, K., Xu, C., & Nakatsuka, T. (2013). May–September precipitation in the Bhutan Himalaya since 1743 as reconstructed from tree ring cellulose δ18O. *Journal of Geophysical Research: Atmospheres*, *118*(15), 8399–8410. https://doi.org/10.1002/jgrd.50664

Saurer, M., Cherubini, P., Reynolds-Henne, C. E., Treydte, K. S., Anderson, W. T., & Siegwolf, R. T. W. (2008). An investigation of the common signal in tree ring stable isotope chronologies at temperate sites. *Journal of Geophysical Research: Biogeosciences*, *113*(G4). https://doi.org/10.1029/2008JG000689

Schmidt-Simard, K. (2022). *Tree Rings and Oxygen Isotopes as Climatic Indicators in the U.S. Pacific Northwest* [University of North Carolina at Chapel Hill]. https://cdr.lib.unc.edu/concern/dissertations/zc77t135v

Schneider, U., Finger, P., Meyer-Christoffer, A., Rustemeier, E., Ziese, M., & Becker, A. (2017). Evaluating the Hydrological Cycle over Land Using the Newly-Corrected Precipitation Climatology from the Global Precipitation Climatology Centre (GPCC). *Atmosphere*, *8*(3), Article 3. https://doi.org/10.3390/atmos8030052

Seattle Public Utilities. (2019). *SPU's Risk and Resiliency Assessment and Framework—2019 Final Report*. https://www.insurance.wa.gov/sites/default/files/2020-05/2019-spu-risk-and-resiliency-assessment-and-framework.pdf

Shanley, C. S., Pyare, S., Goldstein, M. I., Alaback, P. B., Albert, D. M., Beier, C. M., Brinkman, T. J., Edwards, R. T., Hood, E., MacKinnon, A., McPhee, M. V., Patterson, T. M., Suring, L. H., Tallmon, D. A., & Wipfli, M. S. (2015). Climate change implications in the northern coastal temperate rainforest of North America. *Climatic Change*, *130*(2), 155–170. https://doi.org/10.1007/s10584-015-1355-9

Sharma, A. R., & Déry, S. J. (2020). Contribution of Atmospheric Rivers to Annual, Seasonal, and Extreme Precipitation Across British Columbia and Southeastern Alaska. *Journal of Geophysical Research: Atmospheres*, *125*(9), e2019JD031823. https://doi.org/10.1029/2019JD031823

Shi, C., Masson-Delmotte, V., Risi, C., Eglin, T., Stievenard, M., Pierre, M., Wang, X., Gao, J., Bréon, F.-M., Zhang, Q.-B., & Daux, V. (2011). Sampling strategy and climatic implications of tree-ring stable isotopes on the southeast Tibetan Plateau. *Earth and Planetary Science Letters*, *301*(1), 307–316. https://doi.org/10.1016/j.epsl.2010.11.014

Shields, C. A., & Kiehl, J. T. (2016a). Atmospheric river landfall-latitude changes in future climate simulations. *Geophysical Research Letters*, *43*(16), 8775–8782. https://doi.org/10.1002/2016GL070470

Shields, C. A., & Kiehl, J. T. (2016b). Simulating the Pineapple Express in the half degree Community Climate System Model, CCSM4. *Geophysical Research Letters*, *43*(14), 7767–7773. https://doi.org/10.1002/2016GL069476

Shields, C. A., Rutz, J. J., Leung, L.-Y., Ralph, F. M., Wehner, M., Kawzenuk, B., Lora, J. M., McClenny, E., Osborne, T., Payne, A. E., Ullrich, P., Gershunov, A., Goldenson, N., Guan, B., Qian, Y., Ramos, A. M., Sarangi, C., Sellars, S., Gorodetskaya, I., … Nguyen, P. (2018). Atmospheric River Tracking Method Intercomparison Project (ARTMIP): Project goals and experimental design. *Geoscientific Model Development*, *11*(6), 2455–2474. https://doi.org/10.5194/gmd-11-2455-2018

Siirila-Woodburn, E. R., Rhoades, A. M., Hatchett, B. J., Huning, L. S., Szinai, J., Tague, C., Nico, P. S., Feldman, D. R., Jones, A. D., Collins, W. D., & Kaatz, L. (2021). A low-to-no snow future and its impacts on water resources in the western United States. *Nature Reviews Earth & Environment*, *2*(11), Article 11. https://doi.org/10.1038/s43017-021-00219-y

Smith, E. T., & Sheridan, S. C. (2022). The relationship between teleconnections, surface temperature, and cold air outbreaks. *International Journal of Climatology*, *42*(3), 1531–1543. https://doi.org/10.1002/joc.7318

Snauffer, A. M., Hsieh, W. W., & Cannon, A J. (2016). Comparison of gridded snow water equivalent products with in sit measurements in British Columbia, Canada. *Journal of Hydrology, 541*(B). https://doi.org/10.1016/j.jhydrol.2016.07.027

Son, H.-Y., Park, W., Jeong, J.-H., Yeh, S.-W., Kim, B.-M., Kwon, M., & Kug, J.-S. (2012). Nonlinear impact of the Arctic Oscillation on extratropical surface air temperature. *Journal of Geophysical Research: Atmospheres*, *117*(D19). https://doi.org/10.1029/2012JD018090

Speer, J. H. (2010). *Fundamentals of Tree-ring Research*. University of Arizona Press.

Spry, C. M. (2013). *Understanding Extreme Precipitation Behaviour in British Columbia's Lower Mainland Using Historical and Proxy Data* [Simon Fraser University]. https://summit.sfu.ca/item/13790

Spry, C. M., Kohfeld, K. E., Allen, D. M., Dunkley, D., & Lertzman, K. (2014). Characterizing Pineapple Express storms in the Lower Mainland of British Columbia, Canada. *Canadian Water Resources Journal / Revue Canadienne Des Ressources Hydriques*, *39*(3), 302–323. https://doi.org/10.1080/07011784.2014.942574

Squamish Nation. (2024). *Our Land*. Squamish Nation. https://www.squamish.net/about-our-nation/our-land/

St. George, S. (2014). An overview of tree-ring width records across the Northern Hemisphere. *Quaternary Science Reviews*, *95*, 132–150. https://doi.org/10.1016/j.quascirev.2014.04.029

Stahle, D. W., Cleaveland, M. K., & Cerveny, R. S. (1991). Tree-ring reconstructed sunshine duration over central USA. *International Journal of Climatology*, *11*(3), 285–295. https://doi.org/10.1002/joc.3370110305

Starheim, C. C. A., Smith, D. J., & Prowse, T. D. (2013). Dendrohydroclimate reconstructions of July–August runoff for two nival-regime rivers in west central British Columbia. *Hydrological Processes*, *27*(3), 405–420. https://doi.org/10.1002/hyp.9257

Steiger, N. J., Smerdon, J. E., Cook, E. R., & Cook, B. I. (2018). A reconstruction of global hydroclimate and dynamical variables over the Common Era. *Scientific Data*, *5*(1), 180086. https://doi.org/10.1038/sdata.2018.86

Steinschneider, S., Ho, M., Williams, A. P., Cook, E. R., & Lall, U. (2018). A 500-Year Tree Ring-Based Reconstruction of Extreme Cold-Season Precipitation and Number of Atmospheric River Landfalls Across the Southwestern United States. *Geophysical Research Letters*, *45*(11), 5672–5680. https://doi.org/10.1029/2018GL078089

Stó:lō Research and Resource Management Centre. (2016). *Stó:lō Resource and Research Management*. https://www.srrmcentre.com/gis

Stone. (2022). *Fir tree icon*. The Noun Project. https://thenounproject.com/icon/fir-tree-4841585/

Sun, W., Liang, Y., Bi, H., Zhao, Y., Meng, J., & Zhang, J. (2022). Insight on Poleward Moisture and Energy Transport into the Arctic from ERA5. *Atmosphere*, *13*(4), Article 4. https://doi.org/10.3390/atmos13040616

Tang, W., Qin, J., Yang, K., Jiang, Y., & Pan, W. (2022). Mapping long-term and high-resolution global gridded photosynthetically active radiation using the ISCCP H-series cloud product and reanalysis data. *Earth System Science Data*, *14*(4), 2007–2019. https://doi.org/10.5194/essd-14-2007-2022

Tardif, J. C., Conciatori, F., & Leavitt, S. W. (2008). Tree rings, δ13C and climate in Picea glauca growing near Churchill, subarctic Manitoba, Canada. *Chemical Geology*, *252*(1), 88–101. https://doi.org/10.1016/j.chemgeo.2008.01.015

Tei, S., Sugimoto, A., Yonenobu, H., Yamazaki, T., & Maximov, T. C. (2013). Reconstruction of soil moisture for the past 100 years in eastern Siberia

by using δ13C of larch tree rings. *Journal of Geophysical Research: Biogeosciences*, *118*(3), 1256–1265. https://doi.org/10.1002/jgrg.20110

Thakur, B., Kalra, A., Lakshmi, V., Lamb, K. W., Miller, W. P., & Tootle, G. (2020). Linkage between ENSO phases and western US snow water equivalent. *Atmospheric Research*, *236*, 104827. https://doi.org/10.1016/j.atmosres.2019.104827

Thermo Fisher Scientific. (2008). *Thermo Scientific High Temperature Conversion Elemental Analyzer*. https://lachniet.faculty.unlv.edu/TC-EA_files/TC-EA_Thermo_Product_Guide.pdf

Thompson, D. W. J., Lee, S., & Baldwin, M. P. (2003). Atmospheric Processes Governing the Northern Hemisphere Annular Mode/North Atlantic Oscillation. In *The North Atlantic Oscillation: Climatic Significance and Environmental Impact* (pp. 81–112). American Geophysical Union (AGU). https://doi.org/10.1029/134GM05

Tohver, I. M., Hamlet, A. F., & Lee, S.-Y. (2014). Impacts of 21st-Century Climate Change on Hydrologic Extremes in the Pacific Northwest Region of North America. *JAWRA Journal of the American Water Resources Association*, *50*(6), 1461–1476. https://doi.org/10.1111/jawr.12199

Toride, K., & Hakim, G. J. (2021). Influence of Low-Frequency PNA Variability on MJO Teleconnections to North American Atmospheric River Activity. *Geophysical Research Letters*, *48*(13), e2021GL094078. https://doi.org/10.1029/2021GL094078

Trouet, V., & Taylor, A. H. (2010). Multi-century variability in the Pacific North American circulation pattern reconstructed from tree rings. *Climate Dynamics*, *35*(6), 953–963. https://doi.org/10.1007/s00382-009-0605-9

Tsleil-Waututh Nation. (2021). About Tsleil-Waututh Nation. *Tsleil-Waututh Nation*. https://twnation.ca/about/

Tsuji, H., Nakatsuka, T., & Takagi, K. (2006). δ18O of tree-ring cellulose in two species (spruce and oak) as proxies of precipitation amount and relative humidity in northern Japan. *Chemical Geology*, *231*(1), 67–76. https://doi.org/10.1016/j.chemgeo.2005.12.011

Vano, J. A., Nijssen, B., & Lettenmaier, D. P. (2015). Seasonal hydrologic responses to climate change in the Pacific Northwest. *Water Resources Research*, *51*(4), 1959–1976. https://doi.org/10.1002/2014WR015909

Vano, J. A., Voisin, N., Cuo, L., Hamlet, A. F., Elsner, M. M., Palmer, R. N., Polebitski, A., & Lettenmaier, D. P. (2010). Climate change impacts on water management in the Puget Sound region, Washington State, USA.

Climatic Change, *102*(1), 261–286. https://doi.org/10.1007/s10584-010-9846-1

Vystavna, Y., Matiatos, I., & Wassenaar, L. I. (2021). Temperature and precipitation effects on the isotopic composition of global precipitation reveal long-term climate dynamics. *Scientific Reports*, *11*(1), Article 1. https://doi.org/10.1038/s41598-021-98094-6

Wagenmakers, E.-J., & Farrell, S. (2004). AIC model selection using Akaike weights. *Psychonomic Bulletin & Review*, *11*(1), 192–196. https://doi.org/10.3758/BF03206482

Waliser, D., & Guan, B. (2017). Extreme winds and precipitation during landfall of atmospheric rivers. *Nature Geoscience*, *10*(3), Article 3. https://doi.org/10.1038/ngeo2894

Wang, H., & Asefa, T. (2018). Impact of different types of ENSO conditions on seasonal precipitation and streamflow in the Southeastern United States. *International Journal of Climatology*, *38*(3), 1438–1451. https://doi.org/10.1002/joc.5257

Watson, E., & Luckman, B. H. (2016). An investigation of the snowpack signal in moisture-sensitive trees from the Southern Canadian Cordillera. *Dendrochronologia*, *38*, 118–130. https://doi.org/10.1016/j.dendro.2016.03.008

Whitfield, P. H., Moore, R. D. (Dan), Fleming, S. W., & Zawadzki, A. (2010). Pacific Decadal Oscillation and the Hydroclimatology of Western Canada—Review and Prospects. *Canadian Water Resources Journal / Revue Canadienne Des Ressources Hydriques*, *35*(1), 1–28. https://doi.org/10.4296/cwrj3501001

Willett, K. (2023). *HadISDH - gridded global surface humidity dataset* [dataset]. Met Office Hadley Centre. https://www.metoffice.gov.uk/hadobs/hadisdh/

Wilson, G., Green, M., Brown, J., Campbell, J., Groffman, P., Duran, J., & Morse, J. (2020). Snowpack affects soil microclimate throughout the year. *CLIMATIC CHANGE*, *163*(2), 705–722. https://doi.org/10.1007/s10584-020-02943-8

Wise, E. K., & Dannenberg, M. P. (2022). Simulating the Impacts of Changes in Precipitation Timing and Intensity on Tree Growth. *Geophysical Research Letters*, *49*(22), e2022GL100863. https://doi.org/10.1029/2022GL100863

Wood, S. (2004). Stable and Efficient Multiple Smoothing Parameter Estimation for Generalized Additive Models. *Journal of the American Statistical Association*, *99*(467), 673–686. https://doi.org/10.1198/016214504000000980

Wood, S. (2011). Fast Stable Restricted Maximum Likelihood and Marginal Likelihood Estimation of Semiparametric Generalized Linear Models. *Journal of the Royal Statistical Society Series B: Statistical Methodology*, *73*(1), 3–36. https://doi.org/10.1111/j.1467-9868.2010.00749.x

Wood, S. (2017). *Generalized Additive Models: An Introduction with R, Second Edition* (2nd ed.). Chapman and Hall/CRC. https://doi.org/10.1201/9781315370279

Wood, S. (2023). *Choose.k Function*. https://www.rdocumentation.org/packages/mgcv/versions/1.9-0/topics/choose.k

Wu, A., Hsieh, W. W., Shabbar, A., Boer, G. J., & Zwiers, F. W. (2006). The nonlinear association between the Arctic Oscillation and North American winter climate. *Climate Dynamics*, *26*(7), 865–879. https://doi.org/10.1007/s00382-006-0118-8

Wu, Y., Hu, C., Hu, Z., Liu, Y., & Bräuning, A. (2023). Quantitative relative humidity reconstruction combining tree-ring with ice core oxygen isotope records. *Journal of Hydrology*, *617*, 129084. https://doi.org/10.1016/j.jhydrol.2023.129084

Xu, C., Shi, J., Zhao, Y., Nakatsuka, T., Sano, M., Shi, S., & Guo, Z. (2019). Early summer precipitation in the lower Yangtze River basin for AD 1845–2011 based on tree-ring cellulose oxygen isotopes. *Climate Dynamics*, *52*(3), 1583–1594. https://doi.org/10.1007/s00382-018-4212-5

Xu, C., Zheng, H., Nakatsuka, T., & Sano, M. (2013). Oxygen isotope signatures preserved in tree ring cellulose as a proxy for April–September precipitation in Fujian, the subtropical region of southeast China. *Journal of Geophysical Research: Atmospheres*, *118*(23), 12,805-12,815. https://doi.org/10.1002/2013JD019803

Xu, G., Liu, X., Hu, J., Dorado-Liñán, I., Gagen, M., Szejner, P., Chen, T., & Trouet, V. (2022). Intra-annual tree-ring δ18O and δ13C reveal a trade-off between isotopic source and humidity in moist environments. *Tree Physiology*, *42*(11), 2203–2223. https://doi.org/10.1093/treephys/tpac076

Xu, G., Liu, X., Qin, D., Chen, T., Sun, W., An, W., Wang, W., Wu, G., Zeng, X., & Ren, J. (2014). Drought history inferred from tree ring δ13C and δ18O in the central Tianshan Mountains of China and linkage with the North Atlantic Oscillation. *Theoretical and Applied Climatology*, *116*(3), 385–401. https://doi.org/10.1007/s00704-013-0958-1

Xu, G., Liu, X., Trouet, V., Treydte, K., Wu, G., Chen, T., Sun, W., An, W., Wang, W., Zeng, X., & Qin, D. (2019). Regional drought shifts (1710–2010) in East Central Asia and linkages with atmospheric circulation recorded in

tree-ring δ18O. *Climate Dynamics*, *52*(1), 713–727. https://doi.org/10.1007/s00382-018-4215-2

Yamaguchi, D. K. (1991). A simple method for cross-dating increment cores from living trees. *Canadian Journal of Forest Research*, *21*(3), 414–416. https://doi.org/10.1139/x91-053

Yu, B., Zhang, X., Lin, H., & Yu, J.-Y. (2015). Comparison of Wintertime North American Climate Impacts Associated with Multiple ENSO Indices. *Atmosphere-Ocean*, *53*(4), 426–445. https://doi.org/10.1080/07055900.2015.1079697

Zhang, C. (2005). Madden-Julian Oscillation. *Reviews of Geophysics*, *43*(2). https://doi.org/10.1029/2004RG000158

Zheng, C., Chang, E. K.-M., Kim, H.-M., Zhang, M., & Wang, W. (2018). Impacts of the Madden–Julian Oscillation on Storm-Track Activity, Surface Air Temperature, and Precipitation over North America. *Journal of Climate*, *31*(15), 6113–6134. https://doi.org/10.1175/JCLI-D-17-0534.1

Zhu, Y., & Newell, R. E. (1998). A Proposed Algorithm for Moisture Fluxes from Atmospheric Rivers. *Monthly Weather Review*, *126*(3), 725–735. https://doi.org/10.1175/1520-0493(1998)126<0725:APAFMF>2.0.CO;2

Appendix A: Chapter 2 supplemental tables

Table A.1 Location and tree characteristics for Pacific silver firs sampled for radial growth at MKRF-1.

Sample ID	Latitude	Longitude	Elevation (masl)	Diameter at Breast Height (DBH) (m)	Tree height (m)	Record length*	Sampling date*
PSF-11	49.328549	-122.543340	438.99	0.40	38	1937 - 2021, 1937 - 2022	08-26-2022, 03-30-2023
PSF-12	49.328645	-122.543239	437.06	0.42	33	1942 - 2021	10-20-2022
PSF-13	49.328750	-122.543303	437.78	0.49	31	1936 - 2021, 1936 - 2021	08-09-2022, 10-20-2022
PSF-15	49.328729	-122.543869	442.19	0.32	33	1933 - 2021	08-09-2022
PSF-17	49.329012	-122.543195	436.62	0.27	31	1934 - 2021, 1934 - 2022	08-26-2022, 03-30-2023
PSF-26	49.328484	-122.543335	439.86	0.30	33	1952 - 2022	03-30-2023
PSF-27	49.328689	-122.543462	439.47	0.40	33	1933 - 2022	03-30-2023
PSF-28	49.327987	-122.543324	449.33	0.36	32	1940 - 2022	04-26-2023
PSF-30	49.327795	-122.543226	451.72	0.48	34	1939 - 2022	04-26-2023
PSF-31	49.327844	-122.543198	450.25	0.50	33	1941 - 2022	04-26-2023
PSF-32	49.327983	-122.541668	440.26	0.38	31	1937 - 2022	05-22-2023
PSF-33	49.327996	-122.541893	440.39	0.37	31	1931 - 2022	05-22-2023
PSF-36	49.328063	-122.541827	439.95	0.27	30	1939 - 2022	05-22-2023
PSF-37	49.328474	-122.541995	438.49	0.42	33	1933 - 2022	05-22-2023

Sample ID	Latitude	Longitude	Elevation (masl)	Diameter at Breast Height (DBH) (m)	Tree height (m)	Record length*	Sampling date*
PSF-38	49.328646	-122.542147	437.87	0.23	30	1946 - 2022	05-22-2023

* For trees with cores sampled on different days, the record length and sampling date of the earlier sampled core is listed first, followed by the core sampled later.

Table A.2 *P* values, adjusted R^2, and DE for the single-predictor GAMs between the MKRF-1 annual growth index and AR and climate variables. *P* values <0.05 and R^2≥0.10 are shown in bold.

	WY	AMJ	JAS	OND	JFM
AR variables					
Total AR count	p = 0.71 R^2 = -0.01 DE = 0.02	**p = 0.03** R^2 = 0.06 DE = 0.07	p = 0.15 R^2 = 0.02 DE = 0.04	p = 0.88 R^2 = -0.02 DE = 0.00	p = 0.45 R^2 = -0.01 DE = 0.01
Percent AR precipitation	p = 0.27 R^2 = 0.00 DE = 0.01	p = 0.11 R^2 = 0.03 DE = 0.04	p = 0.56 R^2 = 0.01 DE = 0.04	p = 0.72 R^2 = -0.01 DE = 0.01	p = 0.74 R^2 = -0.02 DE = 0.02
Intense AR count	p = 0.12 R^2 = 0.06 DE = 0.09	**p = 0.02** R^2 = 0.07 DE = 0.08	p = 0.72 R^2 = -0.01 DE = 0.00	p = 0.18 R^2 = 0.04 DE = 0.07	p = 0.73 R^2 = -0.02 DE = 0.00
Climate variables					
Mean temperature	p = 0.37 R^2 = 0.00 DE = 0.01	p = 0.07 R^2 = 0.04 DE = 0.05	p = 0.86 R^2 = -0.01 DE = 0.00	p = 0.67 R^2 = 0.00 DE = 0.02	p = 0.27 R^2 = 0.00 DE = 0.00
Total precipitation	p = 0.54 R^2 = -0.01 DE = 0.01	p = 0.22 R^2 = 0.01 DE = 0.03	p = 0.58 R^2 = 0.01 DE = 0.00	p = 0.35 R^2 = 0.00 DE = 0.01	p = 0.89 R^2 = -0.02 DE = 0.00
SPEI	p = 0.77 R^2 = -0.01 DE = 0.01	p = 0.44 R^2 = 0.01 DE = 0.04	p = 0.54 R^2 = 0.01 DE = 0.02	p = 0.56 R^2 = 0.00 DE = 0.02	p = 0.90 R^2 = -0.02 DE = 0.25
MCC	p = 0.42 R^2 = -0.01 DE = 0.01	p = 0.74 R^2 = -0.02 DE = 0.00	p = 0.92 R^2 = -0.02 DE = 0.00	p = 0.41 R^2 = -0.01 DE = 0.01	p = 0.26 R^2 = 0.00 DE = 0.02
SWE	**p = <0.01** **R^2 = 0.24** DE = 0.25				
Climate oscillation indices					

	WY	AMJ	JAS	OND	JFM
MJO	**p = 0.03** **R^2 = 0.19** DE = 0.24	p = 0.27 R^2 = 0.01 DE = 0.03	**p = 0.06** **R^2 = 0.13** DE = 0.18	p = 0.35 R^2 = 0.00 DE = 0.02	**p = 0.01** **R^2 = 0.12** DE = 0.14
PDO	**p = <0.01** **R^2 = 0.17** DE = 0.18	**p = <0.01** **R^2 = 0.29** DE = 0.32	**p = <0.01** **R^2 = 0.20** DE = 0.22	p = 0.81 R^2 = -0.02 DE = 0.11	p = 0.46 R^2 = -0.01 DE = 0.00
Niño 3.4	p = 0.10 R^2 = 0.09 DE = 0.12	**p = 0.02** **R^2 = 0.15** DE = 0.19	p = 0.98 R^2 = -0.02 DE = 0.00	p = 0.74 R^2 = -0.01 DE = 0.00	p = 0.46 R^2 = 0.01 DE = 0.03
AO	**p = 0.02** R^2 = 0.07 DE = 0.09	p = 0.40 R^2 = 0.10 DE = 0.03	**p = 0.04** R^2 = 0.05 DE = 0.07	p = 0.35 R^2 = 0.00 DE = 0.13	**p = 0.01** **R^2 = 0.12** DE = 0.09
NPGO	p = 0.24 R^2 = 0.01 DE = 0.02	p = 0.48 R^2 = -0.01 DE = 0.01	p = 0.21 R^2 = 0.01 DE = 0.03	p = 0.07 R^2 = 0.04 DE = 0.06	p = 0.50 R^2 = 0.00 DE = 0.01
PNA	p = 0.53 R^2 = -0.01 DE = 0.09	**p = 0.02** R^2 = 0.08 DE = 0.10	p = 0.08 R^2 = 0.04 DE = 0.05	p = 0.81 R^2 = -0.02 DE = 0.00	p = 0.46 R^2 = -0.01 DE = 0.01

Table A.3 ***P*** **values, adjusted** ***R^2***, **and DE for the single-predictor GAMs between the MKRF-1 earlywood growth index and AR and climate variables.** ***P*** **values <0.05 and** ***R^2*** **≥0.10 are shown in bold.**

	WY	AMJ	JAS	OND	JFM
AR variables					
Total AR count	p = 0.58 R^2 = -0.01 DE = 0.01	p = 0.08 R^2 = 0.02 DE = 0.09	p = 0.21 R^2 = 0.01 DE = 0.03	p = 0.58 R^2 = -0.01 DE = 0.01	p = 0.30 R^2 = 0.00 DE = 0.02
Percent AR precipitation	p = 0.41 R^2 = 0.00 DE = 0.01	**p = 0.02** R^2 = 0.07 DE = 0.09	p = 0.77 R^2 = -0.01 DE = 0.02	p = 0.86 R^2 = -0.01 DE = 0.01	p = 0.57 R^2 = -0.01 DE = 0.01
Intense AR count	p = 0.33 R^2 = 0.04 DE = 0.07	**p = 0.01** R^2 = 0.09 DE = 0.10	p = 0.72 R^2 = -0.01 DE = 0.00	p = 0.27 R^2 = 0.03 DE = 0.06	p = 0.59 R^2 = -0.01 DE = 0.00
Climate variables					
Mean temperature	p = 0.59 R^2 = -0.01 DE = 0.04	p = 0.17 R^2 = 0.02 DE = 0.03	p = 0.52 R^2 = 0.01 DE = 0.04	p = 0.78 R^2 = -0.01 DE = 0.01	p = 0.36 R^2 = 0.00 DE = 0.01

	WY	AMJ	JAS	OND	JFM
Total precipitation	p = 0.67 R^2 = -0.01 DE = 0.00	p = 0.20 R^2 = 0.01 DE = 0.03	p = 0.48 R^2 = -0.01 DE = 0.01	p = 0.47 R^2 = -0.01 DE = 0.01	p = 0.79 R^2 = -0.01 DE = 0.00
SPEI	p = 0.80 R^2 = -0.01 DE = 0.01	p = 0.35 R^2 = 0.02 DE = 0.04	p = 0.51 R^2 = 0.00 DE = 0.02	p = 0.65 R^2 = -0.01 DE = 0.01	p = 0.79 R^2 = 0.00 DE = 0.02
MCC	p = 0.52 R^2 = 0.00 DE = 0.01	p = 0.54 R^2 = -0.01 DE = 0.01	p = 0.88 R^2 = -0.02 DE = 0.00	p = 0.41 R^2 = 0.00 DE = 0.01	p = 0.33 R^2 = 0.00 DE = 0.02
SWE	**p = <0.01** **R^2 = 0.22** DE = 0.23				
Climate oscillation indices					
MJO	**p = 0.01** **R^2 = 0.24** DE = 0.29	p = 0.30 R^2 = 0.03 DE = 0.07	p = 0.05 **R^2 = 0.15** DE = 0.19	p = 0.51 R^2 = -0.01 DE = 0.01	**p = 0.01** **R^2 = 0.12** DE = 0.14
PDO	**p = <0.01** **R^2 = 0.16** DE = 0.18	**p = <0.01** **R^2 = 0.28** DE = 0.31	**p = <0.01** **R^2 = 0.19** DE = 0.20	**p = 0.01** **R^2 = 0.10** DE = 0.11	**p = 0.01** R^2 = 0.09 DE = 0.11
Niño 3.4	p = 0.12 R^2 = 0.08 DE = 0.12	**p = 0.02** **R^2 = 0.15** DE = 0.19	p = 0.82 R^2 = -0.01 DE = 0.00	p = 0.82 R^2 = -0.01 DE = 0.00	p = 0.55 R^2 = 0.00 DE = 0.03
AO	p = 0.57 R^2 = 0.04 DE = 0.06	p = 0.27 R^2 = 0.02 DE = 0.05	p = 0.06 R^2 = 0.04 DE = 0.06	p = 0.06 **R^2 = 0.11** DE = 0.15	p = 0.05 R^2 = 0.05 DE = 0.07
NPGO	p = 0.48 R^2 = -0.01 DE = 0.01	p = 0.81 R^2 = -0.02 DE = 0.00	p = 0.40 R^2 = 0.00 DE = 0.01	p = 0.18 R^2 = 0.01 DE = 0.03	p = 0.74 R^2 = -0.01 DE = 0.02
PNA	p = 0.44 R^2 = -0.01 DE = 0.01	**p = 0.01** **R^2 = 0.10** DE = 0.11	p = 0.44 R^2 = 0.05 DE = 0.07	p = 0.66 R^2 = -0.01 DE = 0.00	p = 0.36 R^2 = 0.00 DE = 0.01

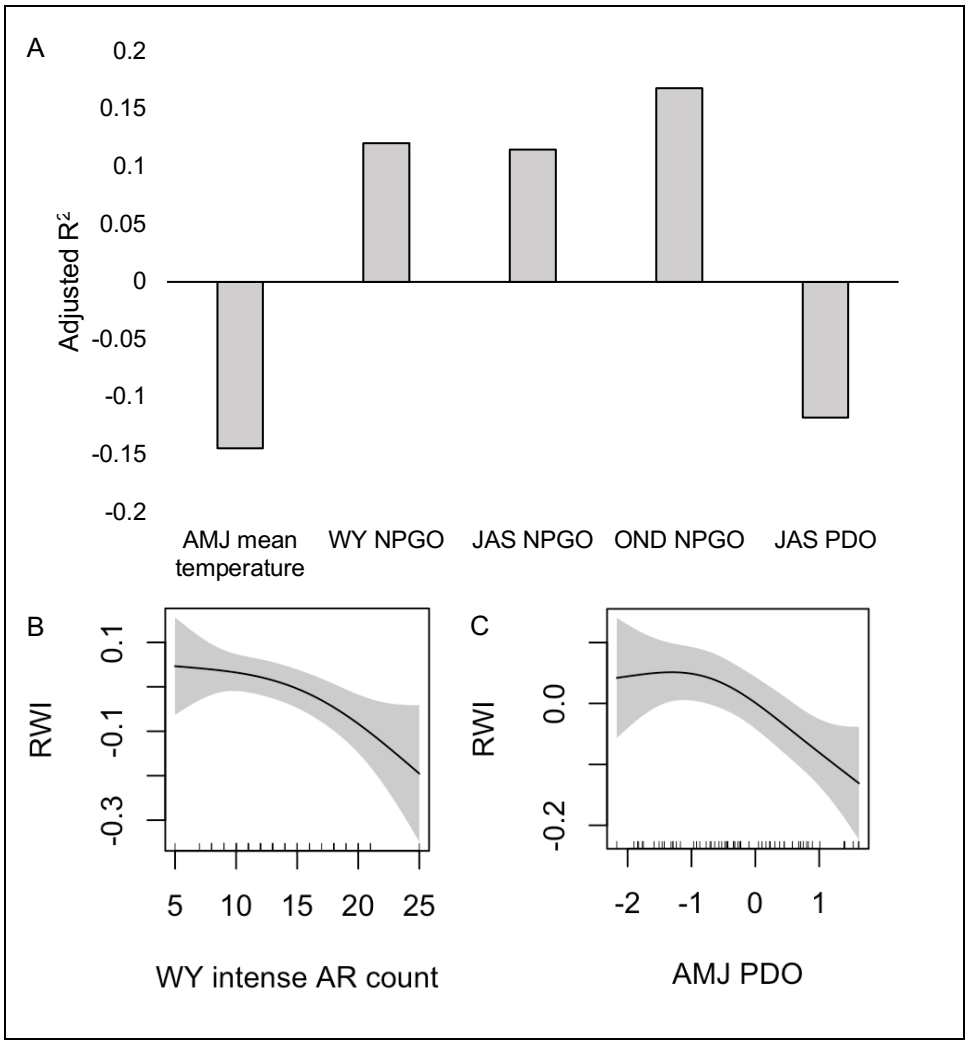

Figure A.1 **Variables with significant (p<0.05 and R^2≥0.10) relationships with the MKRF-1 latewood radial width index (RWI) in single-predictor GAMs. (A) the adjusted R^2 values and direction of the relationship (assessed visually, as adjusted R^2 values do not have a sign) for variables with linear relationships with annual RWI. (B) and (C) the shape of the significant variables with non-linear relationships to latewood RWI, with y-axes zero-centered and small vertical lines denoting the distribution of AR and climate oscillation data.**

Table A.4 Multi-predictor GAM iterations for latewood RWI.

GAM iteration	Input variables	Adjusted R^2	Deviance explained (%)	AIC	Penalized variables	Non-penalized variable pairs with concurvity above 0.5
1 Significant non-AR variables	OND mean temperature WY NPGO OND NPGO JAS NPGO WY PDO JAS PDO	0.214	24.4	-78.3	OND mean temperature WY NPGO JAS NPGO WY PDO	None
2 Remove penalized non-AR variables and add AR variables	OND NPGO JAS PDO WY total AR count JFM total AR count AMJ total AR count JAS total AR count OND total AR count WY %AR precipitation JFM %AR precipitation AMJ %AR precipitation JAS %AR precipitation OND %AR precipitation	0.348	40.4	-85.6	WY total AR count JFM total AR count AMJ total AR count OND total AR count WY %AR precipitation JFM %AR precipitation AMJ %AR precipitation	None

GAM iteration	Input variables	Adjusted R^2	Deviance explained (%)	AIC	Penalized variables	Non-penalized variable pairs with concurvity above 0.5
3 Remove penalized variables and add remaining AR variables	OND NPGO JAS PDO JAS total AR count JAS %AR precipitation OND %AR precipitation WY intense AR count JAS intense AR count AMJ intense AR count JFM intense AR count OND intense AR count	0.477	54.0	-95.7	OND % AR precipitation AMJ intense AR count JAS intense AR count OND intense AR count	None
4 Remove penalized variables and create final GAM	OND NPGO JAS PDO JAS total AR count JAS %AR precipitation WY intense AR count JFM intense AR count	0.477	54.0	-95.7	None	None

Table A.5 Summary results of the final multi-predictor GAM for latewood RWI. *P* values less than 0.05 are shown in bold. EDF indicates the variable's estimated degrees of freedom in the GAM.

Response variable	EDF	*F statistic*	*p* value
JAS AR count	1.022	1.90	**0.01**
JAS % AR precipitation	1.555	1.82	**0.03**
WY intense AR count	1.378	6.08	**<0.01**
JFM intense AR count	0.883	0.50	0.18
OND NPGO	1.383	1.87	**0.02**
JAS PDO	0.925	4.09	**<0.01**

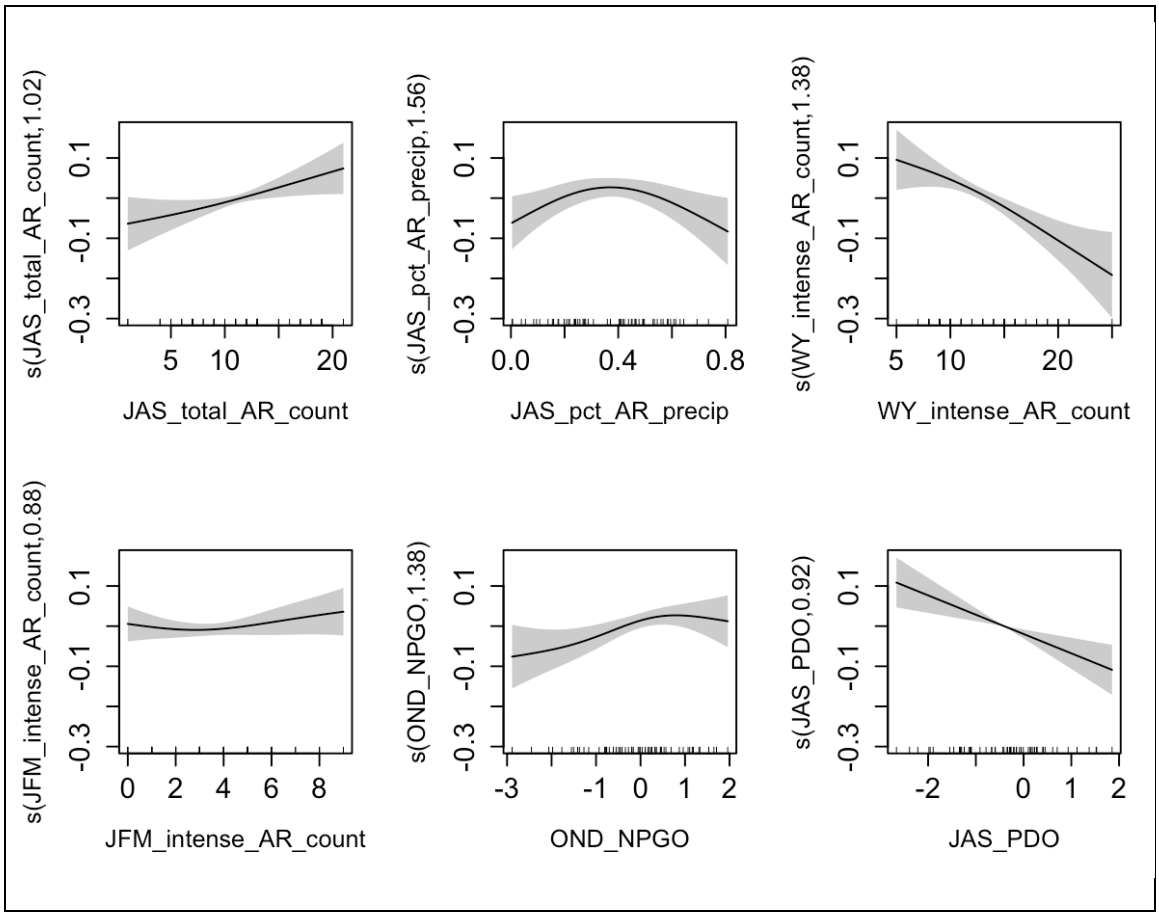

Figure A.2 **Individual partial effects of the smooth functions of predictor variables on the latewood RWI response variable. The predictor variables included are those retained (i.e., not penalized) in the final multi-predictor GAM. Y-axis values are zero-centered, and the numbers following the y-axis labels are the predictor variables' effective degrees of freedom in the GAM. The shaded area indicates the 95% confidence interval andmall vertical lines on the x-axes denote the distribution of AR and climate data.**

Table A.6 ***P*** **values, adjusted** R^2**, and DE for the single-predictor GAMs between the MKRF-1 latewood growth index and AR and climate variables.** ***P*** **values <0.05 and** R^2**≥0.10 are shown in bold.**

	WY	AMJ	JAS	OND	JFM
AR variables					
AR count	p = 0.61 R^2 = -0.01 DE = 0.00	p = 0.38 R^2 = 0.00 DE = 0.01	p = 0.18 R^2 = 0.01 DE = 0.03	p = 0.23 R^2 = 0.00 DE = 0.02	p = 0.49 R^2 = -0.01 DE = 0.01
Percent AR precipitation	p = 0.05 R^2 = 0.05 DE = 0.06	p = 0.31 R^2 = 0.00 DE = 0.02	p = 0.45 R^2 = 0.02 DE = 0.05	p = 0.07 R^2 = 0.04 DE = 0.06	p = 0.24 R^2 = 0.01 DE = 0.02

	WY	AMJ	JAS	OND	JFM
Intense AR count	**p = 0.02** **R^2 = 0.12** DE = 0.15	p = 0.10 R^2 = 0.03 DE = 0.05	p = 0.42 R^2 = 0.01 DE = 0.04	p = 0.05 R^2 = 0.05 DE = 0.07	p = 0.38 R^2 = 0.02 DE = 0.06
Climate variables					
Mean temperature	**p = <0.01** R^2 = 0.08 DE = 0.10	**p = <0.01** **R^2 = 0.14** DE = 0.16	**p = 0.03** R^2 = 0.06 DE = 0.07	p = 0.76 R^2 = -0.01 DE = 0.00	p = 0.06 R^2 = 0.04 DE = 0.06
Total precipitation	p = 0.33 R^2 = 0.00 DE = 0.02	p = 0.15 R^2 = 0.02 DE = 0.04	p = 0.84 R^2 = -0.02 DE = 0.00	p = 0.51 R^2 = -0.01 DE = 0.01	p = 0.53 R^2 = 0.01 DE = 0.04
SPEI	p = 0.86 R^2 = -0.01 DE = 0.01	p = 0.48 R^2 = -0.01 DE = 0.01	p = 0.24 R^2 = 0.01 DE = 0.02	p = 0.50 R^2 = -0.01 DE = 0.01	p = 0.95 R^2 = -0.02 DE = 0.00
MCC	p = 0.33 R^2 = 0.00 DE = 0.02	p = 0.75 R^2 = -0.01 DE = 0.01	p = 0.93 R^2 = -0.02 DE = 0.00	p = 0.36 R^2 = 0.00 DE = 0.01	p = 0.14 R^2 = 0.02 DE = 0.04
SWE	p = 0.07 R^2 = 0.03 DE = 0.05				
Climate oscillation indices					
MJO	p = 0.28 R^2 = 0.07 DE = 0.11	p = 0.10 R^2 = 0.04 DE = 0.06	p = 0.82 R^2 = -0.02 DE = 0.00	p = 0.09 R^2 = 0.04 DE =0.07	p = 0.07 R^2 = 0.05 DE = 0.08
PDO	**p = 0.02** R^2 = 0.07 DE = 0.09	**p = <0.01** **R^2 = 0.17** DE = 0.20	**p = <0.01** **R^2 = 0.12** DE = 0.13	p = 0.23 R^2 = 0.01 DE = 0.02	p = 0.49 R^2 = -0.01 DE = 0.01
ENSO	**p = 0.04** R^2 = 0.05 DE = 0.07	**p = 0.01** R^2 = 0.09 DE = 0.10	p = 0.40 R^2 = 0.00 DE = 0.01	p = 0.17 R^2 = 0.02 DE = 0.03	p = 0.08 R^2 = 0.04 DE = 0.05
AO	**p = 0.01** R^2 = 0.09 DE = 0.10	p = 0.26 R^2 = 0.04 DE = 0.07	**p = 0.02** R^2 = 0.08 DE = 0.09	p = 0.18 R^2 = 0.01 DE = 0.03	**p = 0.03** R^2 = 0.06 DE = 0.08
NPGO	**p = <0.01** **R^2 = 0.12** DE = 0.13	**p = 0.02** R^2 = 0.07 DE = 0.09	**p = <0.01** **R^2 = 0.11** DE = 0.13	**p = <0.01** **R^2 = 0.17** DE = 0.18	**p = 0.02** R^2 = 0.07 DE = 0.09
PNA	p = 0.27 R^2 = 0.00 DE = 0.02	p = 0.22 R^2 = 0.01 DE = 0.03	p = 0.37 R^2 = 0.00 DE = 0.01	p = 0.68 R^2 = -0.01 DE = 0.00	p = 0.51 R^2 = -0.01 DE = 0.01

Table A.7 Post-hoc Pearson correlation results for variables of interest.

Variable 1	Variable 2	N	Pearson's r	*p*
Mean SWE	WY AR count	58	-0.27	0.03
AMJ % AR precipitation	AMJ intense AR count	58	0.86	<0.01
AMJ intense AR count	Earlywood RWI	58	-0.32	0.01
Spring PDO	Annual RWI	58	-0.43	<0.01
Mean SWE	Annual RWI	58	-0.50	<0.01

Appendix B: Procedure for α-cellulose extraction

This procedure was developed by Zheng-Hua Li at the Stable Isotope Laboratory at the University of Tennessee in Knoxville as a modification of the methodologies of Bronstert et al. (2023) and Leavitt & Danzer (1993).

Part A (Day 1)

1. Prepare the tree ring samples (date, slice into annual increments, and pool appropriately).
2. Set up the ultrasonic bath under the fume hood. Turn on the heat for the ultrasonic bath and set temperature to 69°C. Fill the bath with distilled water. The water level should be close to the fill line when you have 2 1-L beakers in the bath, but not too full that the water will spill over into the beakers and contaminate the samples. Cover the bath with the lid and let it warm up.
3. Label 8 Soxhlet extraction tubes and 2 1-L beakers using different coloured elastic bands.
4. Tree ring samples should already be prepared (dated, sanded and separated into annual or seasonal rings for analysis). One at a time, slice each sample into small slivers, as thin as possible.
5. Add a couple small drops of deionized (DI) water and grind the sample in agate mortar and pestle until it is soft and the fibers begin to pull apart.
6. Place the sample in a labelled extraction tube using tweezers and some DI water to flush all the remaining fibers out. Write down the sample name and corresponding extraction tube # in the notebook (e.g. DF3A 1980 EW, red tube in yellow beaker). Do this for all 8 samples.
7. Place four extraction tubes in each labelled beaker. For each beaker, pour in 175 mL DI water, 1.7 mL acetic acid (glacial) and 2.5 g of sodium chlorite. Disperse the ingredients evenly amongst all 4 tubes in the beaker.
8. Place the beakers in the ultrasonic bath for four hours with three additions of acetic acid (1.7 mL) and sodium chlorite (2.5 g), one after each hour. Place half-full plastic laboratory bottles (e.g. Nalgene bottles) around the beakers or on top, depending on the size and beaker arrangement in the ultrasonic bath. Make sure that the beakers are weigh down or propped up by the plastic bottles sufficiently so that the beakers can’t tip over.
9. Keep an eye on the samples in the bath to make sure the elastics stay on and that they don’t tip over.
10. Remove the extraction tubes from the bath after four hours and remove the solution by vacuum filtration (you can create a vacuum

filtration system using the lab sink, a rubber tube, a large Erlenmeyer flask and a rubber stopper).

11. While each tube/sample is still hooked up to the vacuum filtration system, wash the samples with deionized water (fill the tube halfway and let it drain three times).
12. Rinse the two large beakers with DI and place the tubes back in the correct beakers.

Part B (Day 2)

1. Heat up the bath to 69°C.
2. Grind the samples again using a mortar and pestle and a couple drops DI water. The samples should be ground enough that they appear fibrous Another drop or two of water may be necessary to achieve the right consistency. The sample should together and form one wet ball of fiber when picked up with tweezers. It should also have turned a white colour, as opposed to a more yellowy or brown wood colour. This is called holocellulose.
3. Add a 10% w/v sodium hydroxide mixture (i.e., 10 mg per 100 mL di water) to the beakers (about 200 mL per beaker is fine, or 50 mL per tube) and sonicate for 45 minutes at 69 °C.
4. Remove the tubes from the beaker, drain the solution and wash once more with deionized water (~50 mL).
5. Add a 17% w/v sodium hydroxide solution to the beakers, about 200 mL per beaker. Sonicate for 45 minutes <u>at room temperature</u> (use distilled water in the sonicator bath).
6. Remove the tubes from the beakers and remove residual sodium hydroxide solution by filtration under vacuum.
7. Wash the α-cellulose with 17% w/v sodium hydroxide solution (~20 mL per sample).
8. Wash the α-cellulose with copious amounts of deionized water (using vacuum filtration procedure).
9. Wash the α-cellulose with 1% hydrochloric acid (~20 mL per sample).
10. Flush the α-cellulose with large volumes of cold deionized water until the washings are neutral (use pH paper to test for neutrality).
11. Remove the sample from the extraction tube using tweezers. (Again, you should be able to pick up the whole sample as one mass). Place the sample in a small labelled (pre-weighed) sample vial.
12. Place all 8 sample vials in an oven at 40 °C for at least four hours.
13. Weigh when dry.

Appendix C: Chapter 3 supplemental tables

Table C.1 Location and tree characteristics for the Douglas-fir trees sampled at Capilano and MKRF-2. Two cores were collected per tree. DBH indicates the diameter at breast height.

Site	Sample name	Latitude	Longitude	Metres above sea level	DBH (m)	Tree height (m)
Capilano	Cap_T1C2	49.354825	-123.111650	67.58	0.98	51
Capilano	Cap_T3C2	49.354667	-123.111675	66.74	1.51	>55
Capilano	Cap_T4C3	49.354540	-123.111541	65.14	0.73	43
Capilano	Cap_T5C2	49.354563	-123.111860	65.03	1.21	54
MKRF-2	MK_T3C1	49.279912	-122.584259	173.81	1.46	>55
MKRF-2	MK _T4C1	49.279729	-122.584194	173.65	1.42	>55
MKRF-2	MK _T6C1	49.279973	-122.584214	174.97	1.23	>55
MKRF-2	MK _T7C1	49.279983	-122.584106	176.55	1.07	51

Table C.2 Selected tree ring cellulose records from western North America.

Chronology	Location	Temporal coverage	Tree species	Number of trees	Record details
Csank_BR (Csank et al., 2016)	Southern coastal Alaska, USA	1950-1995	White spruce (*Picea glauca*)	4	Only the live tree chronologies from this site were analyzed.
Csank_PB (Csank et al., 2016)	Southern coastal Alaska, USA	1950-1995	White spruce (*Picea glauca*)	4	Only the live tree chronologies from this site were analyzed.
Csank_V (Csank et al., 2016)	Southern coastal Alaska, USA	1950-1995	White spruce (*Picea glauca*)	4	Only the live tree chronologies from this site were analyzed.
Hudson_AB (Hudson et al., 2015)	Eastern Alaska, USA	1991-2009	White spruce (*Picea glauca*)	6	"Upper" and "lower" records from this site were 25 m apart. The two records were averaged into one for this analysis.
Hudson_BB (Hudson et al., 2015)	Central Alaska, USA	1991-2009	White spruce (*Picea glauca*)	6	"Upper" and "lower" records from this site were 25 m apart. The two records were averaged into one for this analysis.

Chronology	Location	Temporal coverage	Tree species	Number of trees	Record details
Hudson_NB (Hudson et al., 2015)	Central Alaska, USA	1991-2009	White spruce (*Picea glauca*)	6	"Upper" and "lower" records from this site were 25 m apart. The two records were averaged into one for this analysis.
Porter (Porter et al., 2014)	Northwestern Northwest Territories, Canada	1780-2003	White spruce (*Picea glauca*)	3	None.
Simard_ID (Schmidt-Simard, 2022)	Northwestern Idaho, USA	2006-2018	Ponderosa pine (*Pinus ponderosa*)	6	Earlywood and latewood $\delta^{18}O$ values were averaged by year for this analysis.
Simard_OR (Schmidt-Simard, 2022)	Northeastern Oregon, USA	2006-2018	Ponderosa pine (*Pinus ponderosa*)	5	Earlywood and latewood $\delta^{18}O$ values were averaged by year for this analysis.
Simard_WA (Schmidt-Simard, 2022)	Southwestern Washington, USA	2006-2018	Ponderosa pine (*Pinus ponderosa*)	10	Earlywood and latewood $\delta^{18}O$ values were averaged by year for this analysis.
Spry (Spry, 2013)	Southwestern British Columbia, Canada*	1960-1995	Douglas-fir (*Pseudotsuga menziesii*)	1	Earlywood and latewood $\delta^{18}O$ values were averaged by year for this analysis.

* Note that the Spry site is located <200 m from the Capilano site described in Chapter 3.

Table C.3 ***P*** **values, adjusted** R^2 **values, and deviance explained (DE) for the single-factor GAMs between annual tree ring** $\delta^{18}O$ **measured from Capilano and water year PE and climate variables.** ***P*** **values <0.05 are shown in bold.**

	WY	AMJ	JAS	OND	JFM
PE variables					
PE count	p = 0.65 R^2 = 0.02 DE = 0.08	p = 0.87 R^2 = -0.03 DE =<0.01	p = 0.82 R^2 = -0.03 DE = <0.01	p = 0.26 R^2 = 0.10 DE = 0.16	p = 0.28 R^2 = 0.05 DE = 0.10
Intense PE count	p = 0.76 R^2 = -0.03 DE = 0.00	*	*	p = 0.53 R^2 = 0.01 DE = 0.05	p = 0.96 R^2 = -0.03 DE = 0.00
% PE precipitation	p = 0.27 R^2 = 0.06 DE = 0.12	p = >0.99 R^2 = -0.03 DE = 0.01	p = 0.87 R^2 = -0.03 DE = <0.01	p = 0.98 R^2 = -0.03 DE =<0.01	p = 0.47 R^2 = -0.01 DE = 0.02
Climate variables					
Mean temperature	p = 0.49 R^2 = 0.03 DE = 0.08	p = 0.78 R^2 = -0.03 DE =<0.01	p = 0.37 R^2 = -0.01 DE = 0.02	**p = 0.03** R^2 = 0.10 DE = 0.13	p = 0.34 R^2 = 0.07 DE = 0.12
Total precipitation	p = 0.08 R^2 = 0.06 DE = 0.09	p = 0.06 R^2 = 0.18 DE = 0.24	p = 0.83 R^2 = -0.03 DE = <0.01	p = 0.55 R^2 = 0.01 DE = 0.05	p = 0.37 R^2 = <0.01 DE = 0.02
SPEI	**p = 0.03** R^2 = 0.10 DE = 0.13	p = 0.05 R^2 = 0.08 DE = 0.11	p = 0.31 R^2 = 0.05 DE = 0.10	p = 0.14 R^2 = 0.04 DE = 0.06	p = 0.51 R^2 = -0.02 DE = 0.01
SWE	p = 0.37 R^2 = -0.01 DE = 0.02				
GS-RH	**p = 0.01** R^2 = 0.14 DE = 0.17				
Climate oscillation indices					
MJO	p = 0.34 R^2 = <0.01 DE = 0.03	p = 0.64 R^2 = -0.02 DE = 0.01	p = 0.81 R^2 = -0.03 DE =<0.01	p = 0.15 R^2 = 0.03 DE = 0.06	p = 0.45 R^2 = -0.01 DE = 0.02
PDO	p = 0.37 R^2 = -0.01 DE = 0.02	p = 0.24 R^2 = 0.01 DE = 0.04	p = 0.51 R^2 = 0.01 DE = 0.06	p = 0.68 R^2 = -0.02 DE = <0.01	p = 0.72 R^2 = -0.03 DE =<0.01

	WY	AMJ	JAS	OND	JFM
ENSO	p = 0.46 R^2 = -0.01 DE = 0.02	p = 0.81 R^2 = -0.03 DE =<0.01	p = 0.40 R^2 = -0.01 DE = 0.02	p = 0.47 R^2 = -0.01 DE = 0.02	p = 0.65 R^2 = -0.02 DE = 0.01
AO	p = 0.20 R^2 = 0.02 DE = 0.05	**p = 0.02** R^2 = 0.21 DE = 0.27	p = 0.94 R^2 = -0.03 DE =<0.01	p = 0.89 R^2 = -0.03 DE =<0.01	p = 0.05 R^2 = 0.08 DE = 0.11
NPGO	p = 0.50 R^2 = 0.02 DE = 0.06	p = 0.68 R^2 = <0.01 DE = 0.04	p = 0.47 R^2 = 0.02 DE = 0.06	p = 0.37 R^2 = -0.01 DE = 0.02	p = 0.30 R^2 = 0.03 DE = 0.14
PNA	p = 0.55 R^2 = -0.02 DE = 0.01	p = 0.17 R^2 = 0.12 DE = 0.19	p = 0.79 R^2 = -0.01 DE = 0.02	p = 0.42 R^2 = -0.01 DE = 0.02	p = 0.26 R^2 = 0.01 DE = 0.04

* Predictor variables which were incompatible with GAM analysis as they contained fewer unique data levels than the specified k-index.

Table C.4 ***P* values, adjusted R^2 values, and deviance explained (DE) for the single-factor GAMs between annual tree ring $\delta^{18}O$ measured from MKRF-2 and water year PE and climate variables. *P* values <0.05 are shown in bold.**

	WY	AMJ	JAS	OND	JFM
PE variables					
PE day count	p = 0.06 R^2 = 0.09 DE = 0.12	p = 0.31 R^2 = < 0.01 DE = <0.03	p = 0.48 R^2 = -0.01 DE = 0.01	p = 0.05 R^2 = 0.19 DE = 0.25	p = 0.74 R^2 = -0.03 DE = <0.01
Intense PE count	p = 0.73 R^2 = -0.02 DE = 0.00	*	*	p = 0.06 R^2 = 0.07 DE = 0.10	p = 0.23 R^2 = 0.01 DE = 0.04
% PE precipitation	p = 0.96 R^2 = -0.03 DE = <0.01	p = 0.38 R^2 = 0.03 DE = 0.09	p = 0.85 R^2 = -0.02 DE = 0.02	**p = <0.01** R^2 = 0.17 DE = 0.19	p = 0.06 R^2 = 0.17 DE = 0.15
Climate variables					
Mean temperature	p = 0.23 R^2 = 0.01 DE = 0.04	**p = 0.03** R^2 = 0.11 DE = 0.13	p = 0.41 R^2 = 0.05 DE = 0.10	p = 0.88 R^2 = -0.02 DE = 0.01	p = 0.56 R^2 = 0.01 DE = 0.05
Total precipitation	**p = 0.03** R^2 = 0.11 DE = 0.14	p = 0.71 R^2 = -0.03 DE = <0.01	p = 0.76 R^2 = -0.03 DE = <0.01	**p = 0.02** R^2 = 0.12 DE = 0.14	p = 0.05 R^2 = 0.08 DE = 0.11
SPEI	**p = 0.04** R^2 = 0.10 DE = 0.12	p = 0.49 R^2 = -0.01 DE = 0.01	p = 1.00 R^2 = -0.03 DE = <0.01	**p = 0.01** R^2 = 0.14 DE = 0.17	p = 0.15 R^2 = 0.03 DE = 0.06

	WY	AMJ	JAS	OND	JFM
SWE	**p = 0.03** R^2 = 0.11 DE = 0.14				
GS-RH	**p = 0.02** R^2 = 0.12 DE = 0.14				
Climate oscillation indices					
MJO	p = 0.49 R^2 = 0.01 DE = 0.06	p = 0.65 R^2 = -0.02 DE = 0.01	p = 0.24 R^2 = 0.01 DE = 0.04	p = 0.75 R^2 = -0.03 DE =<0.01	p = 0.86 R^2 = -0.02 DE = 0.02
PDO	**p = 0.03** R^2 = 0.11 DE = 0.14	p = 0.71 R^2 = -0.03 DE =<0.01	p = 0.13 R^2 = 0.04 DE = 0.07	p = 0.08 R^2 = 0.06 DE = 0.09	p = 0.68 R^2 = <0.01 DE = 0.04
ENSO	**p = 0.04** R^2 = 0.10 DE = 0.12	**p = 0.04** R^2 = 0.10 DE = 0.12	p = 0.31 R^2 = < 0.01 DE = 0.03	p = 0.01 R^2 = 0.05 DE = 0.08	p = 0.07 R^2 = 0.07 DE = 0.09
AO	p = 0.68 R^2 = -0.02 DE = 0.01	p = 0.17 R^2 = 0.10 DE = 0.16	p = 0.49 R^2 = -0.01 DE = 0.01	**p = 0.02** R^2 = 0.12 DE = 0.15	p = 0.47 R^2 = -0.01 DE = 0.02
NPGO	p = 0.13 R^2 = 0.09 DE = 0.13	**p = 0.04** R^2 = 0.10 DE = 0.12	p = 0.07 R^2 = 0.07 DE = 0.09	p = 0.27 R^2 = 0.05 DE = 0.09	p = 0.17 R^2 = 0.08 DE = 0.13
PNA	p = 0.84 R^2 = -0.03 DE = <0.01	p = 0.20 R^2 = 0.02 DE = 0.05	p = 0.69 R^2 = -0.02 DE =<0.01	p = 0.29 R^2 = <0.01 DE =0.03	p = 0.51 R^2 = -0.02 DE = 0.01

* Predictor variables incompatible with GAM analysis due to their fewer unique data levels than the specified k-index.

Table C.5 **Pearson correlations between Capilano and MKRF-2 $\delta^{18}O$ records and selected tree cellulose $\delta^{18}O$ records from across North America. Chronologies are listed by descending *p* value. DF indicates the degrees of freedom in the Pearson correlation.**

	Capilano correlations			MKRF-2 correlations			
Chronology	***r* value**	***p* value**	**DF**	**Chronology**	***r* value**	***p* value**	**DF**
MKRF-2	0.33	0.03	39	Capilano	0.33	0.03	39
Hudson_AB	-0.37	0.12	17	Csank_BR	0.24	0.38	13
Simard_ID	-0.42	0.16	11	Spry	0.19	0.50	13
Csank_BR	0.33	0.23	13	Hudson_AB	0.13	0.60	17
Porter	-0.17	0.43	21	Simard_OR	0.14	0.64	11
Simard_WA	0.24	0.44	11	Hudson_BB	-0.10	0.67	17
Csank_PB	-0.14	0.53	21	Simard_ID	0.13	0.68	11
Hudson_NU	0.13	0.59	17	Csank_PB	0.08	0.70	21
Simard_OR	-0.14	0.65	11	Porter	-0.08	0.71	21
Spry	0.12	0.67	13	Hudson_NU	0.07	0.77	17
Csank_V	-0.06	0.74	28	Csank_V	0.03	0.87	28
Hudson_BB	0.06	0.82	17	Simard_WA	-0.04	0.90	11